Development of a Design and Sizing Tool for Conceptual Turbofan Engines

MSc Thesis

S.S. Ng

Technische Universiteit Delft

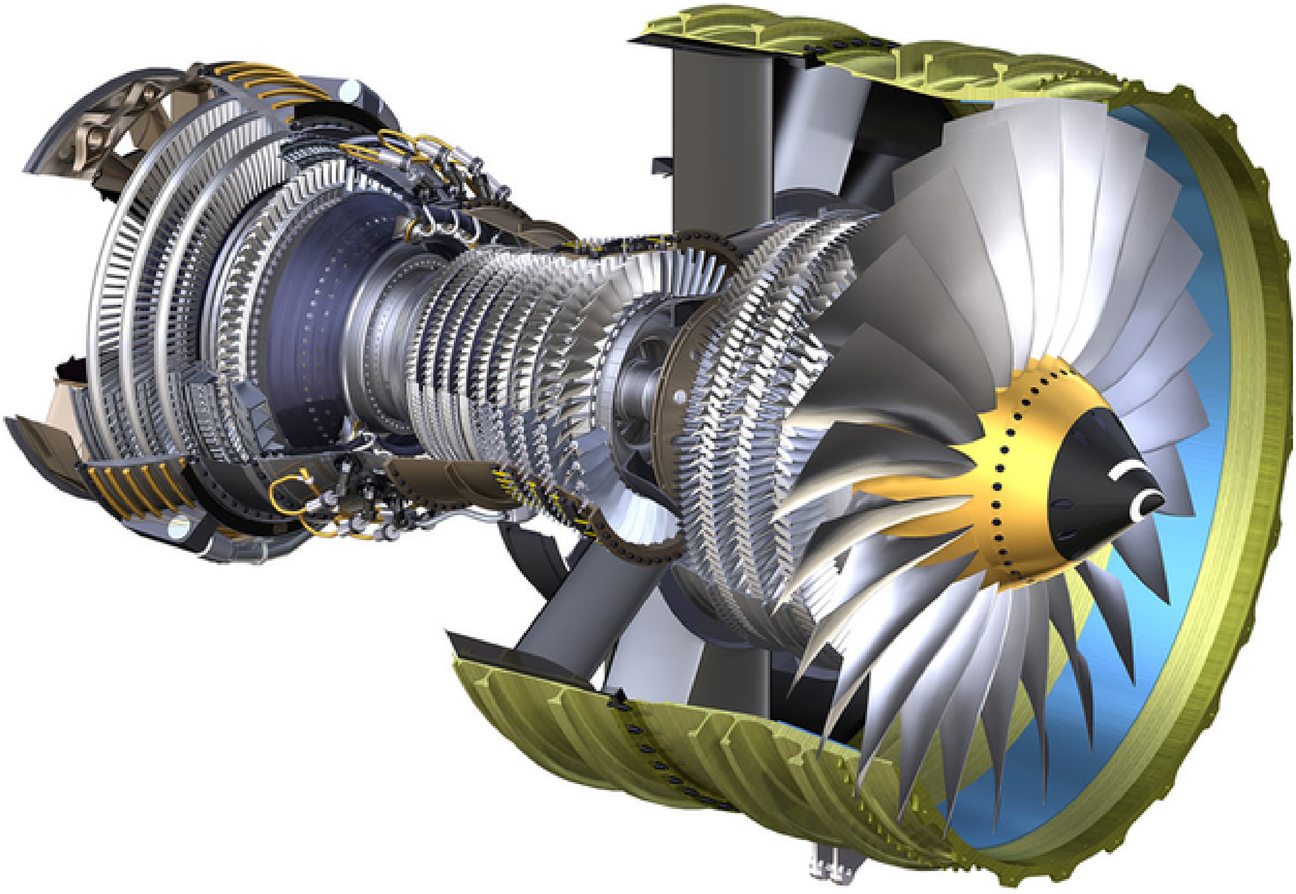

Delft University of Technology

Challenge the future

Development of a Design and Sizing Tool for Conceptual Turbofan Engines

MSc Thesis

by

S.S. Ng

in partial fulfillment of the requirements for the degree of

Master of Science

in Aerospace Engineering

at the Delft University of Technology,

to be defended publicly on Monday January 27, 2020 at 9:00 AM.

Supervisor:	Dr. A. Gangoli Rao	
Thesis committee:	Dr. A. Gangoli Rao	FPP
	Dr. ir. M. Pini,	FPP
	Dr. M. A. Mitici,	ATO

TU Delft Delft University of Technology

Summary

The global air traffic demand is estimated to increase strongly in the next decades. Replacement of the current fleet and new demand will expect a total of 39,210 deliveries by 2038, according to Airbus. The new engines will be subjected to stricter emission regulations due to increased public awareness and political concern over the impact of aviation on sustainability. The Advisory Council for Aeronautical Research in Europe (ACARE) has set very ambitious goals to reduce the environmental footprint of aviation, which will require significant advancements and technology developments. The ACARE goals aim to drive improvements in technology to achieve a 75% reduction in CO_2 emissions per passenger kilometer, a 90% reduction in NO_x emissions, and reduction in perceived acoustic noise from flying aircraft by 65% in 2050. The improvements are compared with the level of performance in 2000.

New aero-engine designs will have more challenging performance targets that reach beyond the capabilities of the current level of technology. Changes in the current designs or new unconventional designs are necessary to tackle the new challenges. Most of the existing tools are not capable of handling the multidisciplinary aspect of aero-engine design, where aerothermodynamic analysis, structural analysis, and weight estimation are all critical. The objective of this thesis project is to develop a multidisciplinary turbofan engine design and sizing tool for conceptual engine design. The tool will be used in a parametric analysis to determine how the main design parameters impact engine characteristics.

The design tool focuses currently on a two-spool unmixed turbofan configuration at the conceptual design phase. Nevertheless, the long term goal is to have capabilities to design any arbitrary engine configuration. A mean-line design method is implemented to perform aerothermodynamic calculations of the engine components, and stage losses are calculated using empirical models. Structural analysis and material selection will be performed to estimate the engine mass. The tool has been validated using publicly available engine data of the CFM56-7B and the PW4056.

A parametric analysis has been conducted using the tool to analyze the effect of several design variables on engine characteristics. A baseline engine comparable to the CFM56-7B has been used at cruise conditions and with a thrust requirement of 24 kN. It has been found that an increased turbine inlet temperature (TIT) will result in lower engine size and weight as a result of the increased specific thrust. The thermal efficiency improves, but the propulsive efficiency drops. The change is firmly dependant on the combination of the compressor temperature and pressure ratio. In this case, with the selected baseline engine, the overall efficiency decreases for increased TIT. The bypass ratio (BPR) defines the ratio between the bypass flow compared to the core flow. An increased BPR has a significant positive impact on fuel efficiency. The bypass nozzle has a much lower exit jet velocity compared to the core flow. A lower jet velocity is more efficient compared to a higher jet velocity because accelerating a larger mass with a small increment is less energy costly for the same momentum. For higher BPR both the propulsive and thermal efficiency show an improvement. On the other hand, the specific thrust of the bypass flow is lower compared to the core flow. Therefore the engine intake mass flow and engine mass will increase. The overall pressure ratio (OPR) defines the work done by the compressors on the working fluid. A higher OPR is favorable for fuel efficiency because more heat energy can be converted into thrust. The extra compressor stages needed for the increased OPR will add to the engine weight.

The trends observed from aero-engine designs are in agreement with the findings of the parametric analysis. The design variables, TIT, BPR, and OPR, have shown increasing trends with every new generation of engine designed. The current level of technology is limiting the further increase in engine performance. Better cooling techniques and improved material properties will allow next-generation engines to reach new performance levels. In the future, it is recommended to include the modeling of cooling flow and emissions to extend the capabilities of the tool.

Acknowledgements

My academic career at the faculty of Aerospace Engineering at the Delft University of Technology has been a challenging journey with ups and downs. I would like to thank the people who supported me during this journey.

I would like to thank my thesis supervisor, Dr. Arvind Gangoli Rao, for giving me the opportunity to work on this thesis project. I am grateful for all the guidance you have given me during times where I felt lost. Your motivation and valuable feedback have supervised me to acquire the desired outcomes and results for this project.

Furthermore, I would like to thank my family and friends for their emotional support during this project. Lastly, I would like to thank my girlfriend Huong for your endless support and love.

Stanley Ng
Delft, December 2019

Contents

List of Figures

List of Tables

Nomenclature

Symbols	Description	Unit
a	Speed of sound	[m/s]
A	Area	$[m^2]$
BLK	Blockage factor	[-]
c	Chord	[m]
C	Absolute velocity	[m/s]
C_D	Drag coefficient	[-]
C_f	Skin friction coefficient	[-]
C_L	Lift coefficient	[-]
C_v	Nozzle velocity coefficient	[-]
C_p	Constant pressure coefficient	[-]
C_v	Constant volume coefficient	[-]
D	Drag	[F]
D	Diameter	[m]
F	Force	[N]
FSP	Blade row spacing over chord length	[-]
f	Frequency	[hz]
F_t	Tangential loading parameter	[-]
g	Gravitational constant	$[m/s^2]$
h	Altitude	[m]
h	Enthalpy	[J/K]
H	Height	[h]
i	Incidence angle	$[^o]$
I	Rothalpy [J/K]	
K	Factor for intake lip losses	[-]
L	Lift	[F]
L	Length	[m]
LD	Length over diameter	[-]
M	Mach number	[-]
m_b	Mass of a blade	[N]
N	Magnification factor	[-]
n_b	Number of blades	[-]
n_{stages}	Number of stages	[-]
o	Pitch to chord ratio	[-]
P	Pressure	[Pa]
Q	Energy	[J]
p_st	Barlow's formula	[Pa]
q	Dynamic pressure	[Pa]
` r	Radius	[m]
Re	Reynolds number	[-]
S	Volume	$[M^3]$
s	entropy	[J/K]
s	critical area ratio a scaling factor	[-]
U	Rotational velocity	[m/s]
t	Thickness	[m]
T	Temperature	[K]

Symbols	Description	Unit
V	Velocity	[m/s]
W	Weight	[N]
W	Work	[J]
$\dot{W}$	Work	[W]
Y	Total loss coefficient	[-]
Y_p	Profile loss coefficient	[-]
Y_s	Secondary loss coefficient	[-]
Y_{TE}	Trailing edge loss coefficient	[-]
Y_{TC}	Tip clearance loss coefficient	[-]
Z_{TE}	Spanwise depth penetration	[m]

Greek Symbols	Description	Unit
α	Angle between V and meridional plane	[^{o}]
β	Blade angle relative to meridional plane	[^{o}]
δ	Deviation angle	[^{o}]
δ^*	Boundary layer displacement thickness	[m]
Δ	Difference	[-]
ρ	Density	[kg/m^3]
$\dot{m}$	Mass flow rate	[kg/s]
ϕ	Flow coefficient	[-]
ψ	Loading coefficient	[-]
λ	Form factor	[-]
λ	Contraction ratio	[-]
Λ	Degree of reaction	[-]
η	Efficiency	[-]
γ	Ratio of specific heats	[-]
γ	Stagger angle	[^{o}]
π	Pressure ratio	[-]
ψ_T	Zweifel criterion	[-]
σ	Stress	[Pa]
σ	Solidity	[-]
θ	Camber angle	[^{o}]
τ	Torque	[Nm]

Suffix	
abs	Absolute
airfoil	Airfoil
ax	Axial
cg	Centre of gravity
casing	Casing
crit	Critical
csf	Constant section
csl	Constant section length
cst	Constant section throat
dd	Drag divergence
des	Design
dr	Drag rise
eff	Effective
f	Fuel
f	Face
final	Final
firtree	Firtree
i	index
initial	Initial
inlet	Inlet
irreversible	irreversible
m	Mean
n	Nozzle
neck	Neck
o	Overall
p	Propulsive
poly	Polytropic
post	Post
platform	Platform
rel	relative
rl	Round lips
rim	Rim
sl	Sharp lip
shroud	Shroud
stage	Stage
shaft	Shaft
t	Throat
th	Thermal
to	Take off
w	Angular direction
W_r	Weight ratio
∞	Ambient condition
$0, t$	Total
$1, i$	In
$2, ii$	Out

Abbreviations	
ACARE	Advisory Council for Aviation Research and Innovation in Europe
AM	Ainley & Mathieson
BPR	Bypass ratio
BM	Burst margin
BS	Burst speed
CFD	Computational fluid dynamics
DC	Dunham & Came
DM	Design margin
FHV	Fuel heating value
FPP	Flight power and propulsion
HPC	High-pressure compressor
HPT	High-pressure turbine
IGV	Inlet guide vane
KO	Kacker & Okapuu
LPC	Low-pressure compressor
LPT	Low-pressure turbine
NASA	National Aeronautics and Space Administration
NPR	Nozzle pressure ratio
OEM	Original equipment manufacturer
OPR	Overall pressure ratio
PR	Pressure ratio
TSFC	Thrust specific fuel consumption
TIT	Turbine inlet temperature
2D	Two-dimensional
3D	Three dimensional

1 Introduction

Aero-engine design is a challenging task with many requirements and demands to be satisfied. Public awareness and political concern about the impact of aviation on the environment have been increasing [16]. As a result, international organizations implement strict policies to reduce emissions, reduce the noise emitted, and improve the fuel efficiency of aero-engines. The Advisory Council for Aeronautical Research in Europe (ACARE) [17] has set very ambitious goals to reduce the environmental footprint of aviation, which will require significant advancements and technological developments. The ACARE goals aim to drive improvements in technology to achieve a 75% reduction in CO_2 emissions per passenger kilometer, a 90% reduction in NO_x emissions, and perceived acoustic noise from flying aircraft to be reduced by 65% by 2050. Other international organizations are also pushing stricter emission legislation to reduce the environmental footprint.

The operators of the aircraft engines, e.g., airliners, are pressured by the increasing oil prices that are driving operational costs up. Operating engines with improved fuel consumption lowers the direct fuel costs and hence the operational costs. The effort to reduce fuel burn is also beneficial to emission reduction as the CO_2 emissions are directly proportional to fuel consumption.

The industry standard for fuel efficiency of aero engines is the thrust specific fuel consumption (TSFC), which is a measure of fuel consumption per unit of thrust produced. Higher fuel efficiency can be achieved by increasing engine efficiency or reducing engine weight. Increasing the bypass ratio (BPR) improves the propulsive efficiency, which leads to improvements in the TSFC. However, the larger fan size due to higher BPR adds significant engine weight and can negatively impact the TSFC. Another crucial design variable is the overall pressure ratio (OPR). Operating at higher OPR can increase thermal efficiency, but the compressor weight might increase as a result. [14] The turbine inlet temperature (TIT) can be increased to increase the specific thrust. The impact of these design parameters is not linear on the TSFC. It is unclear to what extent the BPR, OPR, and TIT can be increased while the extra weight is not negating the beneficial effects. Accurate design tools could be used to predict the engine characteristics and estimate the engine weight for given design variables to see how these impact the engine.

While many existing methods are capable of estimating engine performance, their accuracy and complexity vary significantly. Some models are solely based on statistical data and lack the necessary accuracy for conceptual design. On the other hand, more accurate models require a large number of detailed input variables. It loses the purpose of calculating the performance quickly. Engine design is a multidisciplinary process, including thermodynamics, aerodynamics, and structural analysis. Existing tools with these disciplines within an acceptable level of detail and accuracy are very limited. In Chapter 2, the state of the art tools for both aerothermodynamic analysis and weight estimation are shown. Every tool will be elaborated shortly upon, highlighting its strong points and shortcomings. Only a handful of tools are capable of aerothermodynamic analysis and weight estimation. In most cases, weight estimation capabilities are very preliminary.

1.1. Thesis objective

Combining the challenges from the aviation industry, regulations, and the limitations of currently available tools, the following objective for this thesis project has been formulated:

> *Develop a multidisciplinary turbofan engine design and sizing tool for conceptual engine design. The tool will be used in a parametric analysis to determine how the main design parameters impact engine performance and sizing.*

The conclusions and findings from this thesis project can be used for future aero-engine design to see how to propulsive and thermal efficiency.

Tiemstra[1] and Boormsa[4] have already modeled several engine components. In this project, the remaining components are developed, and all the separate modules are integrated into a single tool. Based on the previously mentioned, the following individual project objectives are formulated:

- Develop the design modules for the remaining component of the turbofan engine. The components developed from scratch are; low-pressure turbine, intake, nozzle, and nacelle. For each component, the module estimated the performance and weight at conceptual design level.
- Redesign the several component modules to be consistent with the other modules. The same design approach and structure is used for all modules. The redesign applies to the high-pressure compressor, low-pressure compressor, and high-pressure turbine designed by Boorsma and Tiemstra.
- Build a framework for the turbofan engine code where the codes for the separate components can be integrated to model the complete turbofan engine.
- Conduct several analyses to find the impact of key design parameters on engine performance and weight estimation. The key design parameters to be analyzed include BPR, FPR, OPR, and TIT.

The main contribution of this thesis project will be to deliver a conceptual turbofan engine design & sizing tool for (future) research purposes. Future users will be able to use it to quickly estimate engine performance and weight based on a small list of design variables. The framework will also allow for future modifications, and new modules can be added to model other engine configurations.

1.2. Thesis outline

This thesis report starts-off with the literature review and background on turbofan engines in Chapter 2. The methodology conducted to create a conceptual turbofan engine design and sizing tool is presented and discussed in Chapter 3. Thereafter, the tool will be validated using existing engine designs. The validation results are discussed in Chapter 4. The tool is then used to conduct a parametric analysis and to assess the impact of different parameters on engine characteristics, which is documented in Chapter 5. Finally, the main findings and conclusions are reported in Chapter 6. In this chapter also the recommendations for possible future work are given.

2
Background

2.1. State of the art engine tools

Simulating aircraft engine performance using multidisciplinary simulation tools helps to assess and compare new technologies and design concepts for civil aviation. Many successful attempts have already been made to develop multidisciplinary engine simulation tools. In section 2.2 the existing gas turbine performance codes are elaborated upon while in section 2.3 weight estimation codes are reviewed.

2.2. Gas turbine performance codes

Gas turbine simulation programs have shown strong development, the programs have advanced from simple engine specific performance codes to complex object-oriented generalized performance tools capable of simulating arbitrary engine configurations. Kyprianidis [14] has provided a review of existing gas turbine performance codes, his findings are summarized in this section.

GENENG I/GENENG II are considered the first generalized codes for engine design, and it was developed at NASA by Koening & Fishbach [18][19]. GENENG I/GENENG II are capable of simulating the design point and off-design performance of turbofan engines and turbojet engines with multiple spool configurations. TURBOMATCH, developed by MacMillan [20], was another static generalized simulation program developed during the early days of gas performance codes. Palmer and Cheng-Zong [21] later developed TURBOTRANS, which is based on the original code TURBOMATCH. The code can simulate the dynamic behavior of engine configuration with different control systems. NLR and TU Delft developed a generalized simulation program called GSP [22][23]. The code can analyze both steady-state and transient performance of any gas turbine configuration. The tool is also capable of analyzing the engine in-flight exhaust emissions. Grönstedt developed GeSTPAn [24][25] which is a generalized simulation program able to estimate the steady-state and transient performance of arbitrary engine configurations. Drummond et al. [26] reported in their study the need to develop object-oriented simulation programs instead of improving the older models. Their main reasoning was based on the relation of engine design with the development of each engine component. New engine designs require more linking of computational tools, and the integration process becomes more complicated. By switching to object-oriented languages based on a compatible framework, it could ease the effort required for the integration. As a result of the findings of Drummond et al., NASA has developed NCP [26] and NPSS [27][28]. NCP is the new platform developed to be used for future codes. NPSS is based on the framework of NCP and is capable of modeling different levels of fidelity varying from simple thermodynamic cycle calculations to full engine geometry CFD simulations. Lolis [5] believes these two programs form the current state of the art in gas turbine performance simulation. Proosis [29][30] is an object-oriented simulation tool for gas turbine performance developed by a consortium of European universities, research institutes, and corporate companies. It allows the user via a graphical interface to modularly build any arbitrary engine configuration.[14] One of the more recently published methods is the "component based" tool called ATLAS developed by the Cranfield university[5]. This tool estimates the engine weight by modeling the separate engine components individually. ATLAS claims to have an accuracy of a maximum 10% error. All the discussed codes have been summarized in table 2.1.

Table 2.1: Overview of gas turbine performance codes. Source:[14]

Ref. no.	Code Name	Publisher	Year of Publication	Author(s)
[18][19]	GENENG I/ GENENG II	NASA	1972	Koening & Fishbach
[20]	TURBOMATCH	Cranfield University	1974	MacMillan
[21]	TURBOTRANS	Cranfield University	1982	Palmer & Cheng-Zong
[22][23]	GSP	NLR & TU Delft	2000	Visser & Broomhead
[24][25]	GeSTPAn	Chalmers University	2000, 2002	Grönstedt, Gröonstedt & Pilidis
[26]	NCP	NASA	1992	Drummond et al.
[27][28]	NPSS	NASA	1991, 2000	Claus et al., Lylte
[29][30]	PROOSIS	Consortium of EU universities, research institutes and corporate companies	2007	Bala et al., Alexiou et al.

2.3. Gas turbine weight estimation

Estimation of engine weight is no easy task due to the large complexity and interdependence of the components. This led to the development of preliminary weight estimation methods based on different approaches. Lolis [5] has given a good overview of existing preliminary weight estimation methods and the categorization of the approaches. The available approaches can be separated into two categories; the first category predicts the weight of the whole engine while the second category estimates the weight by calculating the engine components separately. The philosophy behind the different approaches was based on three parameters: the required level of fidelity, complexity, and availability of component weight data.

The first category is also named "whole engine based" because the weight of only the entire gas turbine can be estimated, not of the individual engine components. The engine weight is also only based on only a few parameters, thus the accuracy, complexity, and calculation time is much lower. The downside of these approaches is that they have been derived from existing engine data. When the correlations are used for engines dissimilar engine data, it can lead to large inaccuracies. Table 2.2 provides an overview of the whole engine based methods by Lolis [5]. The table also gives the input variables required for the correlations.

Table 2.2: Overview of whole engine based weight estimation methods. Source:[5]

Ref. no.	Author(s)	Publication Year	Weight Correlation
[31]	Whitehead and Brown	1953	$WT = f(\dot{m}_{des})$
[32]	Pennington	1959	$WT = f(FN)$
[33]	Torenbeek	1975	$WT = f(FN_{to}, \dot{m}_{to}), BPR, OPR$
[34]	Raymer	1989	$WT = f(FN_{to}, BPR)$
[35]	Jenkinson et al.	1999	$WT = f(FN, BPR)$
[36]	Svoboda	2000	$WT = f(FN_{to})$
[37]	Guha et al.	2012	$WT = f(D_{fan})$

$\dot{m}$ = mass flow rate, FN = thrust, BPR = bypass ratio, D_{fan} = fan diameter, to = take-off, des = design

The second category of the engine weight estimation described by Lolis is the component-based approach. The weight of the separate components is calculated, and the total sum forms the total engine weight. The higher complexity of these methods requires more input variables but will result in a higher level of accuracy at the cost of longer calculation time. This approach is taken in this research project because of the higher level of accuracy. Lolis [5] has presented a clear overview of the existing component-based approaches.

Sagerser et al. [38] were the first ones to develop a method able to estimate each component's weight and dimensions separately. The method was initially developed for vertical take-off and landing /short take-off and landing aircraft. However, it could also be used for conventional engines as well. The method is based on correlating geometrical properties with available engine data[5].

A collaboration by NASA with Boeing led to the development of WATE by Pera et al. [39]. WATE uses preliminary design and sizing to estimate the structural geometry and weight of gas turbine components. Only limited engine data was used to calibrate the model. The accuracy of the first WATE method is not very high. WATE did nonetheless, form the basis of a series of weight estimation methods. The first one is the simplified WATE method by Klees and Fishbach [40]. Later Onat and Klees [41] improved and corrected the WATE approach and developed WATE-2. The method has improved accuracy at the cost of more input variables and increased complexity. Hale [42] developed WATE-S based on the original WATE method and is suited for small gas turbine designs. Tong and Naylor [43] used the WATE-2 code to convert this into an object-oriented code named WATE++. Lolis [5] mentions that despite the complexity the WATE series is still the most accurate method and frequently used method available. Some have used the WATE method as the basis for their modified methods, Sanghi et al. used the WATE by Pera et al.. They adjusted the method to make it suitable for the estimation of military turbojet engine weight. Chalmers University in collaboration with Stuttgart University developed the code WeiCo based on the Onat and Klees WATE-2 method [5].

Other weight estimation method besides the NASA WATE method is GasTurb by Kurzke [44]. GasTurb is a commercial gas turbine performance and design software capable of estimating turbofan weight. It can also handle unconventional gas turbine architectures like geared-turbofan and intercool-recuperated engines. However, it only allows specific engine configurations, restricting the study of arbitrary engine architectures. The tool is also capable of performing preliminary geometrical design, including the disk stress analysis[14].

An overview of the existing component-based approaches is given in table 2.3.

Table 2.3: Overview of component based weight estimation methods. Source:[5]

Ref. no.	Code Name	Publisher	Publication Year	Author(s)
[38]	VTOL/STOL	NASA	1971	Sagerser et al.
[39]	WATE	NASA (collab with Boeing)	1977	Pera et al.
[40]	WATE (simplified)	NASA	1978	Klees & Fishbach
[41]	WATE-2	NASA	1979	Onat & Klees
[42]	WATE-S	NASA	1982	Hale
[43]	WATE++	NASA	1982	Tong & Naylor
[45]	Military turbojet	Indian Institute of Technology	1998	Sanghi et al.
[46]	WeiCo	Chalmers University & Stuttgart University	2007	Bretschneider et al.
[44]	GasTurb	GasTurb & RWTH Aachen university	1993	Kurzke
[5]	ATLAS	Cranfield university	2014	Lolis

2.4. The turbofan engine

The turbofan engine is currently the most used engine configuration for commercial aviation. Turbofan engines were developed to combine the best aspects of the turbojet and the turboprop. The lower mean jet velocity improves the propulsive efficiency compared to the jet engine. In a turbofan configuration, a large fan accelerates air rearwards. Only a small part of the flow enters the core engine, and the rest bypasses the core via the bypass duct. The air bypassing the core is the cold stream, and the core stream is called the hot stream. The bypass ratio defines the ratio of flow of the bypassing cold stream to the hot stream.

The turbofan components of interest are shown. Whether the component is already designed in the previous project or is designed this project is also added. As mentioned earlier in the introduction, some components need to be modified or completely redesigned to fit into the same framework.

- Fan (Tiemstra, used as delivered)
- Low-pressure compressor (Tiemstra, modified this project)
- High-pressure compressor (Boormsa, completely redesigned)
- Combustion chamber (Boorsma, used as delivered)
- High-pressure turbine (Boorsma, completely redesigned)
- Low-pressure turbine (Designed this project)
- Nozzle (Designed this project)
- Nacelle (Designed this project)

The fan produces thrust by accelerating air, part of the air is guided into the core engine where the compressor increases the pressure of the air. In the combustor, the mixture of air and fuel is combusted to increase the energy of the gas mixture. The turbine extracts power from the working fluid passing through the core to drive the fan and the compressors. The low-pressure turbine has unlike the high-pressure turbine no blade cooling because the gas temperature is significantly lower. The nozzle guides the working fluid from the last turbine stage and accelerates the exhaust gas before disposal. The nozzle is designed to produce thrust, minimize total pressure loss and suppress jet noise. The nacelle houses the turbofan engine and is designed to minimize aerodynamic drag of the engine. The inlet must guide and allow for sufficient mass flow to enter the engine during operation.

2.4.1. Nomenclature for turbofan design

In this report, the most common terms and abbreviations of gas turbine performance engineering will be employed. The preferred system of units will be the SI system with few exceptions from figures if the original source differs in unit system. A complete list of symbols and abbreviations can be found in the Nomenclature.

The thermodynamic stations will be numbered according to the description in the SAE Aerospace Standard AS755. The thermodynamic station numbering is shown in figure 2.1 and table 2.4. The station locations will be used as indices of parameter names to indicate the values of different station locations.

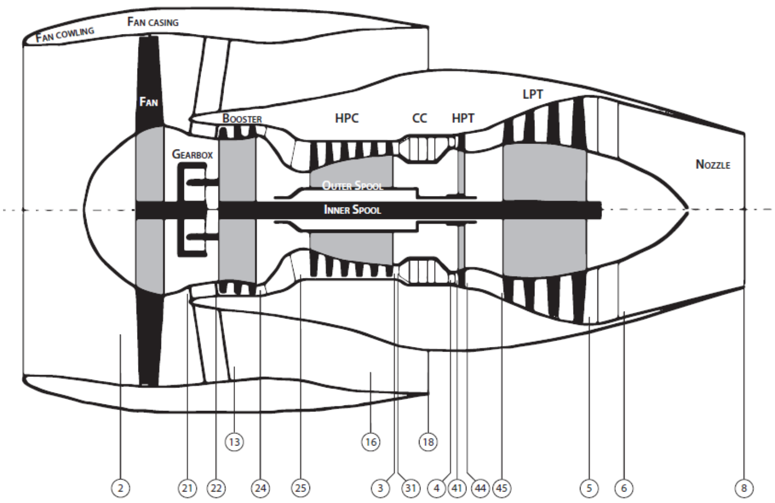

Figure 2.1: Turbofan nomenclature with station numbers. Source:[1] [2]

Table 2.4: Definition of station numbers

Station	Location
0	Free stream condition
1	Inlet entry
13	Fan exit
16	Bypass nozzle entry
18	Bypass nozzle exit
2	Fan entry
21	Core flow entry
22	LPC entry
24	LPC exit
25	HPC entry
3	HPC exit
31	Combustor entry
4	Combustor exit
41	HPT entry
44	HPT exit
45	LPT entry
5	LPT exit
6	Core nozzle entry
8	Core nozzle exit

2.4.2. Brayton cycle

The jet engine working principle is based on Newton's third law. The fluid is accelerated and discharged to generate thrust. The gas turbine usually has traditionally three distinctive components, an upstream compressor coupled to a downstream turbine, and a burner. The thermodynamic process behind the gas turbine is the Brayton cycle, as shown in figure 2.2. The Brayton cycle can be described in the h-s diagram by ambient air being compressed (*2-3*), burned at constant pressure (*3-4*), and expanded in the turbine (*4-5*). These thermodynamic processes can either be real with losses or ideal without losses. The ideal case or isentropic process is indicated in figure 2.2 by subscript $_{is}$, while the numbers without a subscript indicate the real case. In the figure, the constant pressure lines are indicated by the dotted lines. Due to the divergent behavior of the constant pressure lines, a higher pressure ratio will lead to the higher enthalpy of the gas mixture if burned at constant pressure.

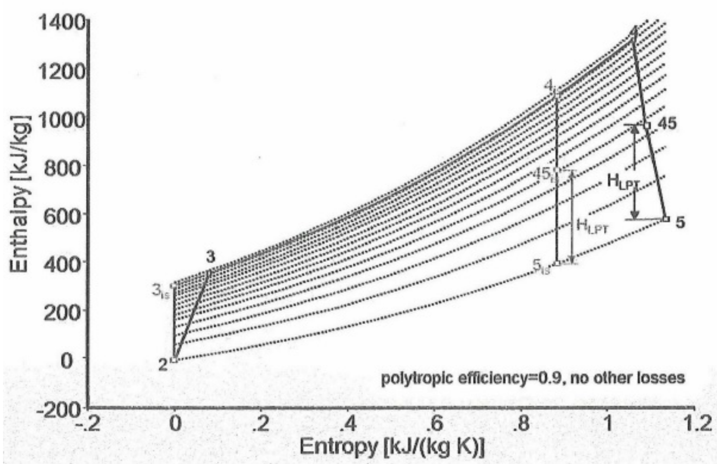

Figure 2.2: H-s diagram of an ideal and real Brayton cycle. Source:[3]

In an ideal cycle, the cycle is composed of compression and expansion processes that operate with no increase in entropy. The following definition for the thermal efficiency of the ideal Brayton cycle can be found in literature [47]:

$$\eta_{\text{thermal}} = 1 - \left(\frac{P_2}{P_3}\right)^{\frac{\gamma-1}{\gamma}} \tag{2.1}$$

Based on equation 2.1 it can be noticed the heat capacity ratio γ influences the thermal efficiency. Another important observation is that the ideal Brayton efficiency continuously increases with pressure ratio. The trend in the past has shown a continuous increase in pressure ratio for gas turbines, which is beneficial for higher thermal efficiency [48] .

3

Methodology

In this chapter, the fundamentals and methods used for the development of the tool are discussed. Firstly, the most important fundamentals of turbomachinery are discussed. Secondly, the methods to design the engine components are elaborated upon. Lastly, the structural analysis and weight estimation of the engine components will be discussed.

3.1. Fundamentals

The basic fundamentals of aero-engine design will be discussed before the more in-depth methodology component design for the compressor and turbine will be treated.

3.1.1. Flowpath

The mean-line analysis method is a one-dimensional analysis widely used for conceptual engine design. It provides a simplified representation of the actual fluid flow field that still provides the user with an indication of the performance. Ainley and Mathieson [9] [49] have done extensive research on the turbine losses using the mean-line design method. It has been proven that their mean-line method is able to predict the overall efficiency of a stage with acceptable accuracy for conceptual design.

The flow path can have different types of mean-line designs, three different mean line configurations are shown in figure 3.1.

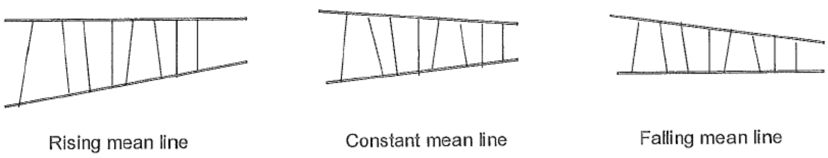

Figure 3.1: Mean-line configurations. Source:[4]

The compressor and turbine will have multiple stages, and each stage will consist of a stator blade row (S) and a rotor blade row (R). The flowpath for a compressor and turbine has been shown in figure 3.2 and 3.3 respectively. The compressor stage will start with the rotor followed by a stator, and the turbine stage starts with a stator followed by a rotor.

Each stage will have its own numbering for the stage station. From the stage inlet till the outlet four different stations will be used as can be seen in figure 3.2 and 3.3. For simplicity stations 2 and 3 in figure 3.2 and 3.3 will be combined into a single station 2 while the stage outlet will then become station 3.

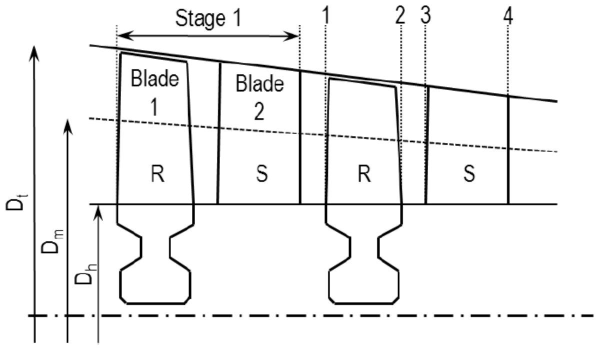

Figure 3.2: Compressor flowpath designation. Source:[5]

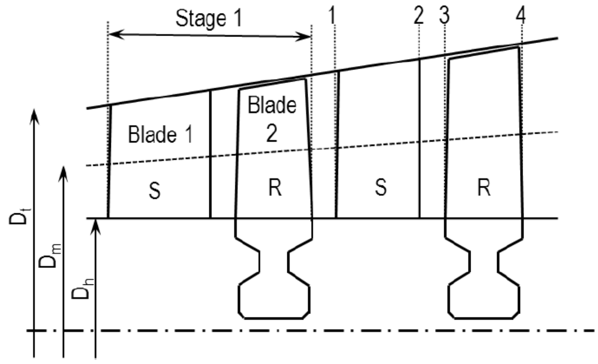

Figure 3.3: Turbine flowpath designation. Source:[5]

3.1.2. Velocity triangles

The velocity triangles for the compressor(figure 3.4) and turbine(figure 3.5) will be used to present the velocity vector for the for every stage. In the figures, C_i indicates the total velocity, V_i, the relative velocity, and U the rotational velocity. The differences between the velocity triangle for the compressor and the turbine will be the position of the rotating blade. As mentioned earlier, the compressor starts with a rotor followed by a stator while the turbine starts with a stator followed by a rotor.

The gas enters the compressor stage with velocity C_1 at an angle α_1 with static pressure and temperature p_1, T_1. For the turbine stage (figure 3.5 the flow will be expanded by the stator blades to p_2, T_2 and leaves the nozzle blades with increased velocity C_2 at a deflected angle α_2. The rotor blades further expand and deflect the gas. The gas leaves with conditions p_3 and T_3 and relative velocity V_3 at an angle β_3. The swirl angle is given as angle α_3. The rotational velocity does vary from root to tip of the blade as the blade radius from the engine center changes. The summation two velocity components $(C_{w2} + C_{w4})$ represents the change in the whirl component of momentum per unit mass flow, which can be extracted to produce the useful torque [8].

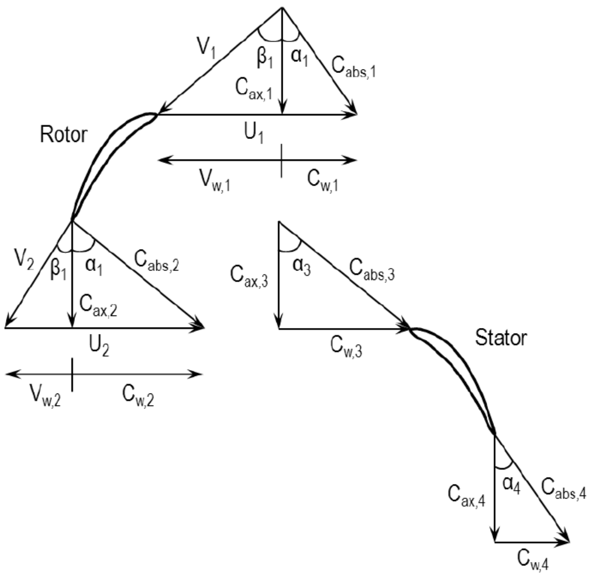

Figure 3.4: Compressor velocity triangles. Source:[5]

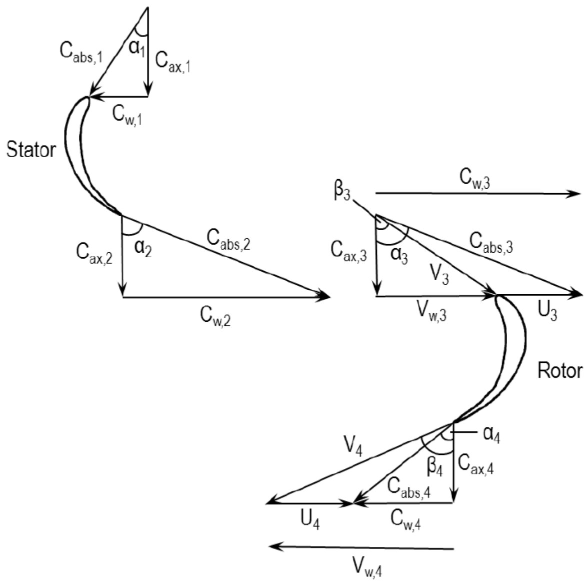

Figure 3.5: Turbine velocity triangles. Source:[5]

3.1.3. Cascade geometry

The cascade geometry is shown in figure 3.6, it is defined by the following geometrical parameters:

- β_1: Relative blade inlet angle
- $\beta_1^{'}$: Blade inlet angle
- β_2: Relative blade outlet angle
- $\beta_2^{'}$: Blade outlet angle
- i: Incidence angle
- γ: Stagger angle
- θ: Camber angle
- σ: Solidity C/S
- t: Thickness
- S: Stagger spacing
- C: Chord length
- t: Maximum thickness

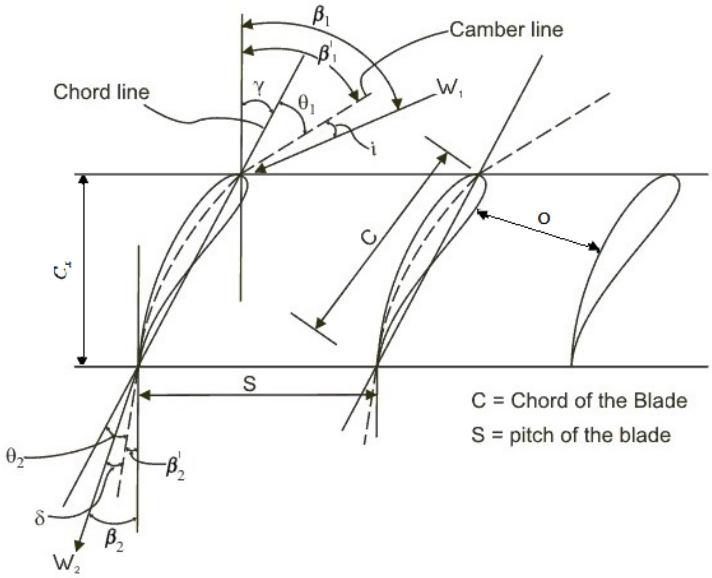

Figure 3.6: A turbine cascade. (Modified image from original source) Source:[6]

3.1.4. Flow governing equations

In aero-engine design several different disciplines come together namely; fluid mechanics, aerodynamics and thermodynamics.[7] The following theories can be considered the fundamentals of turbomachinery working principles.

1. Continuity Equation
2. The First Law of Thermodynamics
3. Momentum Equation - Newton's Second Law of Motion
4. The Second Law of Thermodynamics, Entropy

3.1.5. Continuity equation

The continuity equation describes the law of conservation of mass of a gas, which states that the mass of a given control volume moving in the fluid remains constant. The continuity equation is given as:

$$\rho_1 A_1 C_1 = \rho_2 A_2 C_2 \tag{3.1}$$

3.1.6. The first law of thermodynamics

The first law of thermodynamics describes the law of conservation of energy. In a closed system, energy cannot be created or destroyed. It can only be converted into another form. The first law of thermodynamics is described by equation 3.2.

$$\oint (dQ - dW) = 0 \tag{3.2}$$

By applying the first law of thermodynamics to a steady fluid through a control volume, the steady flow energy equation can be derived. Assuming the potential energy remains constant, the steady flow equation can be rewritten into equation 3.3, where h_0 is the total enthalpy.

$$\dot{Q} - \dot{W}_x = \dot{m}\left[(h_2 + \frac{1}{2}c_2^2) - (h_1 + \frac{1}{2}c_1^2)\right] = \dot{m}\,(h_{02} - h_{01}) \tag{3.3}$$

3.1.7. Momentum equation

The conservation of momentum equation states that the rate of change in linear momentum of a volume moving with a fluid is equal to the forces acting on the fluid and its surface [7]. The momentum equation for a system with a mass *m* along the x-direction is given by equation 3.4.

$$\sum F_x = \frac{d}{dt}(mc_x) \tag{3.4}$$

By applying the conservation of momentum principle to a turbo-machine, the change in angular momentum obtained by the change in the tangential velocity is equal to the summation of all the forces applied on the rotor. Assuming a constant mass flow rate, the torque exerted by the changes in angular velocity can be described by equation 3.5.

$$\tau = \dot{m}(r_2 C_{w2} - r_1 C_{w1}) \tag{3.5}$$

For a rotor rotation at the angular velocity Ω, the rate at which the rotor does work or extract work from the fluid is determined by equation 3.6.

$$\dot{W}_c = \tau_A \Omega = \dot{m}(U_2 C_{w2} - U_1 C_{w1}) \tag{3.6}$$

The work done on the fluid is then calculated by equation 3.7, which is commonly called the Euler work equation.

$$\Delta W_c = \frac{\dot{W}_c}{\dot{m}} = U_2 C_{w2} - U_1 C_{w1} \tag{3.7}$$

In the turbine stages, the rotor extracts work from the fluid. Therefore, the sign for the work is reversed. The specific work for the turbine is determined by equation 3.8, which is the Euler turbine equation.

$$\Delta W_t \frac{\dot{W}_t}{\dot{m}} = U_1 C_{w1} - U_2 C_{w2} \tag{3.8}$$

The Euler turbine equation can be divided into relative quantities by first expressing it in terms of static enthalpy. Equation 3.9 gives the derived rothalpy equation from the Euler equation.

$$I = h + \frac{1}{2}c^2 - Uc_\theta = h + \frac{1}{2}w^2 - \frac{1}{2}U^2 \tag{3.9}$$

In equation 3.9 the first two terms can be defined as the relative enthalpy as $h_{0,rel} = h + \frac{1}{2}w^2$. Equation 3.9 can then be simplified into equation 3.10.

$$I = h_{0,rel} - \frac{1}{2}U^2 \tag{3.10}$$

For rotor rows, the relative stagnation enthalpy is constant, given that the blade speed is constant.

3.1.8. The second law of thermodynamics, entropy

The second law of thermodynamics states that the total enthalpy remains constant for an isolated system. In the isolated system, no energy can enter the system or leave the system. Based on the second law of thermodynamics, the Inequality of Clausius can be defined as shown in equation 3.11.

$$\oint_V \frac{dQ}{T} \leq 0 \tag{3.11}$$

With steady flow through a system's control volume in which the fluid experiences a change of state from entry at condition 1 and the exit at condition 2. The Inequality of Clausius can be written into equation 3.12, here the property entropy is introduced.

$$\int_2^1 \frac{d\dot{Q}}{T} \leq \dot{m}(s_2 - s_1) \tag{3.12}$$

From equation 3.12 it is possible to define an adiabatic and reversible process by rewriting it into equation 3.13, where $\Delta S_{\text{irreversible}}$ is the irreversible entropy production.

$$\dot{m}(s_2 - s_1) = \int_2^1 \frac{d\dot{Q}}{T} + \Delta S_{\text{irreversible}} \tag{3.13}$$

For a flow undergoing a process that is both adiabatic and reversible, the entropy will remain constant. This type of process will be called isentropic. In turbomachinery, the processes are usually adiabatic or close to being adiabatic, but not reversible. An isentropic compression or expansions represent the best possible process that can be achieved. Therefore, to maximize efficiency the irreversible entropy production $\Delta S_{\text{irreversible}}$ must be minimized[7].

3.1.9. Thermodynamic properties of fluids

Fluids have properties like pressure P, temperature T, and density ρ, but other thermodynamic properties such as the internal energy u, the enthalpy h, the entropy s, and the specific heats C_p and C_v also change during a flow process.

3.1.10. Ideal gas

Air consist of a mixture of different gases. In the temperature range 160-2100 K, it can be considered as a pure substance. According to Dixon and Hall [7], the ideal gas relationship holds within these temperature conditions. The ideal gas law is given by equation 3.14.

$$p = \rho R T \tag{3.14}$$

Where R is the gas constant and is defined by:

$$R = C_p - C_v \tag{3.15}$$

Gases at high temperatures and low-pressures conform to the ideal gas law. An ideal gas can either be a semi-perfect gas or a perfect gas. For semi-perfect gas, the specific heat capacities are functions of temperature only:

$$C_p = \left(\frac{\delta h}{\delta T}\right)_p = \frac{dh}{dT} = C_p(T) \tag{3.16}$$

$$C_v = \left(\frac{\delta u}{\delta T}\right)_p = \frac{du}{dT} = C_v(T) \tag{3.17}$$

Over large temperature differences, common gasses, including air should be treated as semi-perfect gas. In figure 3.7 the variation of C_p and γ ($\gamma = C_p/C_v$) is shown. The large variation of these two parameters shows why for large temperatures differences gasses cannot be treated as perfect gases. The C_p of fluid species can be approximated using the Shomate equation, which is a polynomial equation adopted for regression. The Shomate equation is given by equation 3.18. The coefficients in the equation vary per species and temperature and can be found in the NIST –JANAF Thermo-chemical Tables [50].

$$C_{pi} = A_i + B_iT + C_iT^2 + D_iT^3 + E_i/T_2 \tag{3.18}$$

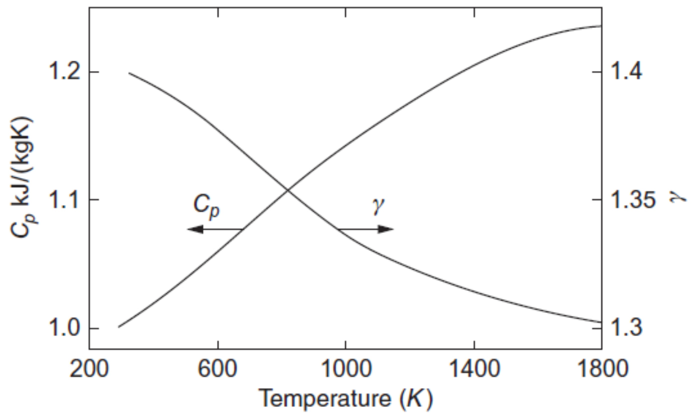

Figure 3.7: Variation of gas properties with temperature for dry air. Source:[7]

3.1.11. Compressible flow relation for perfect gases

The Mach number of a flow is defined as the flow velocity over the local speed of sound. The mathematical form is shown in equation 3.19.

$$M = \frac{c}{a} = \frac{c}{\sqrt{\gamma RT}} \tag{3.19}$$

For flow speeds higher than Mach 0.3, the flow can no longer be considered incompressible. Aero-engine machines require high flow rates and high blade speeds, and this will inevitably lead to compressible flow [7]. Based on the stagnation enthalpy, it is possible to derive the relation for the stagnation temperature over the static temperature. The stagnation enthalpy relation is shown in equation 3.20.

$$h_0 = C_pT_0 = C_pT + \frac{c^2}{2} = C_pT + \frac{M^2\gamma RT}{2} \tag{3.20}$$

Given equation 3.21 it is possible to simplify equation 3.20 into equation 3.22.

$$\gamma R = (\gamma - 1)C_p \tag{3.21}$$

$$\frac{T_0}{T} = 1 + \frac{\gamma - 1}{2} M^2 \tag{3.22}$$

The stagnation condition of the flow is the static condition that is measured if the flow is brought isentropically to rest. The conditions for an isentropic process combined with perfect gas relation equation 3.23 can be derived. This relation can be integrated between the static and stagnation conditions to give the compressible flow relation between the stagnation and static pressure shown in equation 3.24. Combining equation 3.22 with equation 3.24 the relation for the stagnation pressure and density can be derived. The static to total ratio for the pressure and density is given by equation 3.25 and 3.26 respectively.

$$\frac{dp}{p} = \frac{C_p}{R}\frac{dT}{T} = \frac{dT}{T}\frac{\gamma}{\gamma - 1} \tag{3.23}$$

$$\frac{P_0}{P} = \left(\frac{\rho_0}{\rho}\right)^{\gamma} = \left(\frac{T_0}{T}\right)^{(\frac{\gamma}{\gamma-1})} \tag{3.24}$$

$$\frac{P_0}{P} = \left(1 + \frac{\gamma - 1}{2} M^2\right)^{\gamma/(\gamma-1)} \tag{3.25}$$

$$\frac{\rho_0}{\rho} = \left(1 + \frac{\gamma - 1}{2} M^2\right)^{1/(\gamma-1)} \tag{3.26}$$

3.1.12. Dimensionless stage analysis

Each stage of the compressor or turbine can be categorized according to a few dimensionless parameters. These parameters are; the degree of reaction, the flow coefficient, and the stage loading coefficient. By using the dimensionless parameters, it is possible to predict the performance of the stages.

3.1.13. Degree of reaction

The degree of reaction of a stage provides the measure of the contribution of the rotor to the overall static pressure rise in the stage. The degree of reaction of a rotor stage is defined in terms of enthalpy rise as follows:

$$\Lambda = \frac{h_2 - h_1}{h_3 - h_1} \tag{3.27}$$

3.1.14. Flow coefficient

The flow coefficient is a measure of the flow capacity of the stage. It is defined by the axial component of the flow non-dimensionalized by the rotational velocity. The flow coefficient is defined by equation 3.28.

$$\phi = \frac{C_{ax}}{U} \tag{3.28}$$

3.1.15. Loading coefficient

The loading coefficient gives the measure of work capacity of the stage. It is defined as the total enthalpy increase of a stage divided by the square of the rotational velocity, equation 3.29 gives the mathematical definition.

$$\psi = \frac{\Delta h_0}{U^2} \tag{3.29}$$

For a purely axial turbine with a constant radius, the stage loading can be written as equation 3.30 where Δc_θ represents the change in the tangential component of the absolute velocity through the rotor.

$$\psi = \frac{\Delta c_\theta}{U} \tag{3.30}$$

3.1.16. Smith's chart

The Smith Chart is a representation of the stage performance based on the stage loading and flow coefficient. It was first published in 1965 by Smith [51] and is shown in figure 3.8. In the diagram, the constant total-to-total efficiency lines are plotted as a function of the stage-loading coefficient and the flow coefficient. The data used to create the diagram is obtained from 70 Rolls-Royce aircraft turbine engines. The Smith chart provides efficiency estimates based on the assumptions of constant axial velocity, reactions from 0.2 to 0.6, relatively large blade aspect ratios, and not taking into account the tip leakage losses and cooling [7].

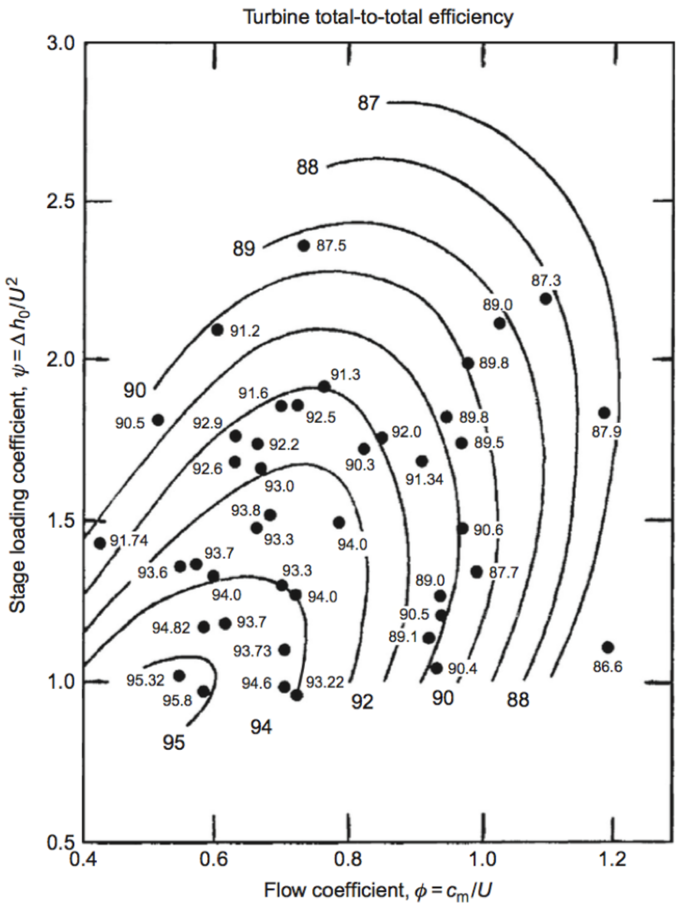

Figure 3.8: Smith Chart. Source:[7]

Based on the Smith chart, it can be concluded that stage efficiency when decreases as the loading coefficient increases, and that the stage efficiency decreases as the flow coefficient increases. From that, the maximum efficiency is located at low load factor and low flow coefficient.

3.1.17. Stage efficiency

The isentropic efficiency (η_{is}) for both compressor or turbine is defined as the ratio of the actual work and the isentropic case. The downside of using isentropic efficiency is that it can be misleading when components of different pressure ratios are compared [7]. To solve this problem the polytropic efficiency (η_{poly}) has been introduced. In the calculation of the polytropic efficiency, the component is divided into numerous small steps with each step containing similar isentropic efficiency. It does not depend upon the thermodynamic effect, and hence, it is considered as the aerodynamic performance of the compressor. Polytropic and isentropic efficiency are related through equation 3.31 and 3.32 for compressor and turbine respectively.

$$\eta_{is} = \frac{PR^{\frac{\gamma-1}{\gamma}} - 1}{PR^{\frac{\gamma-1}{\gamma\eta_{poly}}} - 1} \tag{3.31}$$

$$\eta_{is} = \frac{1 - PR^{\frac{(1-\gamma)\eta_{poly}}{\gamma}}}{1 - PR^{\frac{1-\gamma}{\gamma}}} \tag{3.32}$$

3.1.18. Engine performance parameters

The performance of a gas turbine can be measured using various parameters. This section attempts to make a selection of the most important performance parameters for aero-engines.

Specific thrust

The mass flow of air $\dot{m}_0$ that enters the gas turbine is defined by the size of the intake. The magnitude of the thrust produced is directly proportional to the mass flow rates of the fluid flow through the engine. Therefore it is interesting to study the thrust per mass flow rate as a measure of performance. The specific thrust can be calculated using equation 3.33.

$$F_s = \frac{F}{\dot{m}_0} \tag{3.33}$$

Thrust specific fuel consumption

One of the most important measures for aircraft propulsion is the TSFC, equation 3.34 gives the mathematical definition. The TSFC provides a measure of fuel efficiency per thrust force. The TSFC is for airline operators, perhaps the most important parameters as it provides a measure of fuel efficiency.

$$SFC = \frac{\dot{m}_f}{F} \tag{3.34}$$

Thermal efficiency

The ability of a propulsive system to convert the thermal energy of the fuel used into net kinetic energy gain of the working medium is called the thermal efficiency η_{th}. The formula to calculate the thermal efficiency is given in equation 3.35.

$$\eta_{th} = \frac{\frac{1}{2}\dot{m}_8 \cdot V_8^2 - \frac{1}{2}\dot{m}_0 \cdot V_0^2}{\dot{m}_f FHV} \tag{3.35}$$

Propulsive efficiency

The ratio between the net mechanical energy of the turbine and the thrust is the propulsive efficiency η_p, equation 3.36 provides the definition.

$$\eta_p = \frac{F \cdot V_0}{\dot{m}_8 \frac{1}{2}(V_8^2 - v_0^2)} \tag{3.36}$$

By replacing the thrust power ($F \cdot V_0$) with the uninstalled thrust power and not taking the fuel flow rate into account, which is a small fraction (~ 2 %) of the total air flow[52], equation 3.36 can be rewritten into:

$$\eta_p \approx \frac{2}{1 + \frac{V_8}{V_0}} \tag{3.37}$$

The propulsive efficiency is now only expressed in terms of the jet-to-flight velocity ratio (V_8/V_0). From this relation, it can be observed that velocity increment is beneficial for high propulsive thrust. Mathematically it is possible to calculate a 100% or even higher efficiency if the velocity ratio is smaller than unity. However, in that case, no thrust is generated, or the engine is even decelerating mass flow. The turbofan engine achieves high propulsive efficiency based on moving a large airflow at a relatively low speed.

Overall efficiency

The overall efficiency of the engine is the product of the thermal efficiency and the propulsive efficiency, which can best be described as the fraction of the thermal energy of the fuel converted into thrust work.

$$\eta_o = \eta_{th} \cdot \eta_p = \frac{F \cdot V_0}{\dot{m}_f \cdot FHV} \tag{3.38}$$

Thrust to weight ratio

The engine thrust to weight ratio is defined as the thrust generated by the engine divided by the engine weight, as shown in equation 3.39. A high thrust to weight ratio is desired and is a good indicator of performance.

$$TW = \frac{T}{W} \tag{3.39}$$

3.2. Intake design

The intake is the first component of the engine, and its goal is to guide the airflow to the engine face. According to literature, the airflow must be slowed down to Mach number of 0.5 at the engine face [6]. This will be achieved using a diffuser in the intake that is specially designed to minimize the losses caused by friction and flow separation.

3.2.1. Design methodology

The Matlab function *intake_des* has been developed to calculate the geometry of the intake and estimate the intake pressure recovery based on the geometry. A list of input variables for the function is given in Table 3.1. The function will require thermodynamic properties, intake design variables, and the free-stream Mach number. The first six input variables in Table 3.1 will be assumed to be constant during the analysis. The flowchart of *intake_des* is shown in Figure 3.9. For the estimation of the total pressure loss coefficient, a complex model by ESDU[12] has been used. The model is elaborated upon in Appendix A.

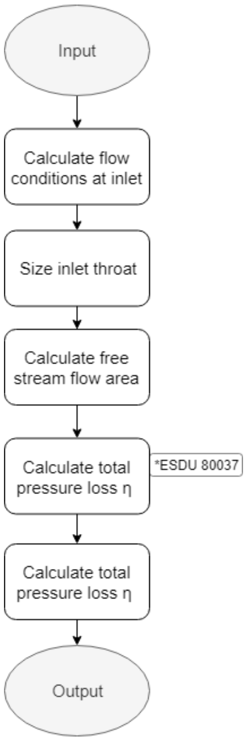

Figure 3.9: Flowchart of the function *intake_des*.

Table 3.1: List of input parameters for *Intake_des*.

Variable	Symbol	Units
Throat design Mach number	M_{tdes}	[-]
Intake length over diameter ratio	LD_{in}	[-]
Ratio of constant section length over total length	L_{csl}	[-]
Engine face design Mach number	M_{fdes}	[-]
Design maximum corrected mass flow rate	$\dot{m}_{max}$	[kg/s]
Entry contraction ratio	λ_c	[-]
Inflow angle	α	[deg]
Free-stream Mach number	M_0	[-]
Corrected mass flow rate	$\dot{m}_c$	[kg/s]
Inflow total pressure	p_{t0}	[pa]
Inflow total temperature	T_{t0}	[K]

Corrected mass flow rate

With dimensionless parameters, different flight conditions can be compared. The quantities of pressure and temperature can be normalized by diving each by their respective standard sea-level static values. These normalized values can be used to express the corrected mass flow rate, which is the mass flow that would pass through a device (e.g. compressor, bypass duct, etc.) if the inlet pressure and temperature corresponded to ambient conditions at Sea Level, on a Standard Day [6]. The corrected mass flow rate can be calculated as follows:

$$m_{c\dot{o}rr} = \dot{m} \cdot \frac{\sqrt{T/T_{0sd}}}{P/P_{0sd}} \tag{3.40}$$

Inlet sizing

The throat diameter of subsonic inlets will be sized such that the maximum Mach number does not exceed 0.8 at the throat location based on one-dimensional flow. This will ensure some margin for growth or error since the one-dimensional Mach number at the throat corresponding to actual inlet choke is about 0.9 [6]. The throat diameter corresponding to the specified conditions can be calculated using Equation 3.41. The maximum corrected mass flow rate for the intake design will be used.

$$D_{th} = \sqrt{\frac{4}{\pi}\left(\frac{\dot{m}_{c0,max}\sqrt{(T_{t0})}}{P_{t0}}\right)\frac{1}{MFP_{@M=0.8}}} \tag{3.41}$$

The mass flow parameter (MFP) used in Equation 3.41 will be calculated as:

$$MFP = \sqrt{\frac{\kappa}{R}} \cdot M \cdot \left(1 + \frac{\gamma - 1}{2}\right)^{\frac{\gamma+1}{2(1-\gamma)}} \tag{3.42}$$

Intake total pressure loss

The estimation of the intake pressure loss will make use of the model by *ESDU 80037, Pressure recovery of axisymmetric intakes at subsonic speeds*. This model takes into account lip losses due to flow separation, friction losses due to the diffuser, and interaction losses between entry and diffuser. The model is elaborated upon in Appendix A, with the flowchart of this model begin shown in Appendix A Figure A.1. The intake will be designed for an engine face (location 2 in Figure 2.1) Mach number of 0.50 and a maximum throat Mach number of 0.80. Several geometrical design parameters required for the ESDU model, e.g. LD_{in}, will be based on actual engine characteristics.

3.3. Compressor design

The compressor is the rotation component of the engine where work will be added to the working fluid to reach the desired pressure. The compressor usually consists of a series of compressor stages, and each stage consists of two rows of blades. The first row in a compressor stage consists of rotor blades, which accelerate the flow. The second row consists of stator blades wherein the kinetic energy transferred into static pressure. Due to the adverse pressure gradient in the compressor stage and diffusion, every stage can only provide a small pressure ratio. The effect can be seen by the number of compressor stages on an engine when compared to the number of turbine stages.

3.3.1. Compressor design procedure

The compressor is designed for to pressure ratio while satisfying all the design constraints. The Matlab optimizer *fmincon* will be used to find a feasible solution with the minimum number of stages while maximizing efficiency. The flowchart of the compressor design process is shown in figure 3.10. The procedure requires some input variables, and these include thermodynamic and geometrical properties from the previous engine component along with several design variables. Table 3.2 provides the complete with list of required input variables. In the design procedure, an estimation of the number of stages will be made based on the input variables, the upstream conditions, annulus geometry, and the rotational speed. The stage estimation is further elaborated upon in Section 3.3.2. The number of stages and the input variables will be fed to the optimizer *fmincon*, which in turn will start the compressor design. The optimizer will change the absolute rotor flow exit angle ($\alpha 2$) & absolute stator flow exit angle ($\alpha 3$). The design of the rotor and stator is done with the developed functions *comprotor* & *compstator* respectively, these two functions are discussed in more detail in Section 3.3.3. The resulting compressor design is checked with the design constraints. If the design does not satisfy the design constraints, the absolute flow angles $\alpha 2$ & $\alpha 3$ will be altered for the next iteration until a solution within the constraint limitations can be found. It can happen the optimizer is not able to find a feasible solution for the initially estimated number of stages. In this case, one extra stage will be added, and the whole procedure to find a feasible solution will be started again.

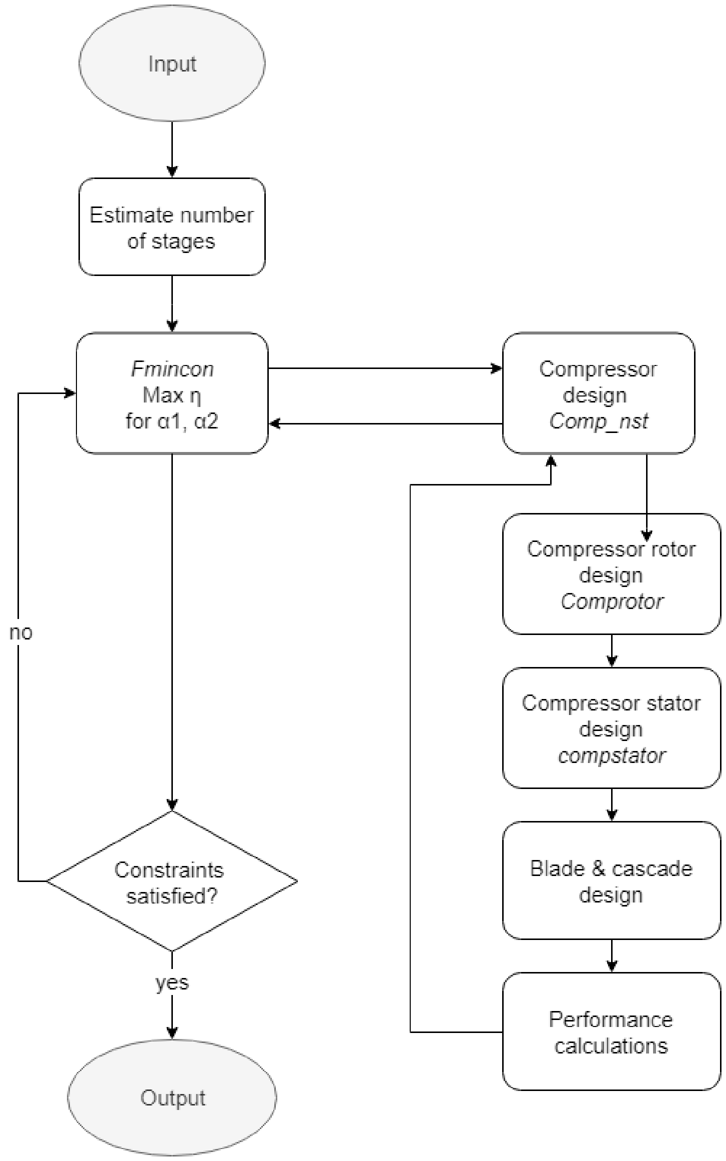

Figure 3.10: Flowchart of the compressor design module.

Table 3.2: List of input variables for the compressor design procedure.

Variable	Symbol	Units
Number of stages	n_{stages}	[-]
Design pressure ratio	PR	[-]
Mass flow rate	$\dot{m}$	[kg/s]
Angular velocity	Ω	[rad/s]
Inlet flow angle	α_1	[deg]
Inlet absolute velocity	C_1	[m/s]
Inlet pressure	p_1	[pa]
Inlet temperature	T	[K]
Hub-to-tip ratio	HTR_1	[-]
Inlet area	A_1	$[m^2]$
Inlet mean radius	r_{m1}	[m]
Blade aspect ratio	AR	[-]
Blade taper ratio	λ	[-]
Thickness-to-chord ratio	t/c	[-]
Maximum camber location	a/c	[-]
Blade clearance gap	τ	[m]
Blade axial spacing	FSP	[-]
Blockage factor	BLK	[-]
Rotor absolute flow angle	α_2	[deg]
Stator absolute flow angle	α_3	[deg]
Maximum loading coefficient	ψ_{max}	[-]

Optimizer design variables

Earlier it has been mentioned the optimizer *fmincon* will find a design solution where the efficiency is maximized while satisfying the design constraints for the minimum amount of stages. The design variables to be altered are shown in Table 3.3 with their corresponding boundaries range. Currently, only the absolute flow angles $\alpha 2$ & $\alpha 3$ are changed during the optimization. Obviously, more design variables can be included to increase the design space, and possibly find a more optimal solution. However, this would considerably increase the computational time. For the selected design variables, upper and lower bounds are set to limit the design space by excluding unfeasible and unrealistic design solutions.

Table 3.3: Design variables for compressor design.

x_i	Parameter	LB	UB	Unit
$x_1 : x_{n_{stages}}$	α_1	0	75	$[^0]$
$x_{n_{stages+1}} : x_{2n_{stages}}$	α_2	5	70	$[^0]$

Design constraints

The constraints limit the design space by excluding options that do not satisfy the design requirements. In the Matlab solver *fmincon* it is possible to set two types of constraints:

Inequality constraints $G_i \leq 0$

Equality constraints $G_i = 0$

The compressor design function is subject to the constraints shown in Table 3.4. These constraints ensure the design is feasible and operable. The deHaller number is a measure of flow diffusion. At low deHaller numbers, flow separation can occur, which leads to compressor stall or surge. The deHaller number for both the rotor and stator blades is limited to a minimum value of 0.60, Dixon [7] proposed a value of 0.72 to provide an adequate margin for the diffusion. However, using the value of 0.72 for the HPC led to unrealistic designs. In the HPC design, the value was lowered to 0.60, while for the LPC the value was kept at 0.72. The relative inlet Mach number is limited at 1.60 to limit losses due to shock-waves. The loading coefficient is limited at 2.50, which is reasonable for the current level of technology [5].

Table 3.4: Design constraints for compressor design.

Parameter	Description	Inequality/equality	Value	Unit
PR	Pressure ratio	=	PR_{des}	[-]
DH	deHaller number	≥	0.72/0.60	[-]
MW_1	Relative Mach number at inlet	≤	1.60	[-]
ψ	Loading coefficient	≤	2.50	[-]

3.3.2. Estimation of number of stages

For the compressor design, the first step is to estimate the number of compressor stages. For the estimated number of stages, the compressor stages are designed, and the resulting design is checked with the requirements and constraints. If for the given number of stages, no feasible solution can be found by the optimizer, the number of stages will be increased until a solution is found.

For the estimation of the number of stages, an initial guess for the polytropic efficiency and the outlet total temperature is made. Using the inlet temperature and the desired pressure ratio, a new outlet temperature can be found with the use of equation 3.43. Iteratively the outlet temperature will be updated, and this will lead to changes in the heat capacity and thus also the outlet temperature. The calculations for the total outlet temperature are performed till convergence, then the total enthalpy change or the total temperature change is known. The outlet total temperature will be used to calculate the specific heat capacity, which in turn will be used for the estimation of the number of stages.

$$T_{t,out} = PR^{\frac{\kappa-1}{\eta_p \kappa}} \cdot T_{t,in} \tag{3.43}$$

Using equation 3.44, the number of stages can be estimated based on the maximum loading coefficient ψ_{max}, the rotational speed, and the earlier calculated total temperature change. In this estimation, the rotational speed will be calculated using the shaft rotational speed, and the inlet mean radius. The rotational speed U will be assumed to be constant for the number of stages estimation. Obviously, for the actual compressor design without a constant mean radius, the mean rotational speed will vary.

$$n_{stages} = \frac{Cp\Delta T}{\psi_{max} \cdot U^2} \tag{3.44}$$

3.3.3. Stage design

For the compressor design, a rotor and a stator design function have been developed named *Comprotor* and *Compstator* respectively. The two functions are very similar in terms of flow-path but do have fundamental changes because of the differences between rotor and stator. The output of the stage design functions will be the thermodynamic properties, geometric properties, and the velocity triangle results. All these results will be stored in the stg. structure as described in section 3.3.4.

Only the flowchart of *Comprotor* will be discussed as the flow-path of the function is almost similar to *Compstator*. The only differences are in the velocity triangle calculations and the loss model for the two functions. This is due to the fundamental difference between a rotor and a stator, but the overall steps are similar. The flowchart of the function *Comprotor* is shown in Figure 3.11. A list with all the input variables is shown in Table 3.5. This list includes data from the previous station and several fixed design parameters.

In *Comprotor* (3.11) both the entropy change(Δs) and mean radius (r_{m2}) are initially guessed. Based on the mean radius, the velocity triangle calculations can be performed. Following the results from the velocity triangle calculations, the geometrical properties will be calculated. The newly calculated mean radius ($r_{m2_{new}}$) will be compared to the initial guess. If the difference is larger than the error tolerance, then the initial guess will be updated with the calculated value, and the steps are retaken till convergence is reached. The blade calculations and the pressure loss calculations are next after the geometry calculations. Empirical models will be used to estimate total pressure loss of the blade row. These models are elaborated on in section 3.3.6. Finally, the actual stage entropy change will be calculated, and compared to the initial guess, if the error exceeds the error tolerance, then the initial guess will be updated. The whole calculation starts over again with a new entropy change(Δs) estimate.

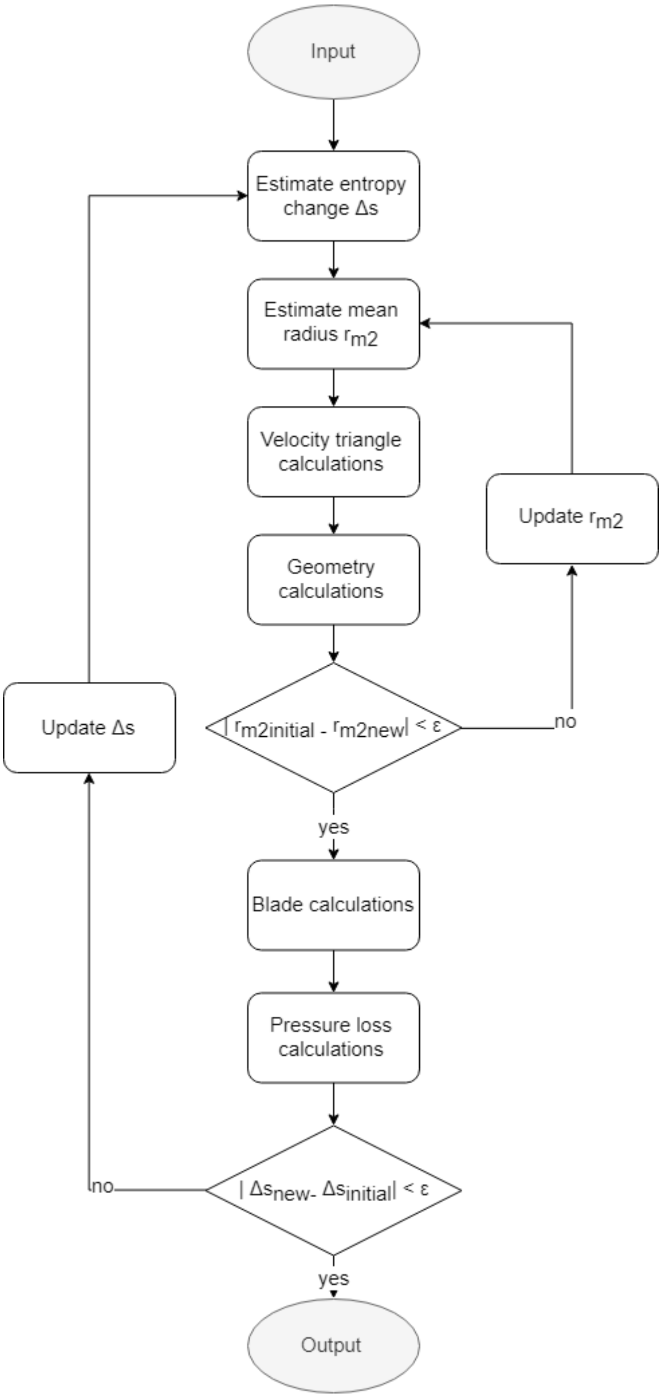

Figure 3.11: Flowchart of the function *Comprotor*.

Table 3.5: List of input parameters for *Comprotor*

Variable	Symbol	Units
Stage properties previous stage	stg.	[-]
Mass flow rate	$\dot{m}$	[kg/s]
Angular velocity	Ω	[rad/s]
Velocity station	vt	[-]
Geometry station	geom	[-]
Aero station	aero	[-]
Blade aspect ratio	AR	[-]
Blade taper ratio	λ	[-]
Thickness-to-chord ratio	t/c	[-]
Maximum camber location	a/c	[-]
Blade clearance gap	τ	[m]
Blade axial spacing	Fsp	[-]
Blockage factor	BLK	[-]
Axial velocity ratio	AVR	[-]
Compressor rotor absolute exit flow angle	α_2	[deg]

Velocity Triangle

In the *Velocity triangle calculations* block of *Comprotor* the velocity triangle will be designed using equations 3.45 - 3.50.

$$C_{ax2} = C_{ax1} \cdot AVR \tag{3.45}$$

$$U_2 = \Omega \cdot r_{m2} \tag{3.46}$$

$$C_2 = C_{ax2}/cos(\alpha 2) \tag{3.47}$$

$$C_{th2} = C_{ax2} - U_2 \tag{3.48}$$

$$\beta_2 = atan\left(\frac{W_{th2}}{C_{ax2}}\right) \tag{3.49}$$

$$W_2 = \sqrt{W_{th2}^2 + C_{ax2}^2} \tag{3.50}$$

The rothalpy defined earlier in equation 3.9 remains constant over the rotor. Using the rothalpy equation the static and total enthalpy, h_2 and h_{02} can be found by equations 3.51 & 3.52.

$$h_2 = I_2 - \frac{1}{2}W_2^2 + \frac{1}{2}U2^2 \tag{3.51}$$

$$h_{02} = h_2 + \frac{1}{2}C_2^2 \tag{3.52}$$

Finally the area at rotor outlet station can be found using equation3.53.

$$A_2 = \frac{\dot{m}}{C_{ax2}\rho_2 BLK} \tag{3.53}$$

3.3.4. Data structure

For the storage of the calculation results structures matrices have been used. Each compressor or turbine stage will share the same data structure for consistency. The structure is shown in figure 3.12. The geometrical properties are stored in **stg.geom**, the aerodynamic properties in **stg.aero**, the velocity triangle in **stg.vt**, the blade properties in **stg.blade** and lastly the stage characteristics in **stg.props**. In Appendix B the individual tabs of stg. will be elaborated further upon.

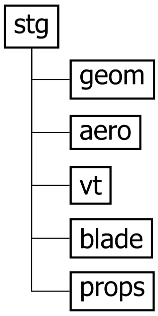

Figure 3.12: Stage data structure.

3.3.5. Blade calculations

The optimum blade solidity (s/c), will be estimated using cascade data on profile loss coefficient. In Figure 3.13 the 'optimum' pitch/chord ratio design curves for minimum profile loss are shown. The design curves are only based on profile loss. Therefore the pitch/chord ratios do necessarily result in the lowest total pressure loss coefficient.

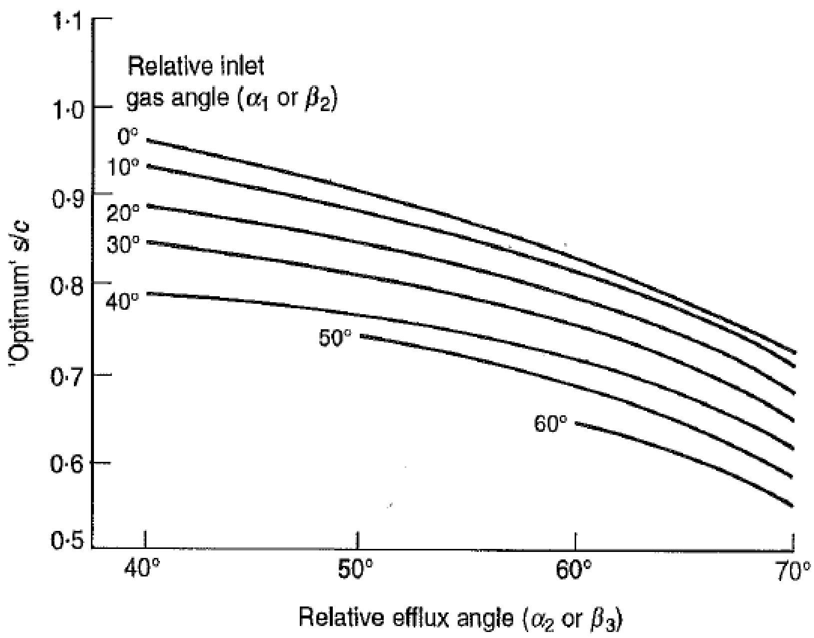

Figure 3.13: Optimumpitch-chord ratio for minimum profile drag. Source:[8]

The number of blades can be calculated using the blade solidity and the geometry. The number of blades will be calculated using Equation 3.54.

$$z_{bl} = \frac{2\pi r_m \sigma}{h} AR \tag{3.54}$$

The blade spacing can be calculated as well using the number of blades, this follows from:

$$s = (2\pi r_m)/z_{bl} \tag{3.55}$$

The blade chord at mid-span will follow from:

$$c = \sigma \cdot s \tag{3.56}$$

Free vortex Design

The free vortex design controls the radial variation of the swirl component to distribute the work over the blade span evenly. The rotational velocity increases with the increasing blade height. Therefore the velocity triangle will be different along the blade. The following equation describes the free vortex method:

$$r \cdot C_{th} = constant \tag{3.57}$$

3.3.6. Compressor pressure loss

In order to give an accurate representation of the performance of the compressor, loss models have been implemented in the tool. The 2D empirical loss models will estimate the total loss parameter w, which is the ratio of loss in stagnation pressure over the dynamic inlet pressure. Equation 3.58 shows the mathematical definition of the loss parameter w.

$$w = \frac{\Delta p_t}{p_{t1} - p_1} \tag{3.58}$$

In Tournier & El-Genk [53] the loss coefficient consist of five different loss sources which add up to the total loss coefficient as shown in Equation 3.59.

$$w = w_{pro} + w_{sec} + w_{end} + w_{tc} + w_{shock} \tag{3.59}$$

Profile loss

Lieblein [54] has defined the following empirical relation for the blade profile loss coefficient as:

$$w_{pro} = 2\left(\frac{\theta_2}{c}\right)\frac{\sigma}{cos\beta_2}\left(\frac{cos\beta_1}{cos\beta_2}\right)^2\left(\frac{2H_{TE}}{3H_{TE}-1}\right)\left[1-\left(\frac{\sigma_2}{c}\right)\frac{\sigma H_{TE}}{cos\beta_2}\right]^{-3} \tag{3.60}$$

The boundary layer momentum thickness at the blade outlet in dimensionless form is given by as:

$$\frac{\theta_2}{c} = \frac{\theta_2^0}{c} \cdot \zeta_M \cdot \zeta_H \cdot \zeta_{Re} \tag{3.61}$$

The boundary layer trailing-edge shape factor, H_{TE}, is defined as the ratio of the boundary layer displacement thickness to the momentum thickness expressed as:

$$H_{TE} = H_{TE}^0 \cdot \xi_M \cdot \xi_H \cdot \xi_{Re} \tag{3.62}$$

The parameters θ_2^0 and H_{TE}^0 are reference values for nominal conditions. These conditions refer to inlet Mach numbers, Ma_1 < 0.05, no contraction in the height of the flow annulus, an inlet Reynolds number of $Re_{1C} = 10^6$ and hydraulically smooth blades. Koch and Smith [55] provide empirical correlations for the boundary layer momentum thickness and the boundary layer trailing edge shape factor for the nominal flow conditions. The correlations are given by equations 3.63 and 3.64 respectively.

$$\frac{\theta_2^0}{c} = 2.644 \cdot 10^{-3} D_{eq} - 1.519 \cdot 10^{-4} + \frac{6.713 \cdot 10^{-3}}{2.60 - D_{eq}} \tag{3.63}$$

$$H_{TE}^0 = \frac{\delta_{TE}^*}{\theta_2^0} = (0.91 + 0.35 D_{eq})[1 + 0.48(D_{eq} - 1)^4 + 0.21(D_{eq} - 1)^6] \tag{3.64}$$

In the case $D_{eq} > 2.0$ a value of $H_{TE}^0 = 2.7209$ will be used. For the conditions other than the nominal conditions by Koch and Smith have developed correction factors for the momentum thickness to correct for Mach number ζ_M, contraction ratio ζ_H and Reynold's number $\zeta_R e$. The following correlations are presented:

$$\zeta_m = 1 + (0.11757 - 0.16983 D_e q) M_1^n \tag{3.65}$$

$$n = 2.853 + D_{eq}(-0.97747 + 0.19477 D_{eq}) \tag{3.66}$$

The correction factor for the flow area contraction ratio is given by:

$$\zeta_H = 0.53 \frac{H_1}{H_2} + 0.47 \tag{3.67}$$

An approach proposed by Aungier [56] approximates the Reynolds corrected factor well. Angier introduced the critical blade chord Reynolds number above which the effect of roughness becomes significant, the value is set at $Re_{cr} = \frac{100c}{\kappa}$. In the case the $Re_{1C} < Re_{cr}$ the correction factor is expressed as:

$$\zeta_{Re} = \begin{cases} (\frac{10^6}{Re_{1C}})^{0.166}, & \text{for } Re_{1C} \geq 2 \cdot 10^5 \\ 1.30626(\frac{2 \cdot 10^5}{Re_{1C}}), & \text{for } Re_{1C} < 2 \cdot 10^5 \end{cases} \tag{3.68}$$

In the case the $Re_{1C} > Re_{cr}$ the friction losses are dominated by the surface roughness, for this case the correction factor is given by:

$$\zeta_{Re} = \begin{cases} (\frac{10^6}{Re_{cr}})^{0.166}, & \text{for } Re_{cr} \geq 2 \cdot 10^5. \\ 1.30626(\frac{2 \cdot 10^5}{Re_{cr}}), & \text{for } Re_{cr} < 2 \cdot 10^5. \end{cases} \tag{3.69}$$

The correction factors (xi_m, xi_h and xi_{Re}) for the form factor shown in Equation 3.62 are accurately fitted by the following correlation described in Equations 3.70 - 3.72.

$$\xi_m = 1.0 + [1.0725 + D_{eq}(-0.8671 + 0.18043 D_{eq})] M_{a1}^{1.8} \tag{3.70}$$

$$\xi_h = 1.0 + (\frac{H_1}{H_2} - 1)(0.0026 D_{eq}^8 - 0.024) \tag{3.71}$$

$$\xi_{Re} = \begin{cases} (\frac{10^6}{Re_{1C}})^{0.06}, & \text{for } Re_{1C} < Re_{cr} \\ (\frac{10^6}{Re_{cr}})^{0.06}, & \text{for} Re_{1C} \geq Re_{cr} \end{cases} \tag{3.72}$$

The equivalent diffusion ratio, D_{eq}, used in the equations for the correction factors is presented in Koch and Smith [55] as:

$$D_{eq} = \frac{V_{1R}}{V_{2R}}\left[1 + K_3\frac{t_{max}}{c} + K_4\Gamma^*\right]\sqrt{(sin\beta_1 - K_1\sigma\Gamma^*)^2 + (\frac{cos\beta 1}{A^*_{\text{throat}}\rho_{\text{throat}}/\rho_1})} \tag{3.73}$$

Where the throat area contraction ratio ,A^*_{throat}, is defined as:

$$A^*_{\text{throat}} = \left[1.0 - \frac{K_2\sigma(\frac{t_{max}}{c})}{cos(\frac{\beta_1+\beta_2}{2})}\right]\frac{A_{throat}}{A_1} \tag{3.74}$$

In Tournier & El-Genk [53], the assumption is made that cascade throat area is assumed to occur at one-third of the axial chord. This leads to the following equation for the cascade throat area:

$$A_{throat} = A_1 - \frac{A_1 - A_2}{3} \tag{3.75}$$

The gas density ratio $\rho_{\text{throat}}/\rho_1$ used for the equivalent diffusion ratio is defined as:

$$\frac{\rho_{\text{throat}}}{\rho_1} = 1 - \frac{M_{x1^2}}{1 - M^2_{x1}}\left(1 - A^*_{throat} - K_1\sigma\Gamma^*\frac{tan\beta_1}{cos\beta_1}\right) \tag{3.76}$$

The constants K_i in Equations 3.73 - 3.76 are from the experimental data from Koch & Smith [55] and are shown in Table 3.6.

Table 3.6: Values for K_i constants.

Constant	Value [-]
K_1	0.2445
K_2	0.4458
K_3	0.7688
K_4	0.6024

The dimensionless circulation parameter, Γ^*, used in Equation 3.73 is given by Equation 3.77. Under the assumption that $r_{m1} = r_{m2} = r_m$ resulting into $U_{1m} = U_{2m} = U_m$ the equation for the circulation parameter can be simplified.

$$\Gamma^* = \frac{r_{1m}\cdot v_1 - r_{2m}\cdot v_2}{\sigma V_1\cdot(r_{1m} + r_{2m})/2} = (tan\phi_1 - tan\phi_2)\frac{cos\phi_1}{\sigma} \tag{3.77}$$

Secondary loss

The losses due to secondary flows are will be described by the correlation presented by Howell [57]. The secondary flow loss coefficient is described by Equation 3.78.

$$w_s = 0.018\sigma\frac{cos^2\phi_1}{cos^3\phi_m} \tag{3.78}$$

End wall loss

In Aungier [56] a modified Howell's model [57] has been developed to estimate end wall loss coefficient. In Equation 3.79 the correlation for the end wall loss coefficient is shown.

$$w_{end} = 0.0146\frac{c}{H}(\frac{cos\phi_1}{cos\phi_2})^2 \tag{3.79}$$

Tip clearance loss

The tip clearance loss Y_{TC} will be modeled using the approach presented by Yaras & Sjolander [58]. The loss will be separated into two components which are the blade tip and blade gap as shown in equation 3.80. The loss components, tip loss & gap loss, are given in equation 3.81 and 3.82 respectively.

$$w_{tc} = Y_{tip} + Y_{gap} \tag{3.80}$$

$$w_{\text{tip}} = 1.4K_e\sigma\frac{\tau}{H}\frac{\cos^2\beta_2}{\cos^3\beta_m}C_L^{1.5} \tag{3.81}$$

$$w_{\text{gap}} = 0.0049K_g\sigma\frac{C}{H}\frac{\sqrt{C_L}}{\cos\beta_m} \tag{3.82}$$

The theoretical blade lift coefficient C_L is given by AM and is shown in equation 3.124.

$$C_L = \frac{2}{\sigma}cos(\beta_m)[\tan(\beta_1) + \tan(\beta_2)] \tag{3.83}$$

Yaras and Sjolander have provided values for K_E and K_G for different blade loading types.

Mid-loaded blades: $K_E = 0.5$ and $K_G = 1.0$

Front- or aft-loaded blades: $K_E = 0.566$ and $K_G = 0.943$

Shock loss

If the blade tip speed of a compressor blades reaches sonic speeds, the shock losses must be taken into account. Boorsma [4] presented an empirical relation based on the data of Koch & Smith [55] to estimate the shock loss coefficient. This empirical relation is given in Equation 3.84.

$$w_shock = 0.375 - 0.75M_{1R} + 0.375M_{1R}^2 \tag{3.84}$$

Boorsma also presented a weighing method to account for the radial variation in Mach number over the blade. To better predict the shock losses, a weighted average is taken from the Mach number at blade mean radius and the Mach number at the blade tip as shown in Equation 3.85.

$$M_{1R,shock} = M_{1Rmean} + 0.9(M_{1Rtip} - M_{1Rmean}) \tag{3.85}$$

3.3.7. Cascade design

All the rotating engine components have stages consisting of stationary and rotating blade rows. The rotating rows depending on whether it is a compressor or turbine, will add or extract energy from the working fluid. In the stator, depending on the absolute velocity of the fluid is either decreased/increased to convert the energy into a static pressure increase/decrease.

A gap between the blades and the annulus must be present. For this research project, the tip clearance gap is assumed to be fixed at 5mm for the fan stage and 1mm for compressor & turbine stages.

For the fan and compressors, the following airfoil types are considered: Double Circular Arc (DCA), NACA 65-series airfoils (NACA), and British-C.4 airfoils (C4). These are considered common airfoil shapes for compressors, Figure 3.14 shows the airfoil shapes for 60^o camber angle and 10% thickness-to-chord ratio.

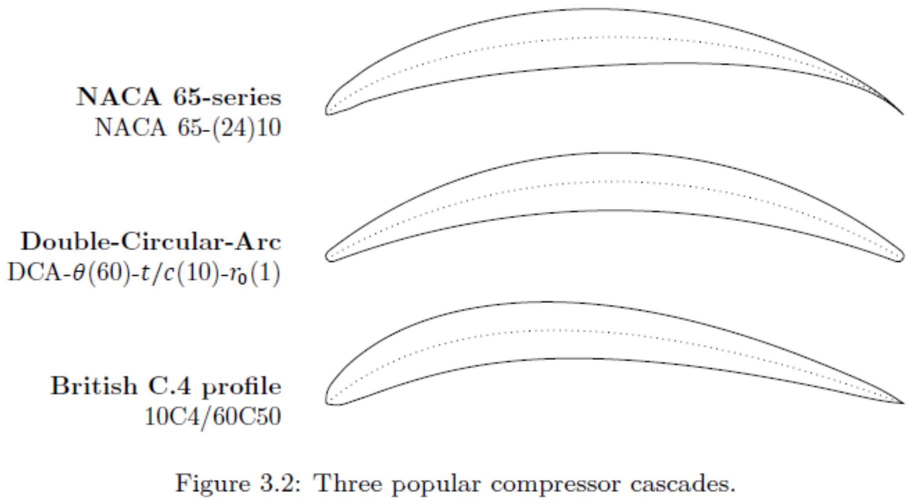

Figure 3.14: Three popular compressor cascades. Source:[1]

Cascade nomenclature

The cascade geometry is shown in figure 3.15, it is defined by the following geometrical parameters:

- β_1: Relative blade inlet angle
- β_1': Blade inlet angle
- β_2: Relative blade outlet angle
- β_2': Blade outlet angle
- i: Incidence angle
- γ: Stagger angle
- θ: Camber angle
- θ: Camber angle
- σ: Solidity C/S
- t: Thickness
- S: Stagger spacing
- C: Chord length
- t: Maximum thickness

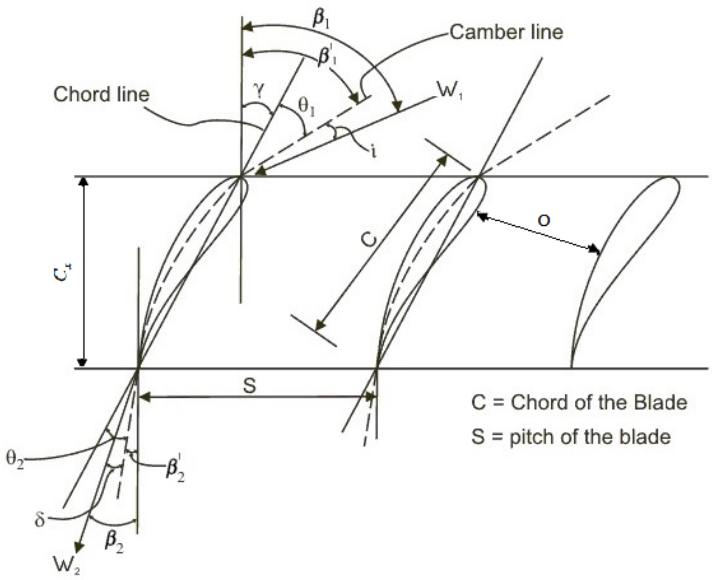

Figure 3.15: Compressor cascade. (Modified image from original source) Source:[6]

Incidence angle

The incidence angle is defined as the difference between the flow inlet angle and the blade camber line. The incidence angle has an influence on cascade losses. Several empirical models are available for the estimation of the optimum incidence angle where the losses are minimum. Tiemstra [1] has compared five different models with experimental data available from rotor measurements at the NASA Lewis Research Center. In total, four methods are compared, these include methods by Aungier [56], Howell [57], and Johnsen & Bullock [59]. In the work of Falck [60], a set of equations has been presented, originally introduced by Howard but based on the original correlations from Johnsen & Bullock. This method, originally by Howard, is also included in the comparison by Tiemstra. The results of his analysis are shown in Figure 3.16 & 3.17 for the rotor and stator respectively. Although Howell predicts the incidence angle most accurately, the mutual differences are minimal, and other methods show approximately similar results. The method used for the incidence angle estimation will be the method by Aungier. This method has been used in Tournier [53], where it led to accurate results when combined with the right deviation angle method.

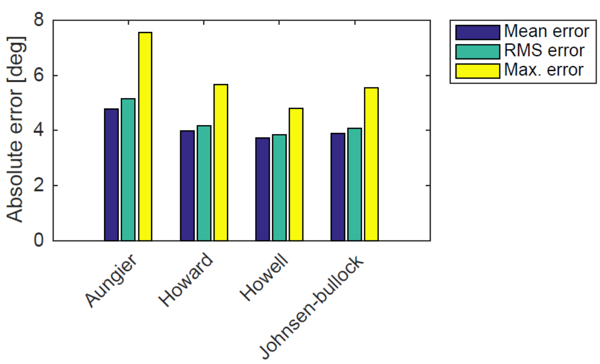

Figure 3.16: Comparison of rotor incidence angle prediction methods using NASA rotor data. Source:[1]

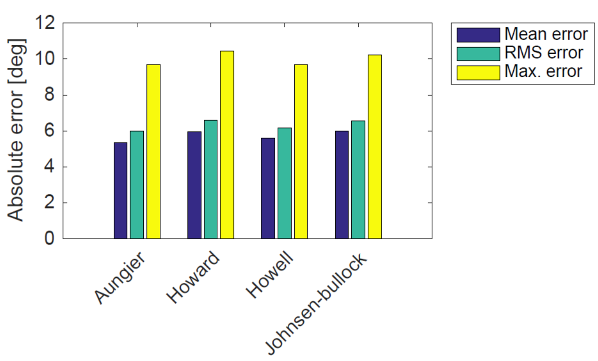

Figure 3.17: Comparison of stator incidence angle prediction methods using NASA stator data. Source:[1]

3.3.8. Deviation angle

In the ideal situation, the airflow will leave along the camber line of the blade at the trailing edge. In the real case, due to pressure differences between the upper and lower surface of the airfoil, the flow cannot follow the airfoil contours. The angle between the trailing edge metal angle, κ_2, and the relative exit flow angle,β_2, is defined as the deviation angle δ. Similar to incidence angle, several methods are available for the estimation of the deviation angle. In Tiemstra [1], a total of 9 methods have been compared. A similar comparison approach has been used for the incidence angle, the experimental rotor data available from rotor measurements at the NASA Lewis Research Center has been used again. The results of his analysis are shown in Figure 3.18 & 3.19 for the rotor and stator respectively. For both the rotor and the stator, the Johnsen and Bullock's methods showed the best estimations. This method, in combination with the Aungier's method for the incidence method, has been used by Tournier and proven to give accurate results.

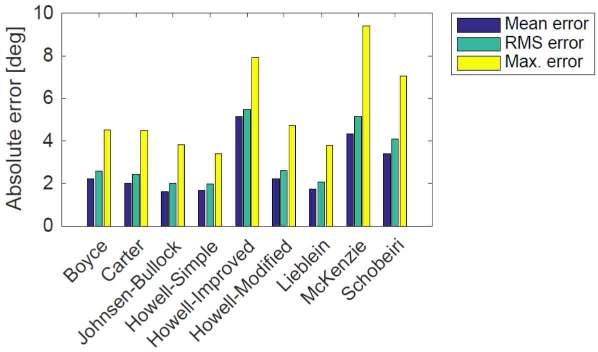

Figure 3.18: Comparison of rotor deviation angle prediction methods using NASA rotor data. Source:[1]

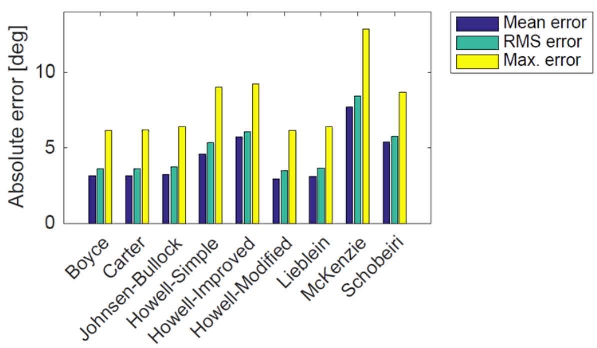

Figure 3.19: Comparison of stator deviation angle prediction methods using NASA stator data. Source:[1]

3.3.9. Cascade methodology flowchart

The blade cascade flow angles will be mainly calculated by *LPC blade angles*. This function uses free vortex design to calculate the blade hub and tip velocity triangles. The blade metal angles for minimum losses will be calculated using the airflow angles. The flowchart for this function is shown in Figure 3.20. The code will initially assume a deviation angle and incidence angle. Using the blade profile and Howell's method, the incidence angle is calculated and updated until the solution is converged. The deviation angle will be calculated using Johnsen & Bullock's method, and again the initial estimation will be updated till convergence.

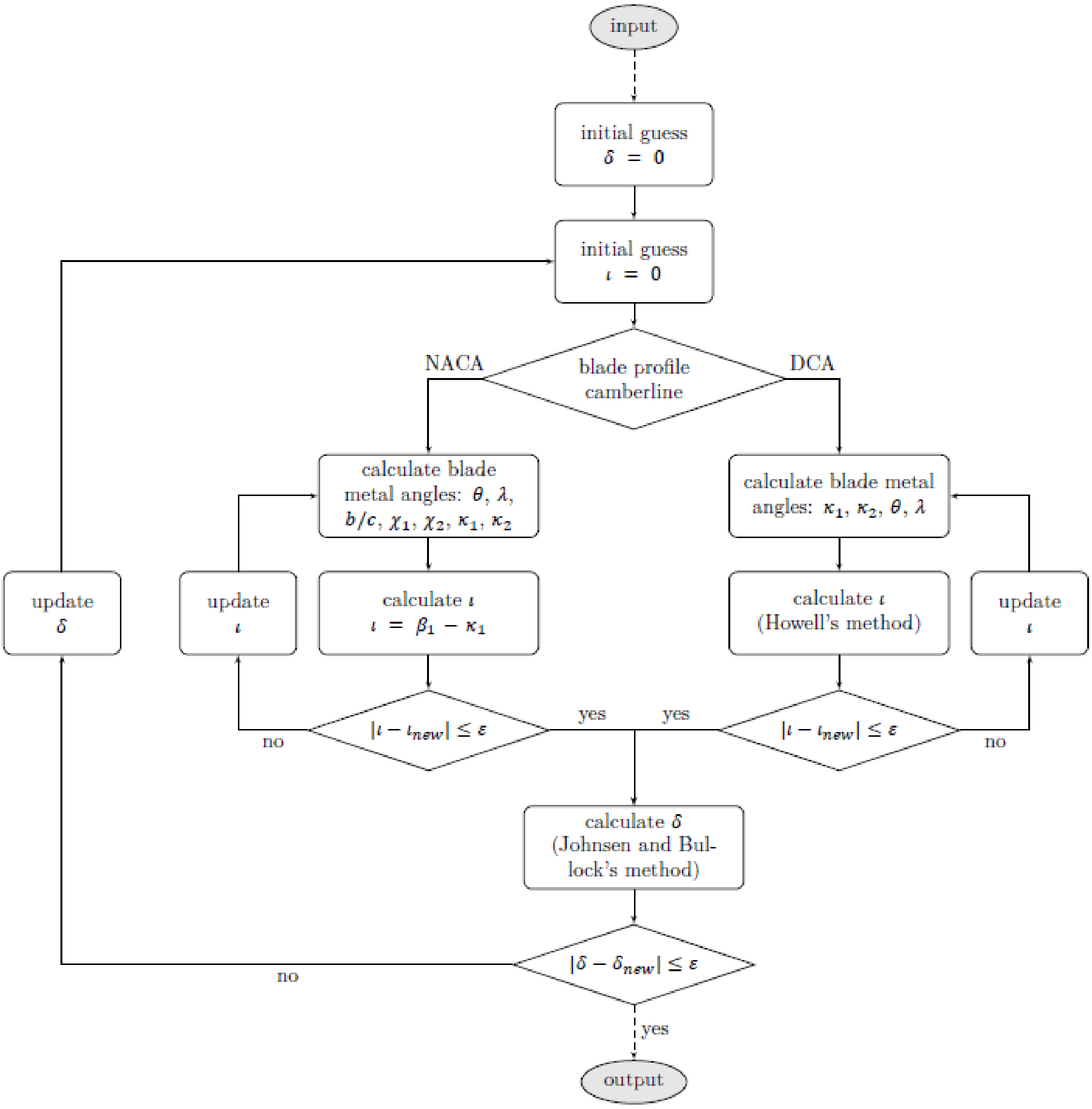

Figure 3.20: Flowchart of the iterative solving method for blade angles. Source:[1]

3.4. Turbine design

3.4.1. Turbine design procedure

The turbine will extract energy from the working fluid to deliver the power required to drive the compressor. The turbine and compressor are connected via a mechanical shaft, which has its efficiency. The mechanical efficiency, η_{mech}, is assumed to be fixed at 0.99.

Turbine design procedure

The most important requirement for the turbine will be the power requirement, which is based on the compressor (and fan) design. The turbine will be designed to meet the power requirement while satisfying other design constraints. Similar to the compressor design, the Matlab optimizer *fmincon* will be used to find a feasible design solution with the minimum amount of stages. The flowchart of the turbine design procedure is shown in figure 3.21, and the list of input variables is provided in Table 3.7.

The code will estimate the number of turbine stages required based on thermodynamics. For the estimated number of stages, the code will design the turbine stages using a stator and rotor design functions *Turbstator* & *Turbrotor* respectively. The optimizer will be alternating three design variables, namely; $\alpha 2$, $\alpha 3$ and M_2 till a feasible design solution is found. If for the estimated number of stages, no feasible solution can be found, one extra stage will be added. The optimizer will then start to find a feasible solution again.

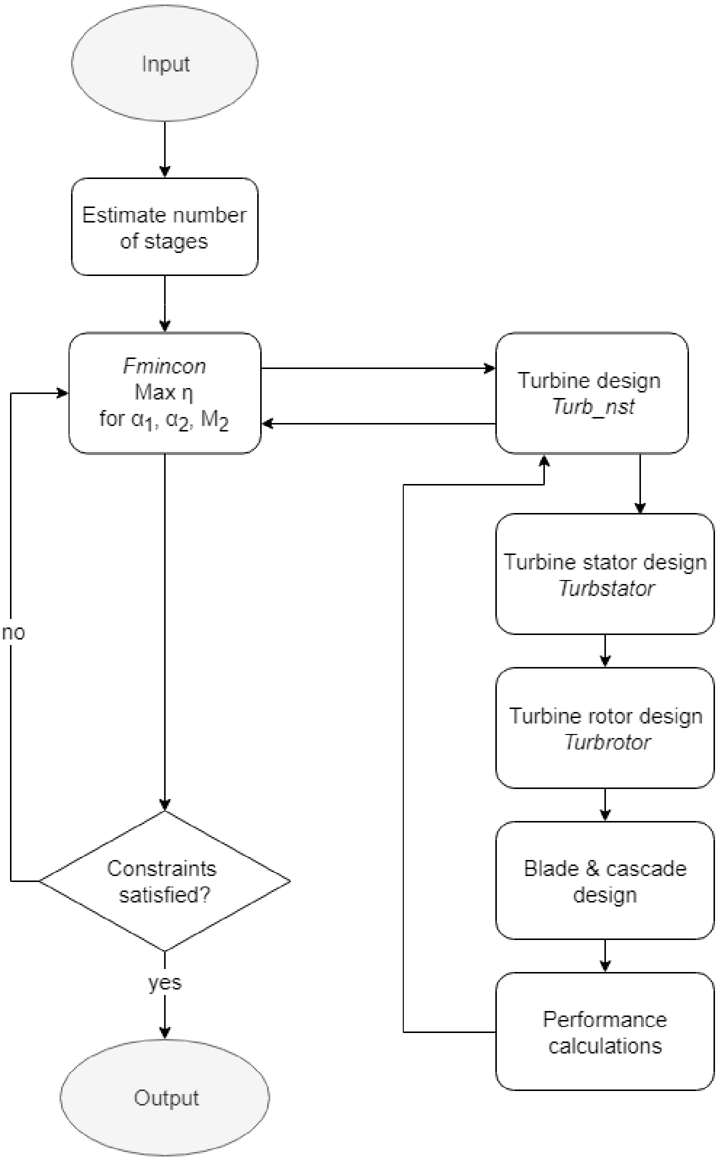

Figure 3.21: Flowchart of the turbine design methodology.

Table 3.7: List of input variables for the turbine design procedure.

Variable	Symbol	Units
Number of stages	n_{stages}	[-]
Power requirement	$\dot{W}$	[W]
Gas composition	$comp_{gas}$	[-]
Mass flow rate	$\dot{m}$	[kg/s]
Angular velocity	Ω	[rad/s]
Inlet flow angle	α_1	[deg]
Inlet absolute velocity	C_1	[m/s]
Inlet pressure	p_1	[pa]
Inlet temperature	T	[K]
Hub-to-tip ratio	HTR_1	[-]
Inlet area	A_1	[m^2]
Inlet mean radius	r_{m1}	[m]
Blade aspect ratio	AR	[-]
Blade taper ratio	λ	[-]
Thickness-to-chord ratio	t/c	[-]
Maximum camber location	a/c	[-]
Blade clearance gap	τ	[m]
Blade axial spacing	Fsp	[-]
Turbine stator absolute flow angle	α_2	[deg]
Turbine rotor absolute flow angle	α_3	[deg]
Absolute stator outlet Mach number	M_2	[-]
Maximum loading coefficient	ψ_{max}	[-]

3.4.2. Estimation of number of stages

The code will estimate the required number of turbine stages based on the power requirement. The power requirement follows from the compressor and, if applicable, also from the fan. The flowchart for the turbine stage estimation is given in figure 3.22. The sum of the total power requirement will be, after correcting for the mechanical efficiency, used to find the enthalpy change. The enthalpy of the fluid at the turbine exit follows from the power requirement using the mass flow rate and specific heat capacity. The total enthalpy change will be found using an iterative loop where the specific heat capacity, Cp_{out}, will be initially estimated and updated till convergence. This iterative loop is as follows. The turbine outlet temperature is estimated using equation 3.86. This exit temperature will then be used to find updated value for the specific heat capacity, Cp_{out}, which in turn will be used for the total enthalpy change required to deliver the required power. Finally, a new exit temperature will be found, which serves for the next iteration until the solution is converged.

$$T_{out} = (T_{in} \cdot Cp_{in} - h_{out})/Cp_{out} \tag{3.86}$$

The number of stages required can be estimated using equation 3.87. For the turbine there is a sign change compared to the compressor because of work extraction from the gas. The total required enthalpy change, Δh, follows from the thermodynamic calculations described earlier. The flowchart of the whole turbine stage estimation is shown in figure 3.22.

$$n_{stages^{\cdot}} = \frac{-\Delta h}{\psi_{max} \cdot U^2} \tag{3.87}$$

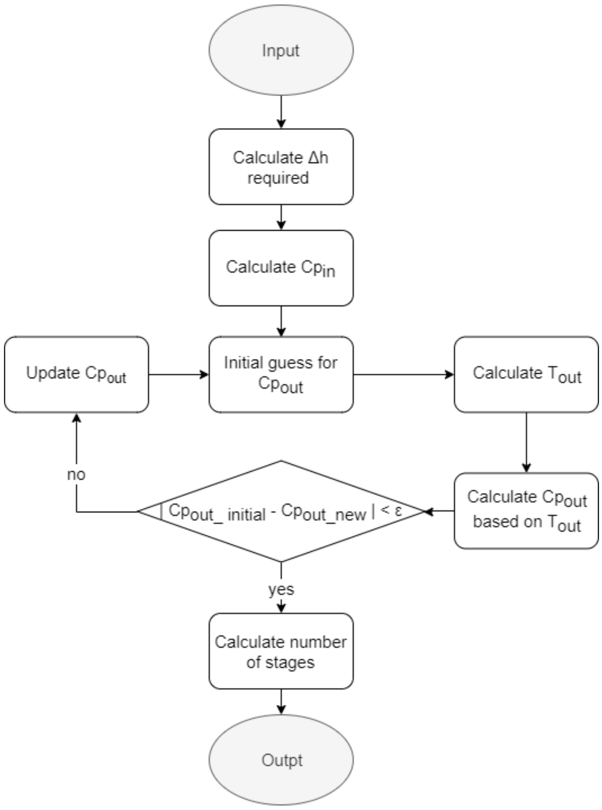

Figure 3.22: Flowchart of turbine stage number estimation procedure..

3.4.3. Stage design

Similar to the compressor stage design, two functions, *Turbstator* and *Turbrotor*, have been developed to design the stator and rotor respectively. The output of the stage design functions will be the stg. structure results as described in section 3.3.4 with the stage properties.

This time the flowchart of Turbstator will be discussed because of two reasons. Firstly, the Turbstator requires the absolute outflow angle and the absolute outlet Mach number instead of the outflow angle only, which is the case for *Turbrotor*. Secondly, the *Turbrotor* function is very similar to *Comprotor*, which has already been discussed earlier. The two functions share the same methodology and use the conservation of rothalpy for the calculations. The only main difference will be the pressure loss model used between the compressor and turbine rotor stage.

The flowchart of *Turbstator* is shown in figure 3.23 and the list of input variables for this function are shown in table 3.8. The *Turbrotor* is comparable and will have small differences due to the difference between a stator and a rotor. These differences mainly affect the velocity triangle calculations and pressure loss calculations.

The *Turbrotor* function will use an initial guess for the pressure loss coefficient($y12_{initial}$), entropy change($\Delta s_{initial}$) and mean radius($r_{m_{initial}}$) to start the calculations. The velocity triangle and geometrical properties of the stages will be calculated using the initial guesses. The calculations for the velocity triangle will be elaborated upon in Section 3.4.3. The calculated mean radius will be compared to the initial guess, if the difference exceeds the convergence criteria, $r_{m_{initial}}$ will be updated, and geometrical calculations start over again. When the mean radius is converged, the function will calculate the stage losses using empirical turbine pressure loss models. Turbine losses and the empirical loss model used will be discussed in section 3.4.4. The resulting pressure loss coefficient will be compared to the initial guess. When the difference exceeds the convergence criteria, the calculations will be rerun till convergence. The *Turbstator* output will be the stage thermodynamic values, velocity triangle results and geometrical properties. These values will be stored in the stg. data structure. The reader is referred to section 3.3.4 for a list of properties stg. includes.

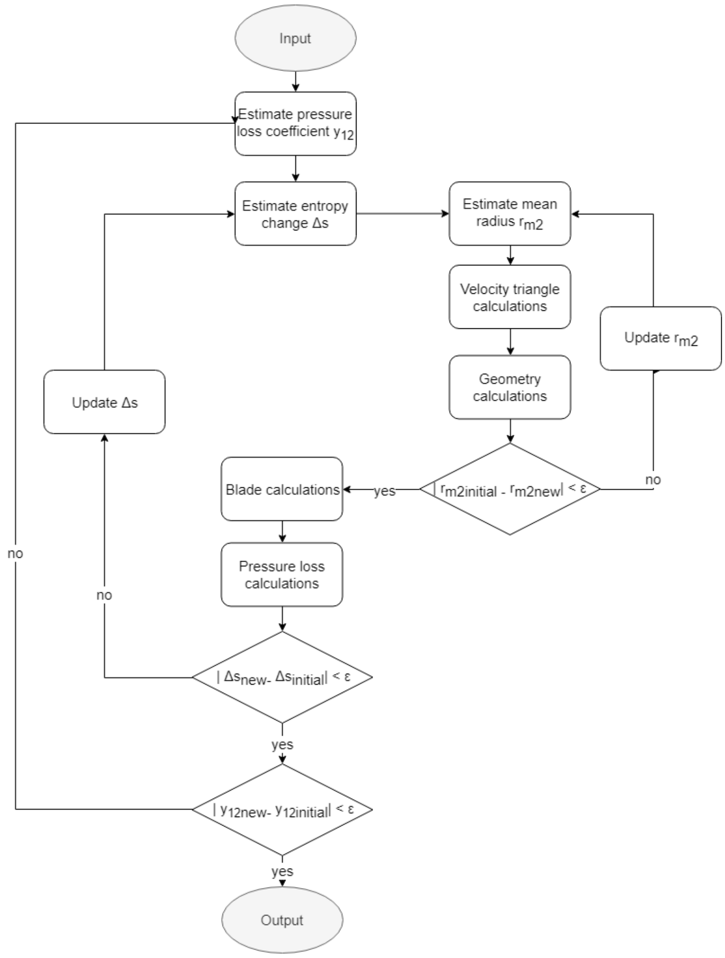

Figure 3.23: Flowchart of the function *Turbstator*.

Table 3.8: List of input parameters for *Turbstator*

Variable	Symbol	Units
Stage properties previous stage	stg.	[-]
Mass flow rate	$\dot{m}$	[kg/s]
Angular velocity	Ω	[rad/s]
Velocity station	vt	[-]
Geometry station	geom	[-]
Aero station	aero	[-]
Blade aspect ratio	AR	[-]
Blade taper ratio	λ	[-]
Thickness-to-chord ratio	t/c	[-]
Maximum camber location	a/c	[-]
Blade clearance gap	τ	[m]
Blade axial spacing	Fsp	[-]
Blockage factor	BLK	[-]
Axial velocity ratio	AVR	[-]
Turbine stator absolute exit flow angle	α_2	[deg]
Turbine stator absolute exit Mach number	M_2	[deg]
Blade trailing edge thickness	t_{TE}	[m]

Velocity triangle

The function *Turbstator* performs the velocity triangle calculations by Equations 3.88 - 3.92.

$$C2 = \sqrt{\frac{\kappa R T_{02}}{1 + (\kappa - 1)/2 M_2^2}} \cdot M_2 \tag{3.88}$$

$$C_{ax2} = C_2 cos(\alpha_2) \tag{3.89}$$

$$C_{th2} = C_{ax2} tan(\alpha_2) \tag{3.90}$$

$$\beta_2 = atan\left(\frac{W_{th2}}{C_{ax2}}\right) \tag{3.91}$$

$$W_2 = \sqrt{W_{th2}^2 + C_{ax2}^2} \tag{3.92}$$

For the stator the total enthalpy remains constant and the same holds for the total temperature. The static conditions do vary and can be found using equations 3.93 & 3.94.

$$h_2 = h_{02} - \frac{C_2^2}{2} \tag{3.93}$$

$$T_2 = T_{02} - \frac{C_2^2}{2Cp_{02}} \tag{3.94}$$

The total and static pressure at stator exit location are found using the isentropic flow equation as shown in Equations 3.95 & 3.96. In equation 3.95 the stator pressure loss coefficient, y_{12}, is used to take the stage losses into account.

$$p_{02} = p_{01}/(y_{12} \cdot (1 - \frac{1 + (\kappa - 1)}{M_2^2})^{-(\frac{\kappa}{\kappa - 1})} + 1) \tag{3.95}$$

$$p_2 = (1 + \frac{\kappa - 1}{2} M_2^2)^{-\frac{\kappa}{\kappa - 1}} \cdot p_{02} \tag{3.96}$$

The density at the stator outlet will follow from the ideal gas law. Finally, the area at the rotor outlet station can be found using equation 3.97. Please note that for the turbine, no blockage factor is used since the flow is an acceleration flow. The boundary layer growth will be less significant compared to decelerating flows in compressors [8].

$$A_2 = \frac{\dot{m}}{C_{ax2} \rho_2} \tag{3.97}$$

3.4.4. Turbine losses

The presence of irreversible entropy creation within the processes of the aero-engine will lead to a loss of available work. In order to get an accurate estimation of the turbine performance, the losses must be taken into account. The complex flow mechanics require the losses to be treated separately to estimate a more accurate pressure loss. In the literature, many different models exist to estimate the pressure losses.

Loss sources

The irreversibilities of the flow are caused by the flow behavior in the turbine. These causes can be categorized into different loss sources. The mechanism behind the loss sources will be explained in this section.

Profile loss

The profile losses are generated on the turbine blades surfaces due to the growth of the boundary layers. The displacement thickness will vary with flow features. However, on the suction side, the boundary layer is usually thicker compared to the pressure side. These flow phenomena will lead to entropy creation. Profile loss can be considered as a two-dimensional flow phenomenon and is usually far away from the inner and outer endwalls. Based on the Reynolds number, the boundary layer can be either turbulent or laminar, for turbulent boundary layers, the losses can be significantly higher. Turbine blade boundary layer losses account for over 50% of the two-dimensional losses in subsonic turbines[61].

Secondary loss

Secondary losses are partly generated when the annulus boundary layers pass through a blade row [61]. The main cause of secondary flows is transverse static pressure gradients and mass forces acting on the flow in the blade passage [62]. The losses associated with endwall secondary flows may account for almost 30-50% of the total blade loss in a turbine blade row [63]. Secondary flow is a complex flow mechanism, and research has shown that instead of endwall boundary layers being transformed into to passage vortexes along the endwalls of the cascade, the boundary layers split at the leading edge of the blade causing a horseshoe vortex to form over the turbine blade [63].

Tip clearance loss

For all turbo-machines, there is always a clearance gap between the rotating blades and the stationary casing. Tip leakage is defined as the passage flow from the pressure side to the suction side of the blade through the tip clearance. The tip clearance leads to a reduction in the mass flow rate through the blade passage and thus a reduction in the work done. The leakage flow leads to an increase caused by the viscous effects and the mixing as it passes through the leakage path. Tip leakage losses increase rapidly with the tip clearance gap size, typically a 1% increase of clearance gap to blade height will already incur a loss of 2-3% of efficiency [61].

Trailing edge loss

At the end of the blade, the flow from the pressure side and the suction side will intersect, and mixing will occur. The mixing process leads to an entropy generation and therefore losses. The trailing edge losses can account for up to 35% of the total 2D losses in subsonic turbines [61].

Shock loss

Shock waves start to occurs when the turbine blade passage is choked, and the exit Mach number is above 0.9. Shock waves are known to be irreversible and cause and entropy creation. In the shock wave, heat conduction and high viscous normal stresses cause entropy creation. Oblique shock waves produce less entropy creation compared to normal shock waves with the same upstream Mach number. The shock waves in the turbines are usually oblique shocks [61].

3.4.5. Pressure loss prediction

Tournier & El-Genk [53] have published work on axial flow turbines where the Kacker & Okapuu [64] model with the most recent refinements from Benner et al. [65] is discussed. This section elaborates on the work of Tournier & El-Genk.

Total loss coefficient

In the model, the turbine loss is given as a pressure loss coefficient. The pressure loss coefficient is defined as a fraction of the dynamic head of the blade row exit, equation 3.98 defines the pressure loss coefficient for the stator row. For the rotor, the equivalent loss coefficient would be defined by equation 3.99.

$$Y = \frac{\text{inlet total pressure - outlet total pressure}}{\text{outlet total pressure - outlet static pressure}} = \frac{P_{01} - P_{02}}{P_{02} - P_2} \tag{3.98}$$

$$Y = \frac{P_{02} - P_{03}}{P_{03} - P_3} \tag{3.99}$$

The model estimates this pressure loss coefficient by dealing with several loss sources as shown in equation 3.100.

$$Y = (Y_p + Y_s) + Y_{TE} + Y_{TC} \tag{3.100}$$

Profile loss & secondary Loss

Benner et al. proposed a pressure loss breakdown for the profile and secondary loss as shown in equation 3.101.

$$(Y_p + Y_s) \equiv (1 - Z_{TE}/H)Y_p' + Y_s' \tag{3.101}$$

The profile loss coefficient Y_p' is given by equation 3.102. The profile loss is multiplied by a factor 0.914 to account for a zero trailing edge thickness[64]. The profile loss coefficient $Y_{p,AM}'$ was originally developed for blades having a trailing edge thickness to pitch ratio of $t_{TE}/S = 0.02$, it also included the trailing edge losses [9].

$$Y_p' = 0.914\left[K_{in}Y_{p,AM}' + Y_{shock}\right]K_{re} \tag{3.102}$$

In the model, a factor K_{in} is used to take the cascade design improvements compared to the 50's into account. Kacker & Okapuu used the factor $K_{in} = 2/3$. It has been found that it underpredicts the profile losses for blade rows with axial inflow. Zhu & Sjolander [66] proposed a higher correction factor ($K_{in} = 0.825$ for IGV's. For rotor turbine blades, the original correction factor of 0.67 can still be used. Zhu & Sjolander have also introduced a Reynolds number correction factor, which is shown in equation 3.103.

$$K_{Re} = \left(\frac{2 \cdot 10^5}{Re_{2C}}\right)^{0.575} \quad \text{for} \quad Re_{2C} < 2 \cdot 10^5 \tag{3.103}$$

$$K_{Re} = 1.0 \quad \text{for} \quad Re_{2C} \geq 2 \cdot 10^5 \tag{3.104}$$

The factors K_p and Y_{shock} in equation 3.102 take gas compressibility into account, these relations are proposed by KO. The factor K_p gives a Mach number correction where 1 and 2 indicates the inlet and outlet of the rotor blades, K_p and can be calculated as shown in equations 3.105 - 3.108.

$$K_p = 1 = K_2(1 - K_1) \tag{3.105}$$

$$K_1 = 1 \quad \text{for} \quad Ma_2 < 0.2 \tag{3.106}$$

$$K_1 = 1 - 1.25(Ma_2 - 0.2) \quad \text{for} \quad Ma_2 > 0.2 \tag{3.107}$$

$$K_2 = \frac{Ma_1}{Ma_2}^2 \tag{3.108}$$

The factor for the shock losses Y_{shock} accounts for the shocks occurring at the hub of the leading edge, the losses due to these shocks occur from Mach number 0.4 at the hub. The factor Y_{shock} can be calculated as provided by Kacker [64]:

$$Y_{shock} = \frac{\rho_1 W_1^2}{\rho_2 W_2^2}\frac{r_{hub}}{r_{tip}}\frac{3}{4}(Ma_1^{hub} - 0.4)^{1.75} \quad \text{for} \quad Ma_1^{hub} > 0.4 \tag{3.109}$$

$$Y_{shock} = 0 \quad \text{for} \quad Ma_1^{hub} \leq 0.4 \tag{3.110}$$

Ainley & Mathieson have published a relation for the profile loss based on two sets of cascade data ($\beta_2 = 0$ and $\beta_2 = \beta_3$). The $Y'_{p,AM}$, which is an interpolation between the results of the two sets, is given by equation 3.111.

$$Y'_{p,AM} = \left[Y_{p,AM}^{\beta_2=0} + |\frac{\beta_2}{\beta_3}|(\frac{\beta_2}{\beta_3})(Y_{p,AM}^{\beta_2=\beta_3} - Y_{p,AM}^{\beta_2=0})\right] \cdot \left(\frac{t_{max}/C}{0.2}\right)^{K_m \beta_2/\beta_3} \tag{3.111}$$

The results from both ($\beta_2 = 0$ and $\beta_2 = \beta_3$) the turbine cascade tests from Ainley & Mathieson can be determined using figure 3.24.

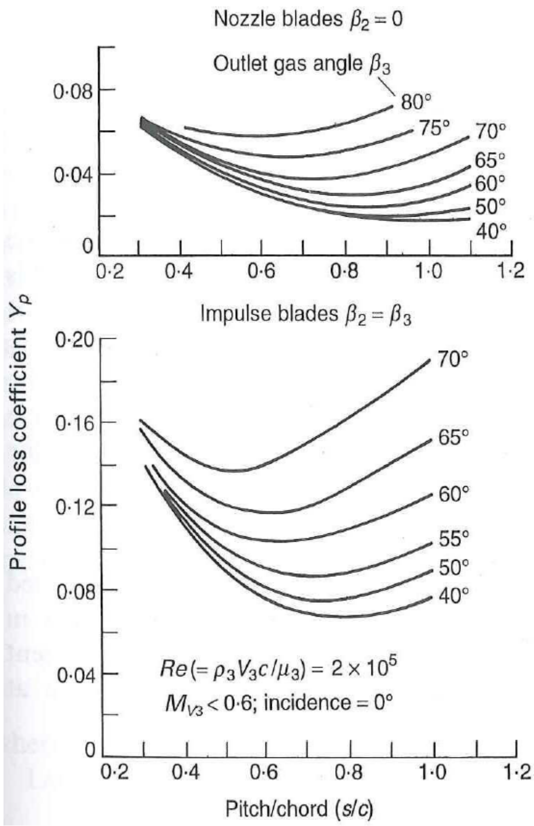

Figure 3.24: Profile loss coefficient as a function of s/c and the inlet and outlet angles. Source:[9]

The exponent K_m in equation 3.111 is given by Zhu & Sjolander [66] as:

$$K_m = 1 \quad \text{when} \quad t_{max/C} < 0.2 \tag{3.112}$$

$$K_m = -1 \quad \text{when} \quad t_{max/C} > 0.2 \tag{3.113}$$

The spanwise penetration depth, Z_{TE}, used in equation 3.101 of of the passage vortex separation line at the trailing edge is given by equation 3.114.

$$\frac{Z_{TE}}{H} = \frac{0.10|F_t|^{0.79}}{\sqrt{\cos\beta_1/\cos\beta_2} \cdot (H/C)^{0.55}} + 32.7\left(\frac{\delta^*}{H}\right)^2 \tag{3.114}$$

In equation 3.114 the tangential loading parameter F_t is given by:

$$F_t = 2\frac{S}{C \cdot \cos\gamma} \cdot \cos^2(\beta_m) \cdot [\tan(\beta_1) + \tan(\beta_2)] \tag{3.115}$$

The mean velocity angle β_m in the tangential loading parameter expression is given by :

$$\tan(\beta_m) = \frac{1}{2}|\tan(\beta_1) - \tan(\beta_2)| \tag{3.116}$$

The boundary layer displacement thickness at the inlet endwall δ^* used for equation 3.114 is given by:

$$\delta^* = \frac{0.0463x}{(\rho_1 W_1 x/\mu_1)^{0.2}} \tag{3.117}$$

The reference length x in equation 3.117 is taken as half the length of the axial blade chord. The secondary loss Y_s' in equation 3.101 can then be given by Benner et al.[65]:

$$Y_s' = F_{ar} \cdot \frac{0.038 + 0.41 \cdot \tanh(1.2\delta^*/H)}{\sqrt{\cos\gamma} \cdot (\cos(\beta_1)/\cos(\beta_2)) \cdot (C\cos(\beta_2)/C_x)^{0.55}} \tag{3.118}$$

The aspect ratio factor F_{ar} depends on the blade aspect ratio as:

$$F_{ar} = (C/H)^{0.55} \quad \text{when} \quad H/C < 2.0 \tag{3.119}$$

$$F_{ar} = 1.36604 \cdot (C/H) \quad \text{when} \quad H/C > 2.0 \tag{3.120}$$

Tip clearance loss

The tip clearance loss Y_{TC} will be modeled using the approach presented by Yaras & Sjolander [58]. The loss will be separated into two components, which are the blade tip and the blade gap, as shown in equation 3.121. The loss components of the tip clearance loss, tip loss & gap loss, are given in equation 3.122 and 3.123 respectively.

$$Y_{tc} = Y_{tip} + Y_{gap} \tag{3.121}$$

$$Y_{\text{tip}} = 1.4K_e\sigma\frac{\tau}{H}\frac{\cos^2\beta_2}{\cos^3\beta_m}C_L^{1.5} \tag{3.122}$$

$$Y_{\text{gap}} = 0.0049 K_g \sigma \frac{C}{H} \frac{\sqrt{C_L}}{\cos \beta_m} \tag{3.123}$$

The theoretical blade lift coefficient C_L is given by AM and is shown in equation 3.124.

$$C_L = \frac{2}{\sigma} cos(\beta_m)[\tan(\beta_1) + \tan(\beta_2)] \tag{3.124}$$

Yaras and Sjolander have provided values for K_E and K_G for different blade loading types.

Mid-loaded turbine blades: $K_E = 0.5$ and $K_G = 1.0$

Front- or aft-loaded turbine blades: $K_E = 0.566$ and $K_G = 0943$

The Y_{tip} given in equation 3.122 is only valid for unshrouded blades cascades. Dunham & Came [67] give an expression for shrouded blades. The relation for unshrouded blades can be used for shrouded blades by replacing the tip clearance with an effective clearance value given in equation 3.125 and reducing the losses by 21.3%. The expressions for Y_{tip} for shrouded cascade blades will be as described in equation 3.126.

$$\tau_{\text{eff}} = \tau/(n)^{0.42} \tag{3.125}$$

$$Y_{\text{tip}_{\text{shrouded}}} = \frac{0.37}{0.47} 1.4 K_e \sigma \frac{\tau_{eff}}{H} \frac{\cos^2 \beta_2}{\cos^3 \beta_m} C_L^{1.5} \tag{3.126}$$

Trailing edge loss

In the original AM model, the trailing edge loss was not treated separately but it was included in the profile loss and secondary loss by using a scaling factor. Kacker & Okapuu have presented a method to estimate the trailing edge kinetic energy loss coefficient $\Delta\phi_{TET}$ for axial entry nozzles (β_1=0) and impulse blades ($\beta_a = \phi_2$). Both types lead to a difference in thicknesses of the profile boundary layers at the trailing edge of the blades. In equations 3.127 & 3.128 give the $\Delta\phi_{TET}$ for axial entry nozzles and impulse blades respectively.

$$\Delta\phi_{TET}^{\beta_1'=0} = 0.59563 \left(\frac{t_{TE}}{O}\right)^2 + 0.12264 \left(\frac{t_{TE}}{O}\right) - 2.2796 \cdot 10^{-3} \tag{3.127}$$

$$\Delta\phi_{TET}^{\beta_1'=\alpha_2} = 0.31066 \left(\frac{t_{TE}}{O}\right)^2 + 0.065617 \left(\frac{t_{TE}}{O}\right) - 1.4318 \cdot 10^{-3} \tag{3.128}$$

For blades other than the two types described above the coefficient can be found using interpolation described in equation 3.129.

$$\Delta\phi = \Delta\phi_{TET}^{\beta_1'=0} + \left|\frac{\beta_1}{\phi_2}\right| \left(\frac{\beta_1'}{\phi_2}\right) [\Delta\phi_{TET}^{\beta_1'=\alpha_2} + \Delta\phi_{TET}^{\beta_1'=0}] \tag{3.129}$$

The kinetic energy loss coefficient $\Delta\phi_{TET}$ is converted to a pressure loss coefficient using the relation described in equation 3.130.

$$Y_{TE} = \frac{\left[1 - \frac{\gamma-1}{2} M_2^2 \left(\frac{1}{1-\Delta\phi_{TET}} - 1\right)\right]^{\frac{\gamma}{\gamma-1}} - 1}{1 - (1 + \frac{\gamma-1}{2} M_2^2)^{-\frac{\gamma}{\gamma-1}}} \tag{3.130}$$

3.5. Structural design & weight estimation

In the previous section, the aerodynamic and thermodynamic aspects of the engine design were discussed. This section will continue with the structural analysis of the engine components. Essentially all engine parts need to withstand the conditions and the structural loads. Based on the operating conditions and the structural loads, appropriate material selection can be made, and finally the component weight can be calculated.

3.5.1. Material selection

Material selection is a very important aspect of the design process since the material needs to meet at all the structural requirements while withstanding the harsh environmental conditions. The material of interest for aero-engines must have high strength-to-weight ratio and high thermal resistance. If the material can withstand high temperatures, the TIT can be increased allowing for higher thermal efficiency. Having a higher strength to weight ratio will require less material to be used and helps weight reduction. Materials that fit within the performance requirements of gas turbines are special steels, titanium alloys, and super-alloys.

Titanium is interesting for aerospace applications because of its high strength to weight ratio and corrosion resistance. Titanium alloy Ti-6Al-4V is mainly used engine parts, while pure titanium is used for the airframe[68]. Unfortunately, the maximum temperature limit for titanium alloys is only near 550^o and is therefore not usable in the higher temperature engine components. For those components, super-alloys are more suitable because of their thermal resistance. However, the density of the super-alloys is twice the value of the titanium alloys. The use of composite materials is slowly introduced in the newest engine to reduce weight drastically. The most commonly used materials for engine components are given in table 3.9. In figure 3.25, the material strength of common aero-engine material is plotted against temperature.

Table 3.9: Aeroengine material properties. Source:[4]

Material	Density [kg $/m^3$]	E [GPa]	$\sigma_u lt$ [MPa]	$\sigma_{0.2}$ [MPa]	ν[-]	Tmax [K]	$\alpha[K^{-1}]$
Ti-6Al-4V	4430	113.8	950	880	0.34	550	$9 \cdot 10^{-6}$
Inconel-718	8190	179	1100	980	0.32	980	$13 \cdot 10^{-6}$
Rene-41	8249	188	1400	1014	0.32	1255	$13.5 \cdot 10^{-6}$
Haynes 188	8980	205	243	131	-	1400	$18.5 \cdot 10^{-6}$

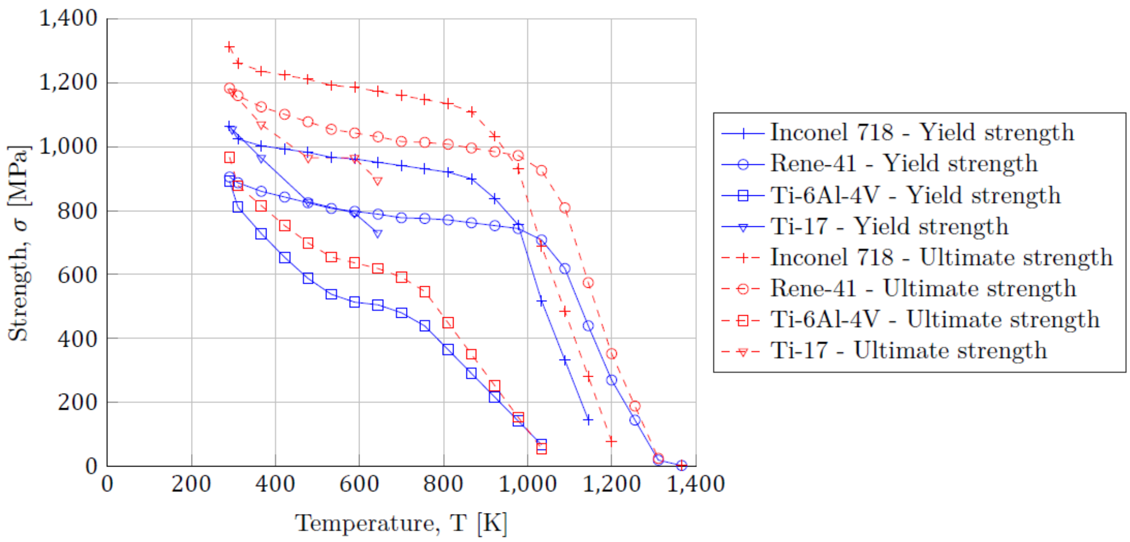

Figure 3.25: Temperature effect on yield and ultimate strength. Source:[1]

3.5.2. Blade

Turbine blades can be divided into two separate sections, the blade attachment section and the blade itself. A typical blade attachment is shown in figure 3.26. The blade attachment is comprised of a blade platform, a neck, and a fir tree. The neck only exists if the total height of the blade root is larger than the sum of the fir tree height and blade platform thickness[3]. The blade top section consists of the blade airfoil and tip shrouds.

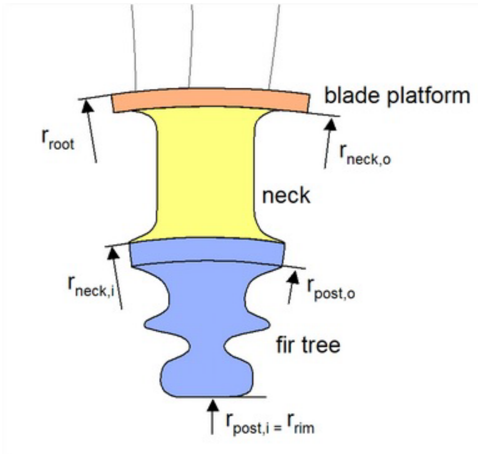

Figure 3.26: Blade segments. Source:[3]

In the documentation of Gasturb [3] the total weight is a summation of the blade components as given by equation 3.131.

$$m_{\text{blade}} = m_{\text{airfoil}} + m_{\text{shroud}} + m_{\text{platform}} + m_{\text{firtree}} + m_{\text{post}} + m_{\text{neck}} \tag{3.131}$$

The weight of the separate components can be calculated using equations 3.132 - 3.136.

$$m_{\text{shroud}} = \rho_b \cdot 0.05 t_{rim}^2 \frac{2\pi r_{b,tip}}{n_b} \tag{3.132}$$

$$m_{\text{platform}} = \rho_b \cdot 0.05 t_{rim}^2 \frac{2\pi r_{root}}{n_b} \tag{3.133}$$

$$m_{\text{firtree}} = \rho_b \cdot t_{rim} \cdot \pi \cdot \frac{r_{neck,i}^2 - r_{rim}^2}{2n_b} \tag{3.134}$$

$$m_{\text{post}} = \rho_b \cdot t_{rim} \cdot \pi \cdot \frac{r_{post,i}^2 - r_{rim}^2}{2n_b} \tag{3.135}$$

$$m_{\text{neck}} = \rho_b \cdot 2 \cdot t_b \cdot t_{rim} \cdot (r_{neck,0} - r_{neck,i}) \tag{3.136}$$

The airfoil blade mass will be approximated using the 2-D airfoil coordinates. These coordinates can be stacked to create a 3-D lofted surface. The enclosed volume by this object will be multiplied with the material density and a volumetric correction factor to calculate the airfoil blade mass. The volumetric correction factor will differ for the separate type of blades. For fan blades, it is assumed to be $V_F = 0.055$, based on the wide-chord hollow fan blade weight from the CFM56-7B validation engine [1] . The low and high-pressure compressor blade and the low-pressure turbine are assumed to be solid ($V_F = 1$), while the high-pressure turbine blades will use $V_F = 0.15$.

$$m_{\text{airfoil}} = \rho_b V_{\text{airfoil}} V_F \tag{3.137}$$

The centre of gravity of the whole blade components can be calculated with the weighted mean of c.g. as shown in equation 3.138.

$$r_{\text{cg,blade}} = \sum \frac{m_i r_{cg,i}}{m_{blade}} \tag{3.138}$$

It is assumed that the centrifugal forces of the blades are carried by the outer rim. The radial stress at the edge of the rim of the live disk is given by equation 3.139.

$$\sigma_{\text{r,rim}} = \frac{n_b m_b r_{cg,b}}{2\pi r_{rim} t_{rim}} \tag{3.139}$$

3.5.3. Disk

The primary function of the disk is to carry the loads from the rotor blades. Besides the loads from the disk, it also needs to bear the centrifugal loads from the disk weight. The weight of the disk can be significant because of all the high loads it has to sustain, and therefore the weight estimation is an important task.

In total, three different web designs are considered, the various options are shown in figure 3.27. Each design has slightly different load-bearing capabilities.

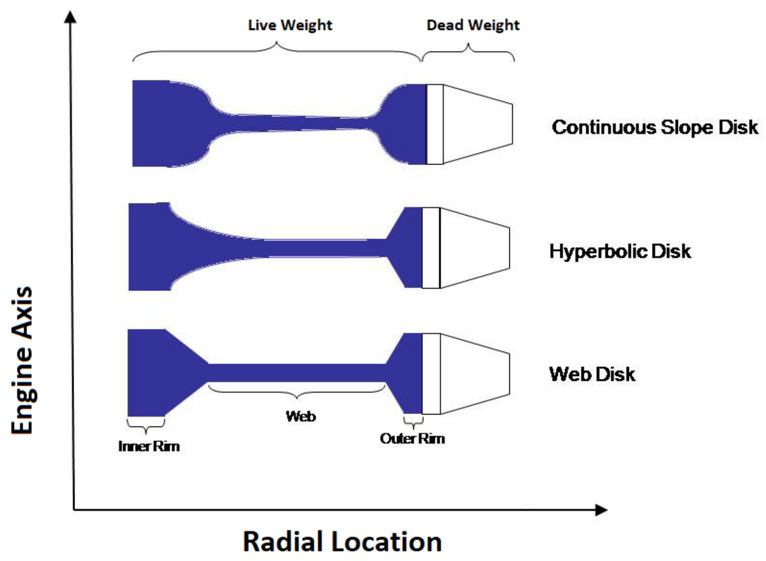

Figure 3.27: Common Disk Designs. Source:[10]

Disk stress calculation

The stress analysis of the turbine disk in literature under centrifugal load is commonly performed by considering an infinitesimal ring-shaped disk part of constant thickness as shown in figure 3.28 [69] [11].

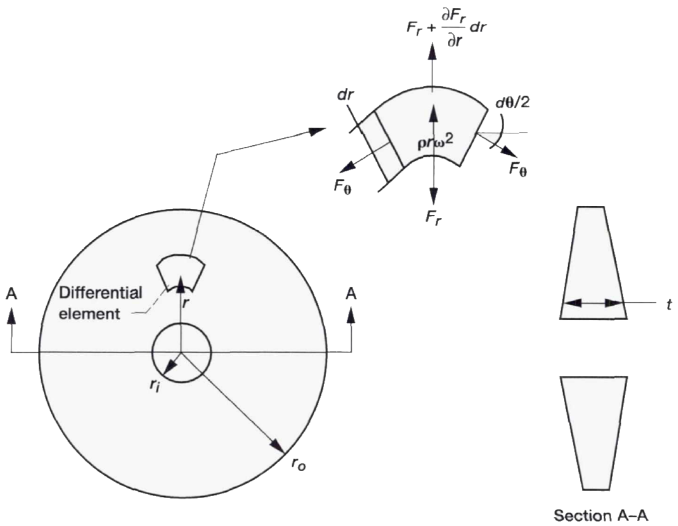

Figure 3.28: Rotating disk stress analysis. Source:[11]

Boormsa [4] and Tiemstra [1] have both discussed several methods for the disk stress analysis. In their work a total of four different methods were considered:

1. Method by Mattingly [6] based on hyperbolic disk design at constant stress levels throughout the disk.
2. A finite difference method by Tong et al.[11].
3. T-AXI Disk [10] method which is a low fidelity method for optimizing disk shapes.
4. Method presented in the work of Lolis[5].

All the different methods have been analyzed and compared, and it has been concluded that the method by T-AXI disk is most suited for the preliminary design stage. The main benefit is the low computational power needed. On the other hand, the T-AXI disk does have limitations as it does not take out-of-plane stresses into account. Both Boorsma [4] & Tiemstra [1] have considered all the pros and cons and have concluded the T-AXI method is the most suitable method. In this study, that choice will also be supported, and the T-AXI method will be the method to be used.

The governing equations of the T-AXI method have been described elaborately by Gutzwiller[70]. For the derivation and more elaborate explanation on the method, the reader is referred to Gutzwiller's publication. Gutzwiller has also provided the software *T-AXI Disk*, which is a disk design tool. This tool will be used for the verification of the implemented disk design methodology.

The method to calculate the disk stress starts by applying a force equilibrium on the infinitesimal ring-shaped disk part shown in figure 3.28 the tangential and radial forces are given by equations 3.140 and 3.141 respectively.

$$\sum F_\theta = 0 \tag{3.140}$$

$$\sum F_r = \sigma_r \cdot r \cdot r d\theta + \sigma_\theta \cdot d r d\theta - \left(\sigma_r + \frac{d\sigma_r}{dr} dr\right) \cdot (r + dr) d\theta - \rho \Omega^2 \cdot r^2 \cdot d r d\theta = 0 \tag{3.141}$$

Using algebraic manipulation on equation 3.141 it can be rewritten into:

$$\frac{d}{dr}(tr \cdot \sigma_r) - t \cdot \sigma_\theta + t \cdot \rho \cdot \Omega^2 \cdot r^2 \tag{3.142}$$

Equation 3.142 can be solved using Hooke's law which directly relates these stresses to the radial and tangential shear strains, but also thermal strains due to temperature differences in the disk. The definition for the hoop stress and radial stress are given in by equations 3.143 and 3.144 respectively.

$$\sigma_\theta = A\frac{du}{dr} + B\frac{u}{r} - A\alpha_r T - B\alpha_\theta T \tag{3.143}$$

$$\sigma_r = B\frac{du}{dr} + D\frac{u}{r} - B\alpha_r T - D\alpha_\theta T \tag{3.144}$$

The boundary conditions for the radial stresses at disk bore and rim is given by equation 3.146 and 3.146 respectively. At the bore of the disk, no force is applied therefore the stress at the disk bore will be zero. The radial stress on the trim of the disk is caused by the centrifugal load of the dead weight.

$$\sigma_{r,bore} = A\cdot\frac{du}{dr} + B\cdot\frac{u}{r} - A\cdot\alpha_r\cdot T - B\alpha_\theta\cdot T = -\frac{n_b m_b r_{cg,b}}{2\pi r t}\Omega^2 \tag{3.145}$$

$$\sigma_{r,rim} = B\cdot\frac{du}{dr} + D\cdot\frac{u}{r} - B\cdot\alpha_r\cdot T - D\alpha_\theta\cdot T = \frac{n_b m_b r_{cg,b}}{2\pi r t}\Omega^2 \tag{3.146}$$

The constants A, B, and D used in the stress calculations are a function of the material properties (i.e. Young's modulus E, Poisson's ratio ν) and relative relations are shown in equations 3.147 till 3.153.

$$A = \frac{C_{11}C_{33} - C_{13}^2}{C_{33}} \tag{3.147}$$

$$B = \frac{C_{12}C_{33} - C_{13}C_{23}}{C_{33}} \tag{3.148}$$

$$D = \frac{C_{22}C_{33} - C_{23}^2}{C_{33}} \tag{3.149}$$

$$C_{11} = C_{33} = \frac{E_r(E_\theta - E_r\nu_{\theta r}^2)}{E_\theta - 2E_r\nu_{\theta r}^2} \tag{3.150}$$

$$C_{22} = \frac{(E_\theta^2}{E_\theta - 2E_r\nu_{\theta r}^2} \tag{3.151}$$

$$C_{12} = C_{23} = \frac{E_r E_\theta \nu_{\theta r}}{E_\theta - 2E_r\nu_{\theta r}^2} \tag{3.152}$$

$$C_{13} = \frac{E_r^2\nu_{\theta r}^2}{E_\theta - 2E_r\nu_{\theta r}^2} \tag{3.153}$$

Feasibility check

The feasibility of the disk design will be checked based on three different parameters.

Burst Margin According to Tong [11], the average tangential stress $\sigma_{\theta,avg}$ should be at 47% lower than the ultimate yield strength σ_y of the material used at average disk temperature. The burst margin is calculated, as shown in equation 3.154.

$$\mathrm{BM} = \left(\frac{0.47\sigma_{ult}}{\sigma_{\theta,avg}} - 1\right)\cdot 100 \tag{3.154}$$

Design Margin The second feasibility check is using a design margin that compares the maximum allowable Von Mises stress, σ_{VM}, the yield stress of the material, σ_y. A safety factor is used in the calculation of the design, which results in equation 3.155.

$$\text{DM} = \left(\frac{0.9\sigma_y}{\sigma_{VM}} - 1\right) \cdot 100 \tag{3.155}$$

Burst Speed The burst speed takes into account the possibility of the disk being used in over-speed conditions. Under these conditions, the disk is turning higher than the design rotational speed limit. This can happen during the design missions for a short period of time. Gasturb proposes a disk to be tested for the feasibility of 130% of the design rotational speed. Equation 3.156 shows the burst speed formula.

$$BS = 100 \cdot \sqrt{\frac{\sigma_{ult}}{\sigma_{\theta,avg}}} \tag{3.156}$$

Flowchart disk design

The flowchart for the disk design is shown in Figure 3.29. The disk designs geometry can be described by geometrical variables, each disk design can be described by a different set of variables. These geometrical variables will be changed by the optimizer to find the optimum disk design. The disk will first be split into 100 stations along the radial span of the disk. At every station, the disk temperature and the material properties will be calculated. Finally, the T-AXI method will be used to calculate the disk stresses, these will be compared to the material properties. Finding a feasible disk design with the lowest disk mass will be done in two steps to save computational time. In the first step, a genetic algorithm is used to find a feasible solution. In the following step, the fmincon optimizer is used to search for a design solution with lower disk weight.

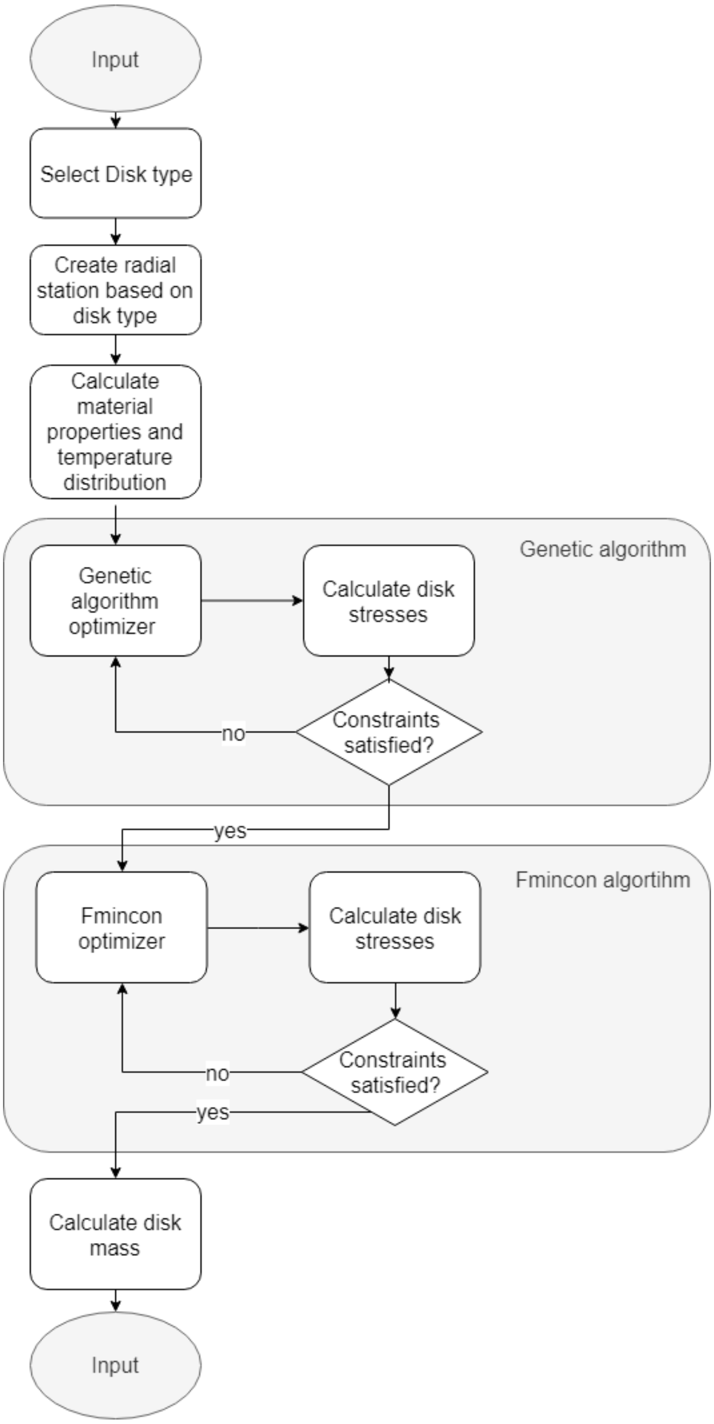

Figure 3.29: Flowchart of disk design code.

3.5.4. Casing

The casing of the LPT will contain the pressure of the turbine. Based on practice, the casing is usually made from a single piece with a constant thickness. The static load the casing has to bear is created by the pressure difference between the inner and outer casing walls. The Barlow's formula is shown in equation 3.157.

$$P_{st} = \frac{2\sigma_y t}{D} \tag{3.157}$$

The equation can be rewritten to calculate the minimum thickness of the casing to sustain the pressure load according to Barlow's formula. Equation 3.158 calculates the minimum thickness required.

$$t_{casing} = \frac{P_{st} r}{\sigma_y - P_{st}} \tag{3.158}$$

Where r is the casing radius and P_{st} is the pressure difference between the inner and outer casing walls. The mass of the casing can be found using equation 3.159.

$$m_{\text{casing}} = 2\pi \cdot r_t \cdot l_{\text{stage}} \cdot t_{\text{casing}} \cdot \rho_{\text{casing}} \tag{3.159}$$

3.5.5. Shaft

The shaft of an aero-engine is mainly used to transfer power or torque between rotating members. In this process, the shaft is subject to torsion, bending, and axial loading. Not only structural requirements need to be fulfilled, but also the power transmission requirements need to be considered too [71]. For the conceptual design, bending and vibrations are neglected because of the complexity introduced by these structural loads. The conceptual design will only be based on transmitted torque. This approach is supported by other preliminary weight estimation methodologies[41] [5]. Several assumptions [5] will be used to simplify the design process of the shaft design. The shafts will be assumed to have a constant thickness. The inner shaft will be a solid shaft with a zero inner diameter. The length of the shaft will be taken equal to the length of the components the shaft connects. The outer diameter of the shaft is selected in order to satisfy the torque load, which is given by equation 3.160.

$$\sigma_{\text{max}_{\text{shaft}}} = \frac{16\dot{W} \cdot D_{\text{out}_{\text{shaft}}}}{\omega \cdot \pi \cdot (D^4_{\text{out}_{\text{shaft}}} - D^4_{\text{in}_{\text{shaft}}})} \tag{3.160}$$

The calculated maximum stress is checked against the material yield stress. Combining the material density and the shaft dimensions the total shaft weight can be calculated.

$$W_{\text{shaft}} = \rho_{\text{shaft}} \cdot \frac{1}{4} \cdot \pi \cdot (D_{\text{out}_{\text{shaft}}} - D_{\text{in}_{\text{shaft}}})^2 \cdot L_{\text{shaft}} \tag{3.161}$$

3.5.6. Frames

The frames are defined as the support structures that carry the loads to the external fixings. They usually include cylindrical or conical shaped bearing housings, but also support struts and mounting lugs. The frame weight is quite significant for aero engines, but available methods in the literature are limited. According to Lolis [5], this can be attributed to their sizing complexity and customized design for one engine or engine family. As a result, frame weight estimation methods are commonly based on empirical correlations. The methods used for the frame weight in this thesis project will be the method described by Onat and Klees[41]. In this method, four different frame types are considered; a single bearing frame with or without power off-take, a turbine frame, and an intermediate 2 bearing frame/ burner frame. The weight of these frames is estimated using the empirical relations shown in figure 3.30, where the frame weight is correlated with the frame diameter.

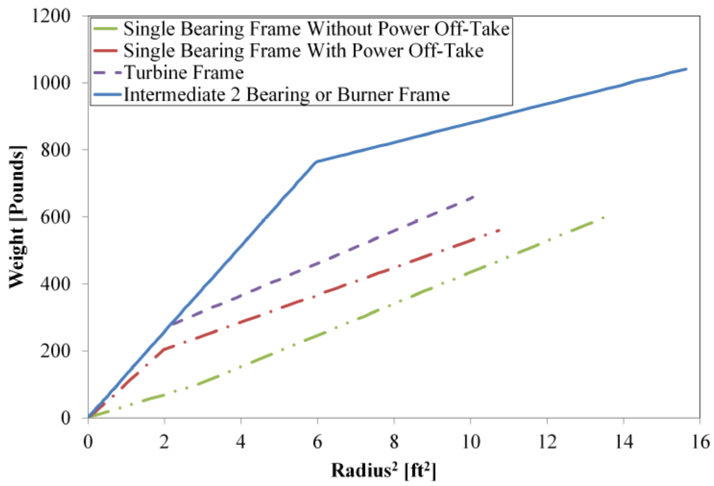

Figure 3.30: Frame weight estimation. Source:[5]

3.5.7. Control and accessories

The category control and accessories includes a collection of smaller components consisting of the weight of the fuel, oil, control, and starting systems and the accessory gearbox. The weight of these individual components is small and difficult to estimate. Based on Onat & Tolle [72], a percentage of the total engine weight is used as an estimation for the control and accessories weight. The accuracy of this method is relatively low because it does not take into account engine type or level of technology. The control and accessories weight will be estimated using equation 3.162.

$$W_{\text{Control and accessories}} = 0.1 \cdot W_{\text{Total engine}} \tag{3.162}$$

3.5.8. Nacelle

The loads the nacelle needs to bear can be divided into engine loads and flight loads. The engine loads include the engine pressure loads, thermal loads, thrust loads, and centrifugal loads. The flight loads include the aerodynamic pressure and inertial forces [73]. In the context of conceptual design, the flight loads and some of the engine loads will not be considered. For the conceptual design, the pressure loads and the thrust loads only will be considered.

The nacelle can be considered as a pressure vessel. The internal pressure is equal to the engine pressure, while the external pressure is equal to the ambient pressure. In the journal article by Ibrahim, Ryu & Saidpour[74], the stress analysis of thin-walled pressure vessels is explained. The following assumptions will be made to simplify the analysis:

- The wall radius will be at least ten times larger than the wall thickness.
- The weight of the fluid is considered negligible.
- Stress distributions do not vary throughout the wall thickness.
- The material is assumed to be linear-elastic, isotropic and homogeneous.

The circumferential and longitudinal stress can be calculated with equations 3.163 & 3.164 respectively.

$$\sigma_{\text{circumferential}} = \frac{(p_{\text{in}} - p_{\text{ex}})r}{t} \tag{3.163}$$

$$\sigma_{\text{longitudinal}} = \frac{(p_{\text{in}} - p_{\text{ex}})r}{2t} \tag{3.164}$$

3.6. Turbofan code overview

The compressor and turbine components design has been elaborated upon in the previous sections, followed by the structural design and weight estimation methodology. For the performance and weight estimation of a turbofan engine, the separate functions of the components need to be coupled in an overall turbofan code. The flowchart for the turbofan design tool is shown in figure 3.31. The low-pressure and high-pressure compressor use the same identical compressor design function. The same also holds for the low-pressure and high-pressure turbine, which share the turbine design function. It has to be noted that only the separate engine components in figure 3.31 are optimized individually. For example, the effect of the compressor design variables on the turbine efficiency is not taken into account for the turbine optimization. As a result, the turbofan design will only be sub-optimal. This could be solved by implementing an optimizer in the overall turbofan code level instead of the components function level, but this would increase the calculation time significantly.

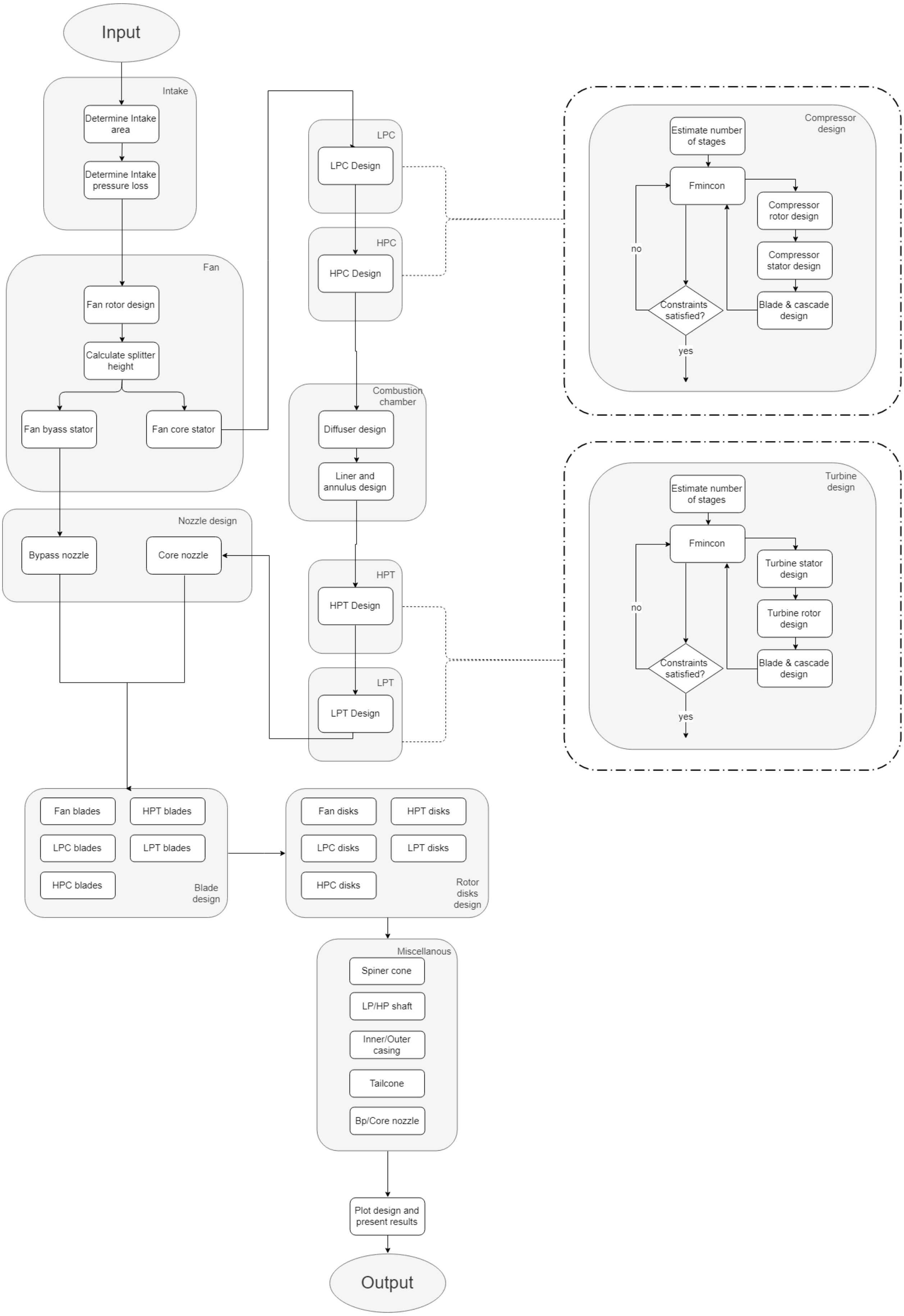

Figure 3.31: Flowchart of the turbofan design code.

4
Validation

4.1. Validation cases

The conceptual turbofan design tool will be validated using two existing turbofan engines. These two engines include the CFM56-7B27 and the PW4056, both are two-spool unmixed turbofan engines. These two engines have different performance characteristics and geometry. Modeling both the CFM56-7B and the PW4056 will demonstrate the capabilities of the conceptual turbofan design tool to model variously sized and thrust-rated turbofan engines. The main challenge of validating the tool is the limited engine data available from the engine manufacturers. As a result, missing data is complemented using data literature or estimated based on comparable engines. The performance characteristics of both engines are shown in table 4.1.

Table 4.1: CFM56-7B and PW4056 engine performance data. [15]

	CFM56-7B27	PW4056	Unit
Take-off thrust	121	222	[kN]
Mass flow rate	355	762	[kg/s]
Bypass ratio	5.10	4.80	[-]
Turbine inlet temperature	1300	1250	[K]
Overall pressure ratio	32.7	30.2	[-]
Cruise TSFC	16.06	17.66	[mg/N s]
Engine mass	2431	4173	[kg]
Fan diameter	1.549	2.46	[m]
HP spool rotational speed	14460	10400	[RPM]
LP spool rotational speed	4860	4000	[RPM]

4.2. CFM56-7B validaiton case

The CFM56 is considered to be the most successful commercial aircraft engine of all time with more than 30,000 units delivered to date. The specific engine model CFM56-7B is an exclusive design for the Boeing 737 aircraft.

Most of the geometrical inputs for the conceptual turbofan tool were extracted from the CFM 2D cutaway (figure 4.1), other input variables were obtained from engine certification and literature[15][5].

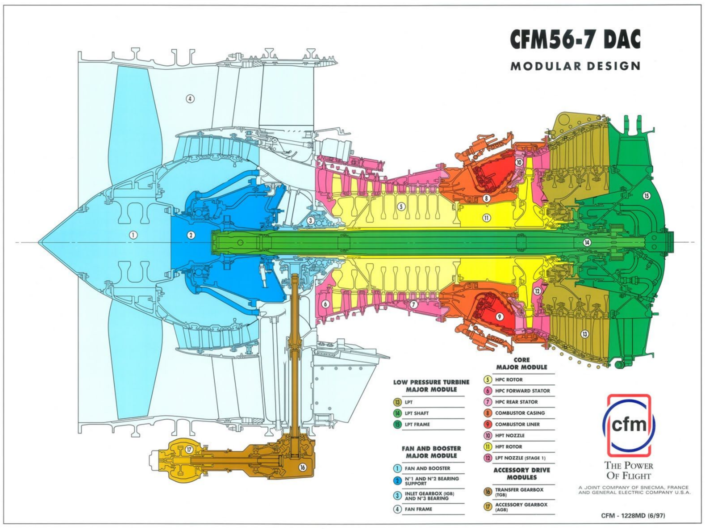

Figure 4.1: CFM56-7 2D cutaway. Source: CFM international [5]

4.2.1. Engine layout

The engine layout of the CFM56-7B estimated by the conceptual turbofan tool is shown in figure 4.2, additionally in figure 4.3 the estimated design is overlaid on the original design 2D cutaway. The existing design is well modeled using the conceptual turbofan tool. The general annulus shape and the number of stages for the compressor and turbine components have been estimated closely. The exact annulus shape could not be matched exactly because the falling mean line used in the original design is currently not an option in the tool. The rotor disks do show some discrepancies. Especially the turbine disks, these are estimated larger than the actual CFM56-7B turbine rotor disks. The larger disks are the result of larger rotating mass since the rotational speed and radial position of the blades are similar in both cases. Given the same annulus design, the larger rotating mass is caused by either a different material use, a different volume fraction of the rotor blades, or a different number of rotor blades used.

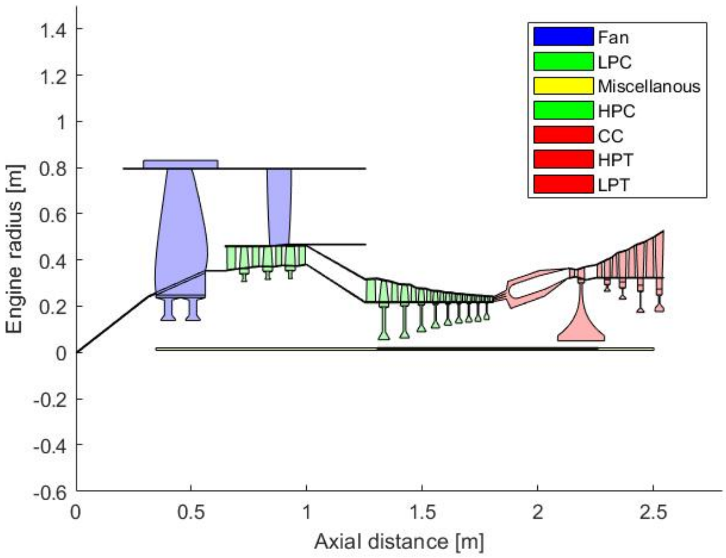

Figure 4.2: Estimated CFM56-7B 2D annulus design.

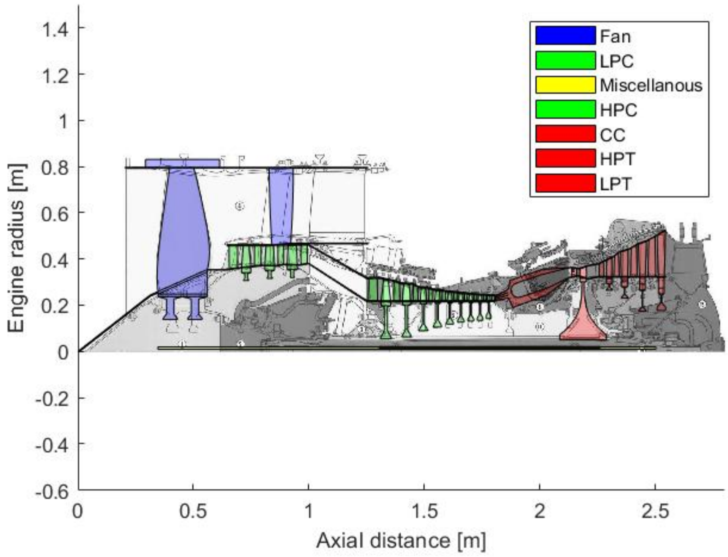

Figure 4.3: Estimated CFM56-7B 2D annulus design overlaid on original CFM-7B 2D cutaway.

4.2.2. Weight estimation

As a result of the very closely matched annulus design, the weight of the engine has also been estimated with high accuracy. In table 4.2 it can be seen that the estimated weight is 9.6% off compared to the real weight. Having a lower estimate is not uncommon. In the estimation, smaller components have not been taken into account because of their insignificant weight. In the current Matlab model, no turbine cooling has been taken into account. This also leads to a lower weight estimation compared to the original CFM56-7B engine.

Table 4.2: CFM56-7B weight estimation results

	Original[kg]	Estimated[kg]	Difference [kg]/[%]
Engine weight	2431	2198	-234(-9.6%)

The lack of OEM component weight data will lead to the use of CFM56-7B simulation results from Lolis [5] for the weight comparison of the individual engine components. Table 4.3 compares the components weight breakdown of the CFM56-7B by Lolis with the results estimated in this study. Lolis has mentioned in her work that the disk rim thickness is only a function of the blade chord, while it should also be a function of the diameter and rotational speed. This has resulted in unrealistic rim stresses and wrong disk shapes. In this study the centrifugal load is used to size the disk, as a result, the disks are overall smaller. The LPC and LPT weight differences can be explained by the difference in disk weight. The difference in HPT design is a combination of the wrong disk stresses by Lolis and the use of a different disk shape. Lolis only implemented web disk shapes while in the tool, a hyperbolic disk shape is used for the HPT disk. Contrary to the lighter components, the estimated fan is heavier compared to Lolis. The main difference in fan design is the use of two rotor disks for the fan rotor blade. In figure 4.1 it can be seen the CFM56-7B has two fan rotor disks instead of a single rotor disk used by Lolis. The fan geometry and size do not match perfectly with Lolis, but do match the original fan design, as shown in figure 4.3.

Table 4.3: CFM56-7B Engine weight breakdown comparison.

	Lolis [kg]	Estimated[kg]	Difference [kg]
Fan	704	755	54
LPC	171	112	-60
HPC	224	145	-79
CC	55	97	42
HPT	105	125	20
LPT	258	210	-48
Ducts	21	17	-4
Shaft	55	20	-35
Frames	462	505	44
Controls	229	212	-17
Total	2283	2198	-86

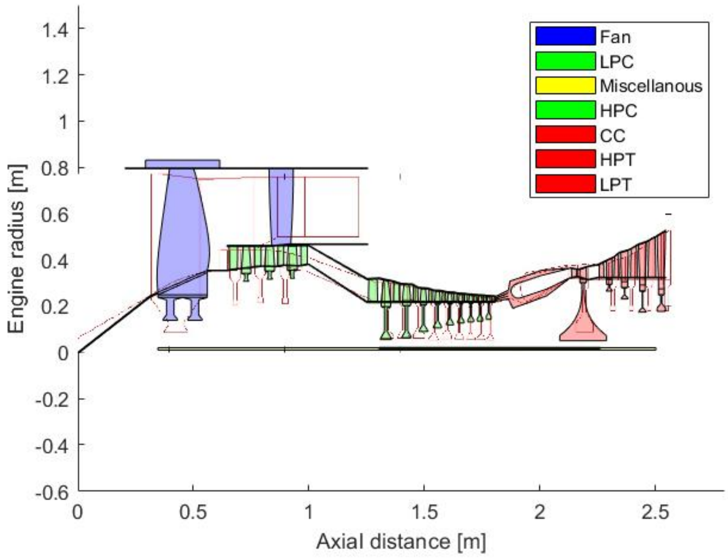

Figure 4.4: Estimated CFM56-7B 2D annulus design overlaid on Lolis' result.

4.2.3. Engine performance

The CFM56-7B engine has been calculated at the top of climb design conditions, the main results can be found in table 4.4. The accuracy of the validation data cannot be ensured. Only the engine weight and fan diameter are obtained from certification data. The remainder of the data is obtained from the literature. The cruise TSFC shows a small difference of 3.1%. Unfortunately, many parameters can impact the TSFC. Most of these parameter values did not come from OEM data. Therefore the accuracy of the TSFC estimate is not high. However, it is good that even with all the uncertainties the TSFC is still close to the actual value.

Table 4.4: CFM56-7B estimated and original engine performance data.

	Matlab CFM56-7B	Original CFM56-7B	Unit
Cruise thrust	24	24	[kN]
Cruise TSFC	16.46	16.06	[mg/N s]
Engine mass	2198	2405	[kg]
Fan diameter	1.587	1.549	[m]
$\eta_{\text{propulsive}}$	0.741	-	[-]
η_{thermal}	0.467	-	[-]
η_{overall}	0.346	-	[-]

4.3. PW4056 validaiton case

The second engine used for the validation is the Pratt & Whitney PW4056 engine. This engine is rated at a take-off thrust of 276 kN, compared to the CFM56-7B, it is a much larger and more powerful engine. Both publicly available data and the PW4056 Gasturb model provided by A. Gangoli Rao from the FPP department of TU delft has been used for the validation. The schematic drawing of the Pratt & Whitney PW4000 is shown in figure 4.5. The PW4000 is a turbofan engine family from Pratt & Whitney. The PW4056 is a variant of the PW4000. In the absence of an available 2D cutaway drawing of the PW4056, the 2D cutaway of the PW4000 will be used.

4.3.1. Engine layout

Similar to the CFM56-7B validation, most of the input parameters of the conceptual turbofan design tool could be obtained from either the engine certification files, the schematic drawing, or just general assumptions based on literature. However, in this case, the Gasturb PW4056 model could also be examined to obtain input variables. The geometry output of the PW4056 calculated by the turbofan tool is shown in figure 4.6. In figure 4.7 & 4.8 the result is overlaid on the PW4000 2D cutaway and Gasturb PW4056 Model respectively.

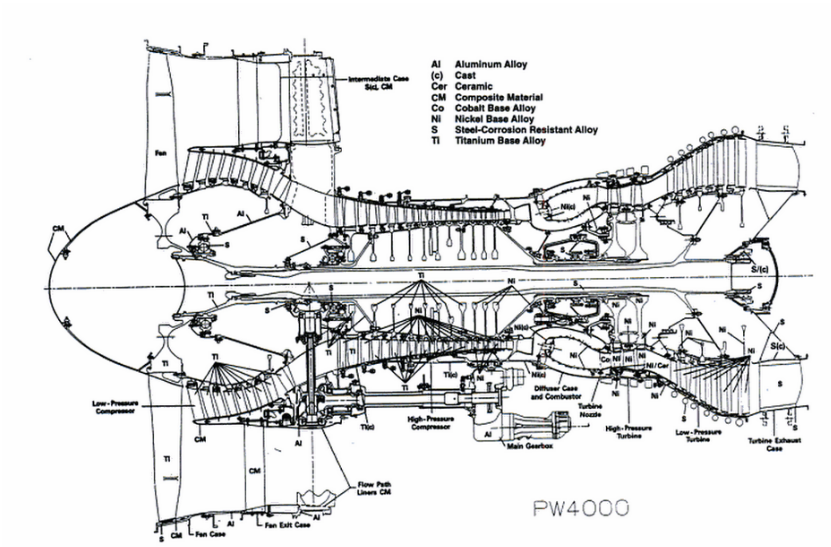

Figure 4.5: PW4000 2D cutaway.

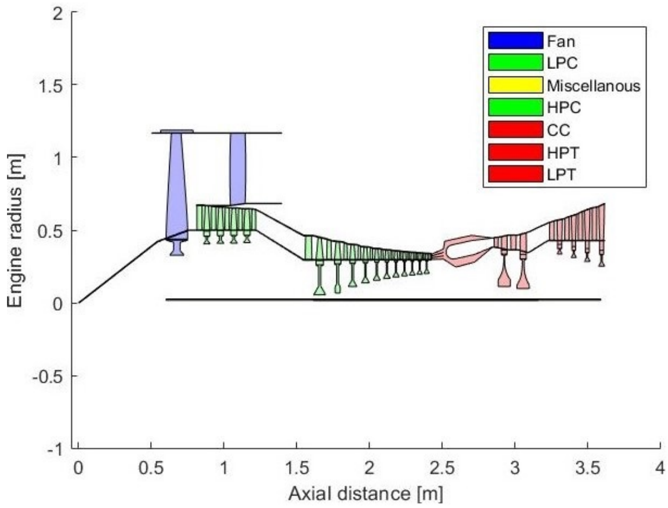

Figure 4.6: Estimated PW4056 2D annulus design.

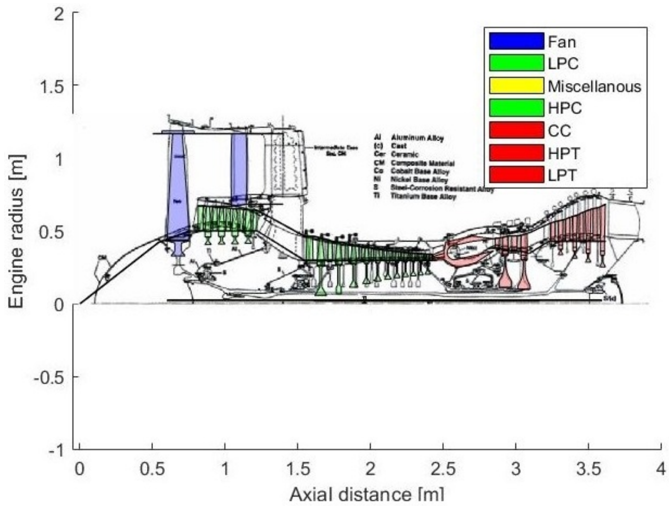

Figure 4.7: Estimated PW4056 2D annulus design overlaid on original PW4000 2D cutaway.

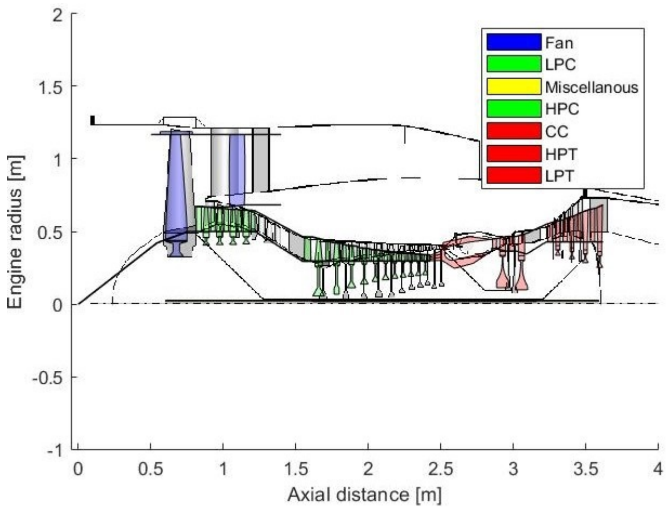

Figure 4.8: Estimated PW4056 2D annulus design overlaid on Gasturb 2D cutaway.

Overall the estimated engine layout matches very closely with the PW4000 2D cutaway. Small differences between the annulus shape and rotor disk design of both designs can be observed. In the conceptual turbofan tool, three different annulus shapes can be chosen, either fixed hub, mean, or tip radius is possible. In the real case, the annulus design can have any shape. This made it hard to exactly match the annulus mean line of the LPC and HPC. The HPC rotor disks show a decreasing disk height in the estimated engine layout while in PW4000, the HPC rotor disks have the same height. The rotor stages decrease in size, and so does the rotating mass. Therefore a smaller rotor disk for the later HPC stages is expected. In the PW4000 case, the rotor disk length is most likely constrained to a fixed length, while in the conceptual turbofan engine estimate, it is not. The turbine part of the estimate matches very closely with the schematic drawing. Both the annulus size and the disk size show minimal differences.

The Matlab estimate does show some differences geometrically compared to the Gasturb estimate. The fan blades estimated by Gasturb are larger because the aspect ratio of the fan rotor blade is different. In the Matlab estimate, an aspect ratio of 3.8 is used while the Gasturb model uses 2.2. As a result of the larger fan blade, the fan disk is also larger in the Gasturb estimate. The HPC in the Gasturb estimate uses a fixed tip radius while the Matlab estimate utilizes a fixed hub radius. This leads to a slight mismatch in HPC geometry, where the average mean radius of the Gasturb HPC design is larger. As a result, the HPC rotor disks of the Gasturb estimate are larger because of the higher disk structural load. The turbine design of both estimates also shows differences when compared, both the HPT and LPT estimated by Gasturb are smaller in size. The size of the HPT disks estimated by Gasturb seems to be unrealistic small when compared to the PW4000 schematic drawing.

4.3.2. Weight estimation

The weight estimation of the PW4056 from the Matlab tool is compared to the PW4000 weight found in the literature. The estimated value is 8.7% lower compared to the literature results, as can be seen in table 4.5. The engine weight of the specific PW4056 is not available. The literature publication [15] for the PW4000 has been used for weight validation. One has to take into account the PW4056 is not exactly the same engine as the PW4000. Also, it must be considered that the Matlab model does not take cooling flows into account, which results in lower engine weight.

Table 4.5: PW4056 weight estimation results

	PW4000 (literature) [kg]	Matlab estimate [kg]	Difference [kg]/[%]
Engine weight	4173	3820	-364(-8.7%)

The benefit of the Gasturb model is that it also estimates the weight of the engine components. Therefore, it can be used to validate the component weight estimation of the conceptual turbofan tool. The downside of the Gasturb weight estimation model is that it depends more on input variables. The weight breakdown of the estimated Matlab model and the Gasturb estimated model are shown in table 4.6.

The components do show some differences; the fan, HPC, and LPT estimated by Gasturb are heavier compared to the Matlab estimate. Both are mainly caused by differences in the blade aspect ratio. Gasturb uses a fixed aspect ratio of 3.2 for the LPT blades, while the Matlab tool uses an aspect ratio of 3.50 for the first stage, which progressively increases to 6.25 for the last stage. The weight differences of the HPT is mainly caused by the cooling effects. The average temperature of the rotor disk is much lower in the Gasturb estimate compared to the Matlab estimate. Material properties are affected by temperature. Material yield strength decreases for higher temperatures. Without cooling, larger rotor disks are required for the HPT. From figure 4.8, it can be seen that the Gasturb modeled HPT disks are significantly smaller compared to the Matlab estimate.

Table 4.6: PW4056 Engine weight breakdown comparison.

	Gasturb [kg]	Matlab estimate [kg]	Difference [kg]
Fan	1093	979	-114
LPC	331	382	51
HPC	592	506	-87
CC	152	151	-2
HPT	156	228	72
LPT	346	280	-66
Ducts	165	42	-123
Shaft	96	47	-50
Frames	506	834	327
Controls	371	373	3
Total	3809	3820	11

4.3.3. Engine performance

The engine performance of Matlab estimate is compared to the Gasturb PW4056 estimate. The thrust difference is significant between the two estimates. The main reason causing this is the use of cooling. In the Gasturb estimation, cooling flows are considered while in Matlab no cooling flows are modeled. For the cooling flow, part of the working fluid at the end of the HPC stages will be extracted to cool the material in the hot sections. This leads to less working fluid combusted and used for useful work extraction. A Gasturb estimate without cooling flows is also included to show the effect of not taking cooling flows into account. The performance of the Gasturb estimates and the Matlab estimate are shown in table 4.7.

When comparing the Matlab results with the Gasturb with cooling results, mainly the thrust value shows a large discrepancy. The other values are much closer, the difference in TSFC and η_{overall} is very small. The results from the Gasturb estimation without cooling are as expected even closer to the Matlab estimation. On the other hand, the weight estimation by Gasturb for the case without cooling is significantly lighter, because of the lack of a cooling system.

Table 4.7: PW4056 estimated performance data at top of climb condition.

	Matlab PW4056	Gasturb PW4056	Gasturb PW4056 (no cooling)	Unit
Cruise thrust	46.03	39.43	45.63	[kN]
Cruise TSFC	17.40	17.66	17.14	[mg/N s]
Engine mass	3820	3809	3673	[kg]
Fan diameter	2.33	2.52	2.52	[m]
$\eta_{\text{propulsive}}$	0.761	0.783	0.758	[-]
η_{thermal}	0.430	0.411	0.438	[-]
η_{overall}	0.327	0.322	0.332	[-]

5

Results and Discussion

The purpose of the conceptual turbofan design and sizing tool is to (quickly) estimate engine performance and characteristics. The conceptual turbofan engine tool will vary four key design parameters (BPR, OPR, FPR, and TIT) over a realistic range to assess their impact on engine characteristics. The analysis will focus on how future engines can improve propulsive efficiency (section 5.1) and thermal efficiency (section 5.2) to reach the ambitious goals set by ACARE. Previously in section 2.4.2, it has already been shortly discussed how the efficiency can be improved in an isentropic process. In this analysis, losses are also taken into account to achieve more accurate and realistic results. Besides the thermodynamics, also weight estimation is considered in the analysis.

Every case is also calculated using Gasturb for comparison with the Matlab conceptual turbofan tool. The weight estimation capabilities of Gasturb are highly dependent on input variables. It has been decided not to include weight estimation results from Gasturb and only the thermodynamic results. For all results related to weight estimation, only the Matlab result are shown.

The CFM56-7B engine from the validation case is used as the baseline engine in the analysis. All cases are run in cruise flight conditions (altitude 10668m and Mach 0.82). In the sensitivity analysis, the parameters of interest (BPR, OPR, FPR, and TIT) are varied while the other parameters remain unchanged at the value shown in table 5.1. In table 5.2, 5.3 and 5.4 the design input parameters are shown for the fan, compressors and turbines respectively.

Table 5.1: Baseline engine performance values.

Parameter	Value	Unit
Altitude	10668	[m]
Mach number	0.82	[-]
Intake mass flow rate	355	[kg/s]
Thrust	24.0	[kN]
Overall pressure ratio	32.7	[-]
Turbine inlet temperature	1300	[K]
Bypass ratio	5.10	[-]
Nozzle type	Unmixed	
High speed spool rotational speed	14460	[RPM]
Low speed spool rotational speed	4860	[RPM]

Table 5.2: Baseline fan design input parameters

Parameter	Value	Unit
Inlet Mach number	0.50	[-]
Fan design pressure ratio	1.65	[-]
Hub-to-tip ratio (inlet/outlet)	0.326 / 0.456	[m]
Rotor aspect ratio	2.347	[-]
Stator aspect ratio	2.90	[-]
Rotor Blade solidity (inlet/outlet)	2.629 / 1.213	[-]
Stator Blade solidity (inlet/outlet)	2.596 / 1.842	[-]
Rotor blade material	AM350	
Stator blade material	AM350	
Fan rotor disk material	AM350	

Table 5.3: Baseline compressor design input parameters

Parameter	LPC Value	HPC value	Unit
Maximum loading coefficient	0.50	0.50	[-]
Compressor design pressure ratio	1.75	12.18	[-]
Configuration	constant tip	constant hub	
Inlet rotor Aspect Ratio	2.50	2.25	[-]
Outlet rotor Aspect Ratio	2.00	1.25	[-]
Inlet stator Aspect Ratio	2.25	1.75	[-]
Outlet stator Aspect Ratio	1.75	1.50	[-]
Rotor blade material	AM350	AM350/INCONEL718	
Stator blade material	AM350	AM350/INCONEL718	
Rotor disk material	AM350	AM350/INCONEL718	

Table 5.4: Baseline turbine design input parameters

Parameter	HPT Value	LPT value	Unit
Maximum loading coefficient	2.50	2.50	[-]
Configuration	constant mean	constant hub	
Inlet rotor Aspect Ratio	2.25	2.50	[-]
Outlet rotor Aspect Ratio	1.25	4.00	[-]
Inlet stator Aspect Ratio	1.75	2.50	[-]
Outlet stator Aspect Ratio	1.50	4.00	[-]
Rotor blade material	RENE41	RENE41	
Stator blade material	RENE41	RENE41	
Rotor disk material	RENE41	RENE41	

5.1. Improvements in propulsive efficiency

Increasing the propulsive efficiency raises the amount of mechanical energy converted into thrust. Using a larger bypass flow is one of the methods to achieve higher propulsive efficiency. However, higher BPR will also lead to undesired effects like a larger fan diameter and higher fan blade tip speed. This section will elaborate on the methods that mainly focus on increasing the propulsive efficiency, the effect on all other gas-turbine characteristics will be discussed.

5.1.1. Effect of increased bypass ratio

The bypass ratio defines the amount of bypass flow compared to core flow. The bypass flow is only accelerated by a small increment. However, the fan moves a large amount of air, and thus still generates a significant amount of thrust. To get an understanding of the impacts of BPR on the turbofan engine characteristics, it is varied from 4 to 10. The results are shown in figure 5.1 - 5.6 where the BPR is plotted versus various engine performance parameters.

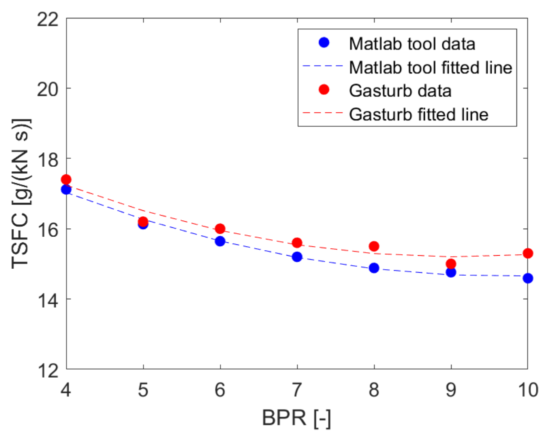

Figure 5.1: Thrust specific fuel consumption versus bypass ratio.

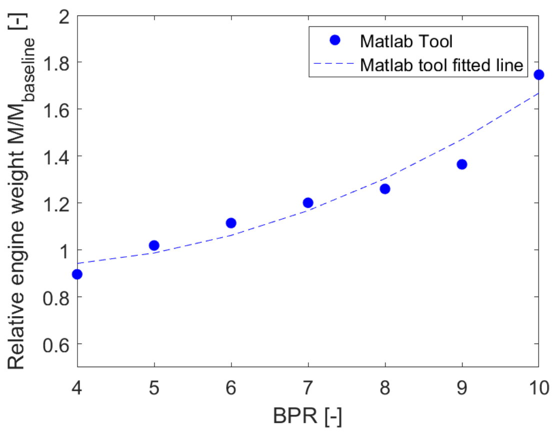

Figure 5.2: Engine weight versus bypass ratio.

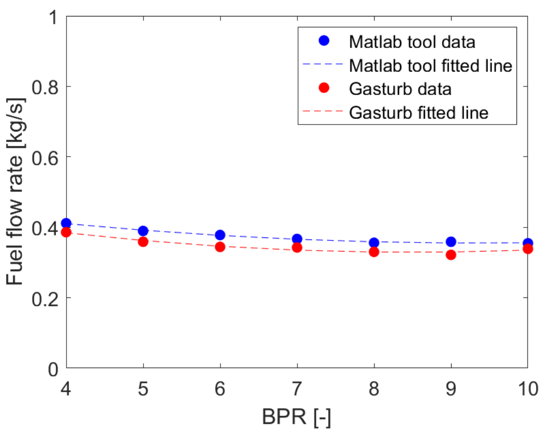

Figure 5.3: Fuel flow rate versus bypass ratio.

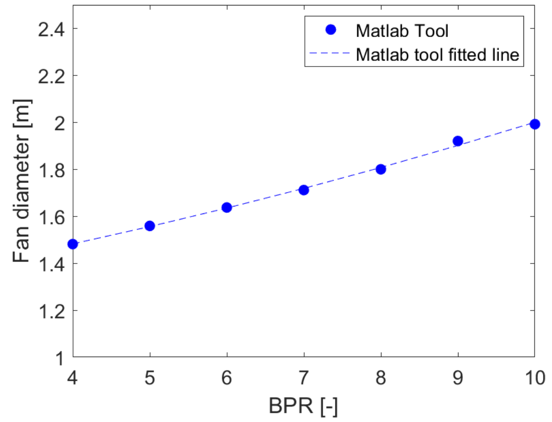

Figure 5.4: Fan diameter versus bypass ratio.

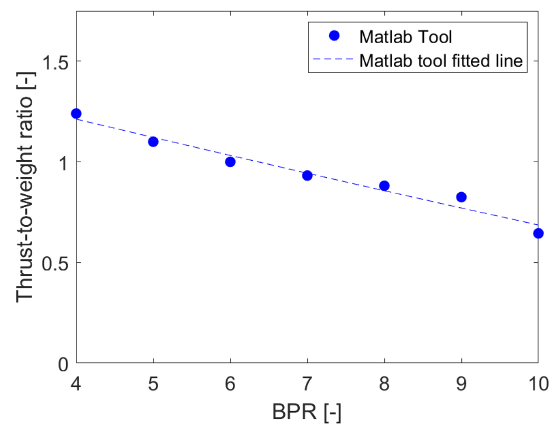

Figure 5.5: Thrust-to-weight ratio versus bypass ratio.

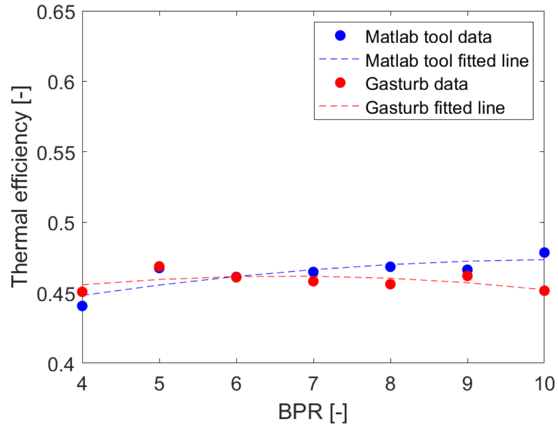

Figure 5.6: Thermal efficiency versus bypass ratio.

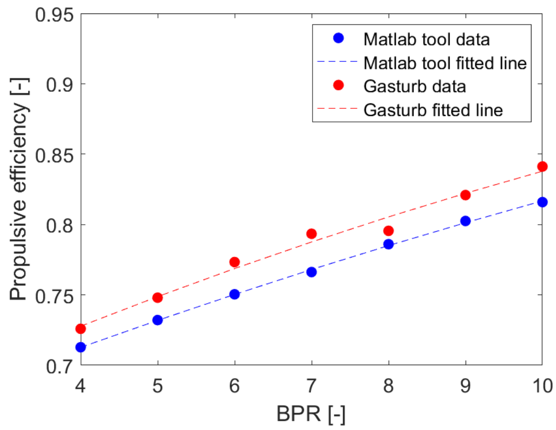

Figure 5.7: Propulsive efficiency versus bypass ratio.

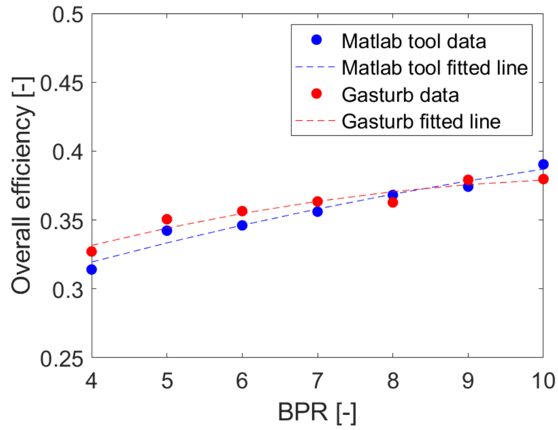

Figure 5.8: Overall efficiency versus bypass ratio.

Increased BPR affects the propulsive efficiency of the engine positively. The reason for the improvement in propulsive efficiency can be explained by the difference between the way the bypass nozzle and core nozzle produce thrust. The bypass flow accelerates a large amount of air with only a small increment while the core flow accelerates a small amount of air with a much larger increment. The difference in efficiency can be explained by the momentum equation and the energy equation, which are shown in equation 5.1 and 5.2 respectively. For the same momentum, less energy is needed if a large mass is accelerated with a small amount instead of accelerating a small mass with a large velocity increase. The reason for this is because the energy equation depends quadratically on the velocity term, while the momentum equation depends linearly on the velocity change. In figure 5.7, it can be observed that the propulsive efficiency improves for higher BPR as explained.

$$\text{Momentum} = m \cdot \delta v \tag{5.1}$$

$$\text{Energy} = 0.5 \cdot m \cdot v^2 \tag{5.2}$$

The most considerable benefit of a higher BPR is the decrease in TSFC, which means the engine is more fuel-efficient. This trend can be clearly observed in figure 5.1. In figure 5.6, the thermal efficiency is shown, which does not change with BPR because the BPR mainly affects to bypass flow. The overall efficiency (figure 5.8) shows a growing trend for higher BPR values because of the improved propulsive efficiency.

While the bypass nozzle produces thrust more efficiently, the specific thrust decreases for increased BPR. As a result, more intake mass flow is required to produce the same amount of thrust. This has a negative impact on fan size and engine weight, which can be seen in figure 5.4 and 5.2. The thrust-to-weight ratio (figure 5.5) is also negatively impacted due to the weight increase. The benefits of fuel efficiency will be at the cost of a heavier and larger engine.

In table 5.5 the weight distribution of the engine is shown, a clear trend can be observed where the total weight increases for higher BPR values. The fan weight shows an apparent increasing trend for increased BPR due to the larger fan size. The core flow becomes smaller for increased BPR. Therefore, the IPC, HPC, CC, and HPT show a decrease in weight. The larger fan will require more work delivered by the LPT. The LPT mass increases for increased BPR for this reason. In general, the higher fan and LPT weight surpasses the benefits of a smaller core size.

Another problem of an increased BPR is the higher tip speed of the fan blades due to the increased fan diameter. For the same rotational spool speed, a larger fan diameter will mean a higher tip speed. The higher tip speed will not only lead to higher engine noise but also larger centrifugal forces. At some point, the rotational speed must be lowered. A lower rotational speed on the low-pressure spool will impact the LPC and LPT performance in a two-spool configuration. A gearbox can be introduced to allow the LPT to still operate at a higher rotational speed. The gearbox will add extra weight, but a decrease in LPT stages may lower the LPT weight and counteract the weight increase due to the gearbox.

Table 5.5: Component mass breakdown for increased BPR.

Bypass ratio [-]	4	5	6	7	8	9	10
Fan [kg]	810	823	1025	1206	1308	1498	2264
IPC [kg]	110	110	104	108	126	131	80
HPC [kg]	158	134	129	123	127	126	123
CC [kg]	81	84	87	73	83	82	75
HPT [kg]	98	106	102	90	102	101	84
LPT [kg]	121	200	162	288	212	295	366
Ducts [kg]	14	16	15	14	14	14	20
Shaft [kg]	21	20	18	17	19	19	18
Frames [kg]	491	496	510	538	544	564	595
Controls [kg]	202	213	235	274	284	324	433
Total [kg]	2105	2203	2387	2730	2819	3154	4057

5.1.2. Effect of increased fan pressure ratio

The fan is what distinguishes the turbofan engine from the jet engine. The fan allows the engine to displace large amounts of air to produce thrust. The fan only accelerates the air by a small increment, which is more efficient and less energy costly compared to the jet engine. In this section, the effect of the fan pressure ratio is discussed. The fan pressure ratio indicates an increase in total pressure of the working fluid. It implies the amount of work done on the working fluid by the fan. In figures 5.9 - 5.16 the trends show the effect of the increased fan pressure ratio. The fan pressure ratio has been varied from 1.40 to 1.70 in steps of 0.05. The overall pressure ratio has been kept constant for all cases.

The thrust produced by the bypass nozzle increases as the pressure and exit velocity are both higher for increased FPR. The extra work required by the fan for the increased FPR will be extracted from the working fluid by the LPT. The core thrust will slightly decrease because more work is extracted from the working fluid, while the total enthalpy at turbine entry remains constant for all cases. The propulsive efficiency (figure 5.15) decreases for increased FPR because of the exit jet velocity of the bypass nozzle increases. The thermal efficiency (figure 5.14 increases because of the higher bypass nozzle exit jet velocity. The effect of the FPR on the overall efficiency is shown in figure 5.16, where it can be seen that a higher FPR has a positive effect on the overall efficiency. The specific thrust increases for increased FPR, therefore the fan diameter (figure 5.12) becomes smaller. The fuel flow (figure 5.11) also shows a decreasing trend because the intake mass flow is lower for higher FPR. The engine weight (figure 5.10) shows a very small decreasing trend, a smaller fan as a result of the lower intake mass flow is the reason for this decrease in weight. In figure 5.9, it can be seen that increasing the FPR is improving fuel efficiency. However, it can be seen from FPR 1.65 the trend shows a reverse in direction. At a certain point of increasing FPR, in this case at FPR 1.65, the BPR must be lowered else the fan design constraints (deHaller number) cannot be satisfied. The effect of BPR has been explained earlier. A lower BPR has a negative effect on efficiency and fuel consumption.

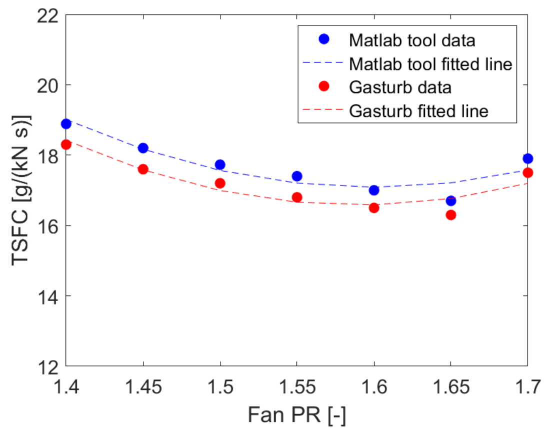

Figure 5.9: Thrust specific fuel consumption versus fan pressure ratio.

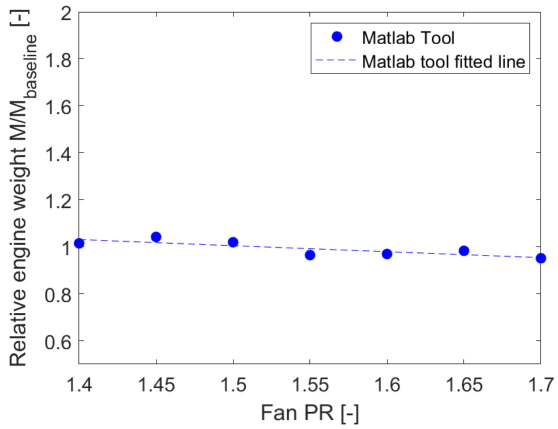

Figure 5.10: Engine weight versus fan pressure ratio.

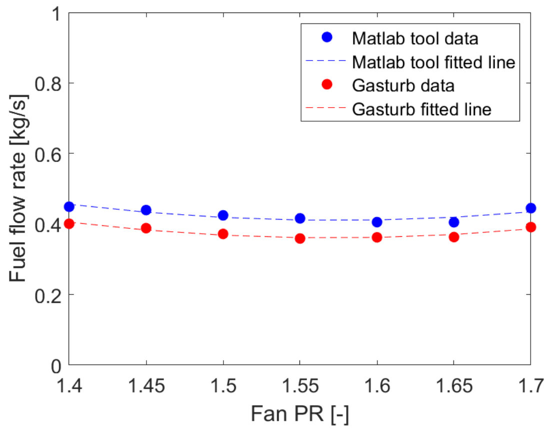

Figure 5.11: Fuel flow rate versus fan pressure ratio.

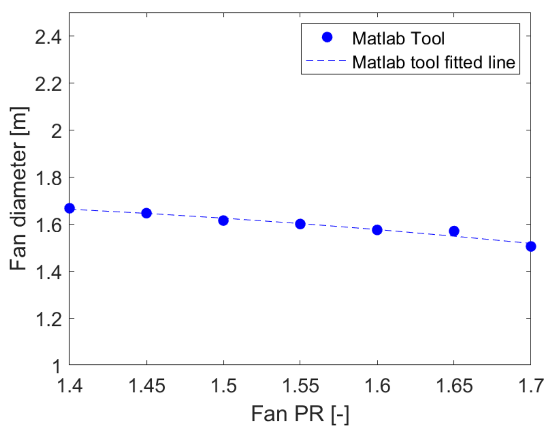

Figure 5.12: Fan diameter versus fan pressure ratio.

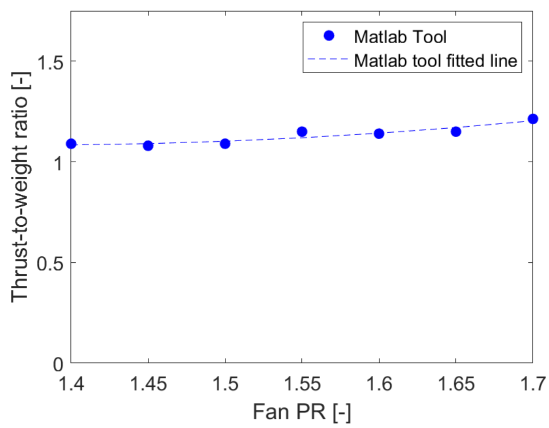

Figure 5.13: Thrust-to-weight ratio versus fan pressure ratio.

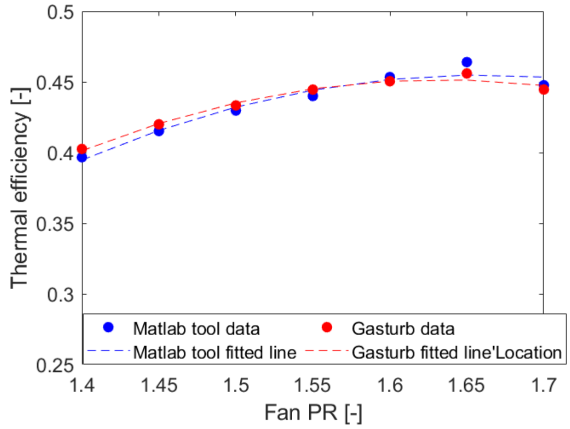

Figure 5.14: Thermal efficiency versus fan pressure ratio

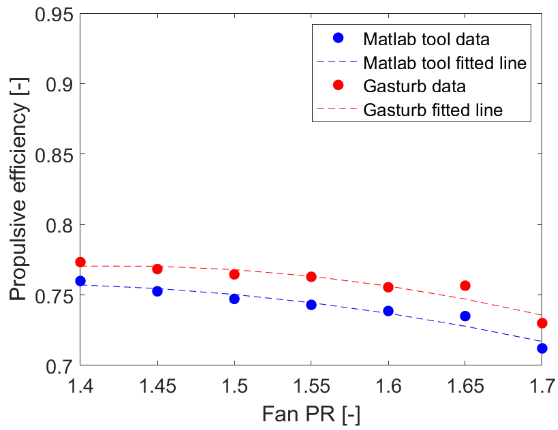

Figure 5.15: Propulsive efficiency versus fan pressure ratio.

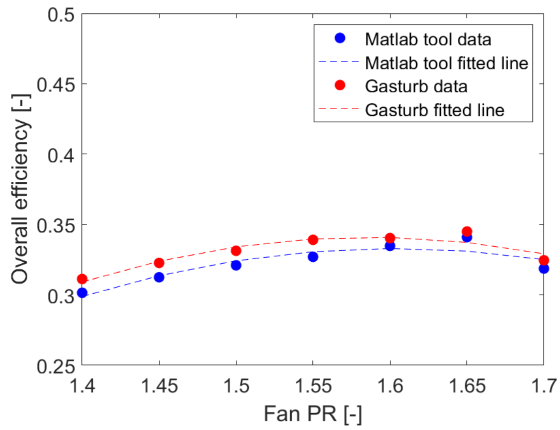

Figure 5.16: Overall efficiency versus fan pressure ratio

In table 5.6, the mass of the engine components for all the FPR values are given. The total weight shows a slightly decreasing trend, mainly because the intake mass flow reduces for higher FPR values. Most components follow the slow decreasing trend, except the LPT that must extract more energy from the working fluid for the higher FPR.

Table 5.6: Component mass breakdown for increased fan pressure ratio.

Fan pressure ratio [-]	1.40	1.45	1.50	1.55	1.60	1.65	1.70
Fan [kg]	879	923	916	829	813	871	851
IPC [kg]	158	150	136	128	140	110	107
HPC [kg]	141	130	129	130	130	132	138
CC [kg]	97	90	93	91	96	89	66
HPT [kg]	113	115	116	117	114	113	104
LPT [kg]	78	112	99	96	102	110	101
Ducts [kg]	20	17	16	17	17	16	19
Shaft [kg]	20	20	19	19	20	20	20
Frames [kg]	511	506	498	497	495	497	485
Controls [kg]	215	223	221	200	204	207	201
Total [kg]	2233	2286	2245	2123	2129	22156	2092

5.2. Improvements in thermal efficiency

The thermal efficiency defines the amount of energy from the fuel is converted into net mechanical work. In section 2.4.2, it was already shortly mentioned how the thermal efficiency could be improved under isentropic conditions. Improvements in thermal efficiency can be achieved by raising the OPR or TIT. This section will focus on the impact of these two design parameters on the engine characteristics.

5.2.1. Effect of increased overall pressure ratio

The overall pressure ratio has shown an increasing trend in the search for improved performance. In section 2.4.2, the H-S diagram is used to demonstrate that the divergent constant pressure lines are the reason the thermal efficiency improves for increased OPR.

The OPR is varied from 30 to 40, in steps of 2 in the analysis, the thrust produced by the engine has been kept at 24 kN. The pressure ratio of the fan and LPC are kept constant while the HPC pressure ratio is increased to reach the desired overall pressure ratio. The results have been shown in figures 5.17 - 5.24. The higher OPR values have an improved effect on the TSFC, as can be seen in figure 5.17. Using a higher OPR will mean not only the total pressure will be higher but also the total temperature. This means less fuel will be required to reach the TIT of 1300 K, as can be seen in figure 5.19. However, the increased OPR will require more compressor work is required, and thus also more work extraction by the turbine. The working flow will have a lower enthalpy when exiting the turbine as more work is extracted. The nozzle can produce less thrust as a result. To still generate the same amount of thrust, more intake mass flow will be required. The larger fan size for increased OPR can be seen in figure 5.20. The increased OPR will result in a heavier compressor. In combination with the slight increase in intake mass flow rate will, it results in an increase in engine weight. On the other hand, since the working fluid is more compressed, the annulus area downstream of the compressor is smaller. This negates some of the weight increase of the compressor. The trends on engine weight and thrust-to-weight ratio can be seen in figure 5.18 and 5.21 respectively. The thermal efficiency improves, as explained earlier, because the work available is higher for increased OPR. This is affirmed by figure 5.22. The propulsive efficiency also improves slightly, as seen in figure 5.23. The propulsive efficiency improves because the core exit jet velocity will be lower as a result of the higher work extraction by the turbine. The overall efficiency will be higher for increased OPR, mainly because of the thermal efficiency improvement and slightly because of the propulsive efficiency improvement for increased OPR.

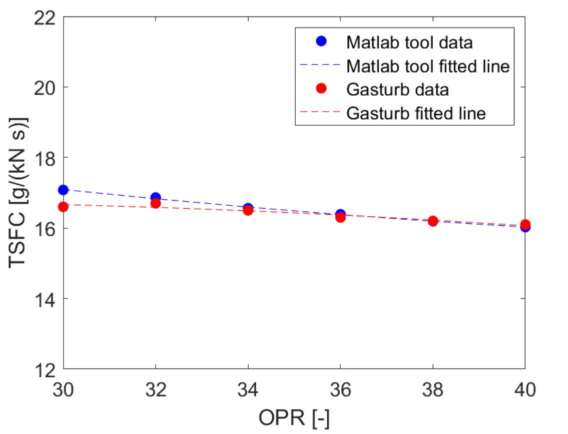

Figure 5.17: Thrust specific fuel consumption versus overall pressure ratio.

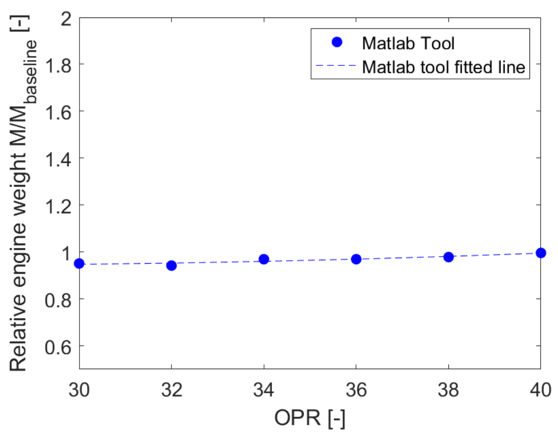

Figure 5.18: Engine weight versus overall pressure ratio.

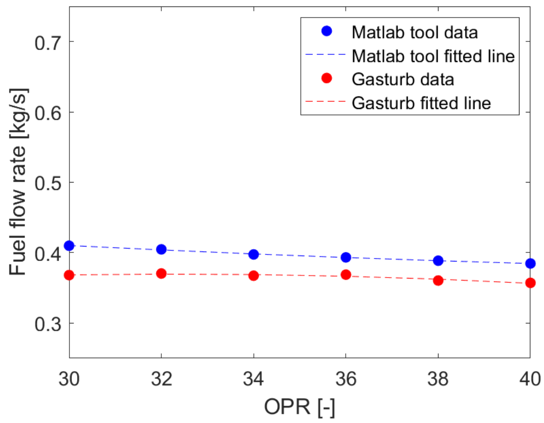

Figure 5.19: Fuel flow rate versus overall pressure ratio.

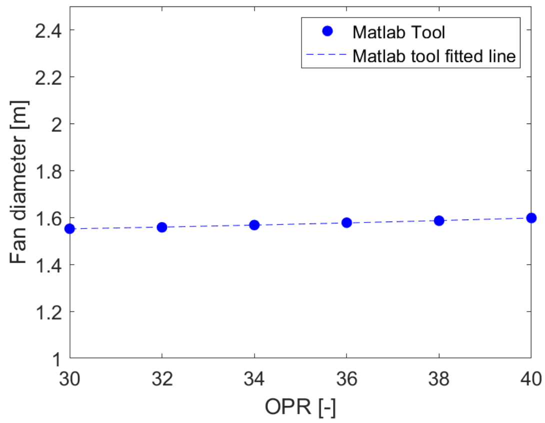

Figure 5.20: Fan diameter versus overall pressure ratio.

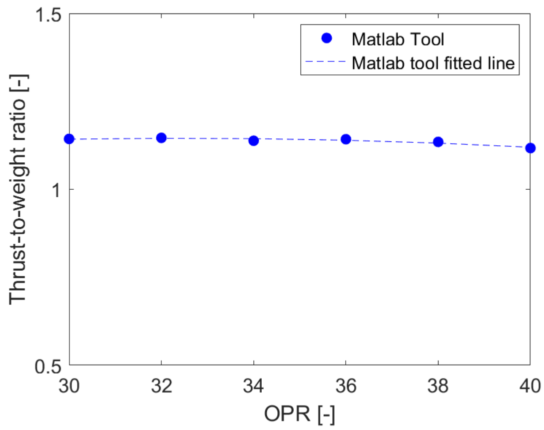

Figure 5.21: Thrust-to-weight ratio versus overall pressure ratio.

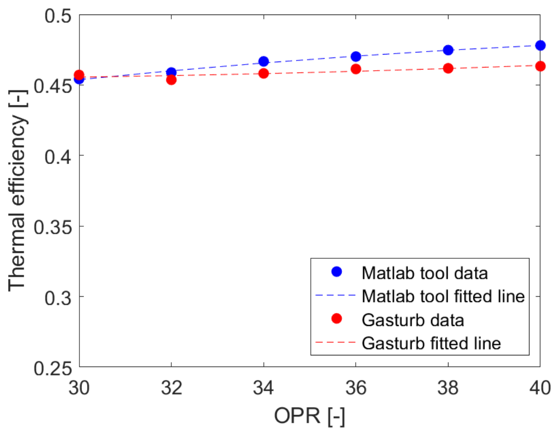

Figure 5.22: Thermal efficiency versus overall pressure ratio

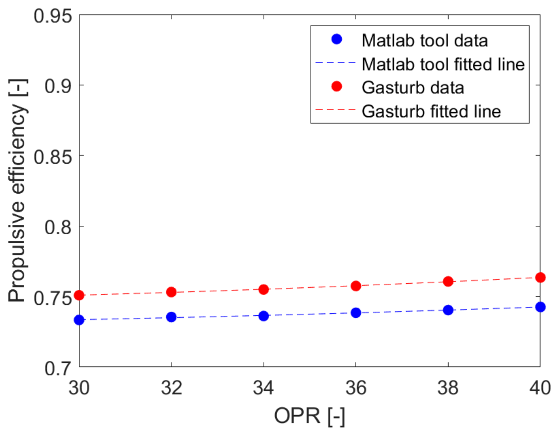

Figure 5.23: Propulsive efficiency versus overall pressure ratio.

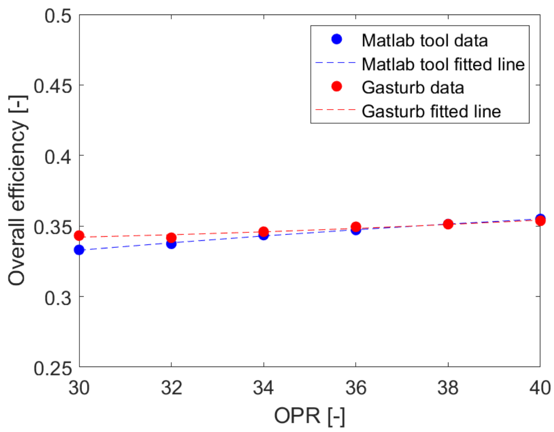

Figure 5.24: overall efficiency versus overall pressure ratio

In table 5.7, the weight breakdown results of the OPR parametric analysis are shown. The lower specific thrust means for increased OPR a higher intake mass flow will be required for the same thrust requirement. The fan, LPC, and HPC increase in weight for increased OPR because more work needs to be added to the working fluid. The components downstream of the compressors show a decrease in mass because the working flow is more compressed. As a result, the annulus area is smaller and therefore these components are lighter. The HPT shows a less clear decreasing trend compared to the LPT because the HPT needs to extract more work for HPC in the case of an increased OPR.

Table 5.7: Component mass breakdown for increased BPR.

Overall pressure ratio [-]	30	32	34	36	38	40
Fan [kg]	800	828	842	871	880	902
IPC [kg]	104	102	118	110	126	125
HPC [kg]	132	135	133	139	142	149
CC [kg]	56	53	52	50	50	51
HPT [kg]	119	108	120	110	103	99
LPT [kg]	145	121	128	109	105	110
Ducts [kg]	15	15	17	18	20	23
Shaft [kg]	16	18	18	18	18	18
Frames [kg]	500	496	500	438	499	501
Controls [kg]	198	197	204	204	206	211
Total [kg]	2087	2072	2130	2126	2150	2189

5.2.2. Effect of increased turbine inlet temperature

The turbine inlet temperature defines the gas temperature entering the turbine. Higher TIT will result in a higher gas enthalpy value, therefore more useful work can be extracted from the gas mixture. On the other hand, bringing the gas mixture to a higher temperature will require more fuel. In the parametric analysis, the TIT is varied from 1200 K to 1800 K with a step size of 100 K while the thrust produced is constant at 24 kN. The impact of the increased TIT is shown in figures 5.25 - 5.32.

Using an increased TIT will lead to higher thrust, but more heat will be wasted in the exhaust. The specific thrust increases for increased TIT, meaning more thrust will be generated per unit intake mass flow rate. The effect of this can be seen in figure 5.28, where a decrease in fan diameter can be observed for higher TIT. For the same level of thrust, less intake airflow will be required when TIT is increased. As a result, all engine components become smaller, and the engine weight decreases. This is confirmed by figure 5.26.

The higher TIT must be reached by increasing the fuel flow since more energy must be added to the working fluid, the increase in fuel flow can be seen in figure 5.27. The increased losses at higher TIT lead to a higher TSFC for increased TIT, which can be seen in figure 5.25. Both the propulsive and thermal efficiency show a decrease due to the increase in losses, as can be seen in figure 5.31 and 5.30 respectively. In this analysis, no cooling is taken into account. The maximum temperature for the rotor disk structural analysis has been limited at 850 K, because of material limitations. Having the rotor disks at this temperature could only be achieved with cooling. Especially for increased TIT, even more cooling flow will be required. This will reduce the amount of working fluid to be available for combustion and work extraction in the turbines. The losses due to cooling will also negatively impact the turbine stage efficiency.

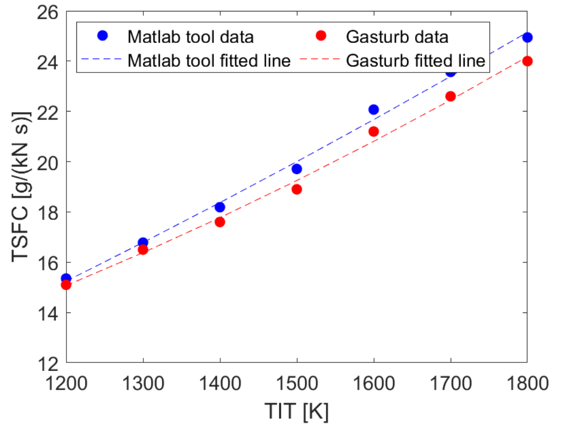

Figure 5.25: Thrust specific fuel consumption versus turbine inlet temperature.

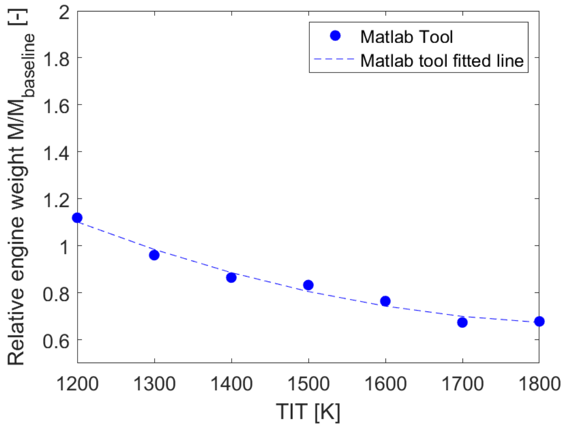

Figure 5.26: Engine weight versus turbine inlet temperature.

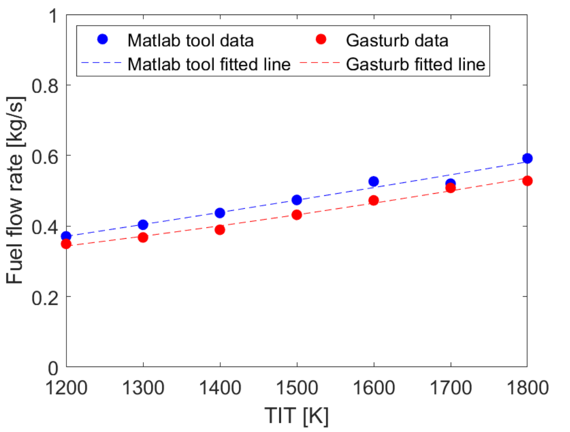

Figure 5.27: Fuel flow rate versus turbine inlet temperature.

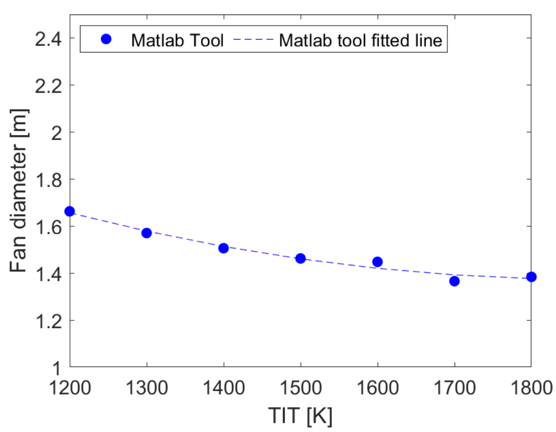

Figure 5.28: Fan diameter versus turbine inlet temperature.

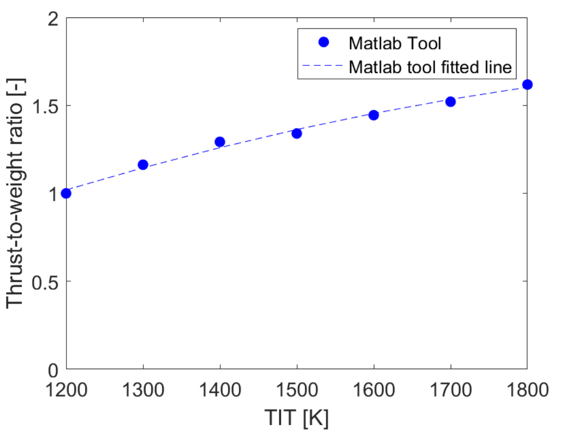

Figure 5.29: Thrust-to-weight ratio versus turbine inlet temperature.

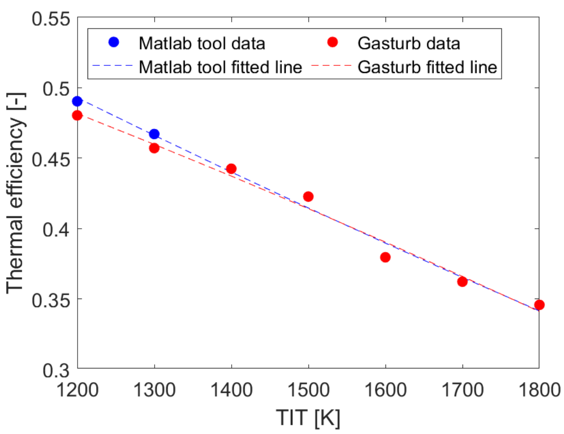

Figure 5.30: Thermal efficiency versus turbine inlet temperature.

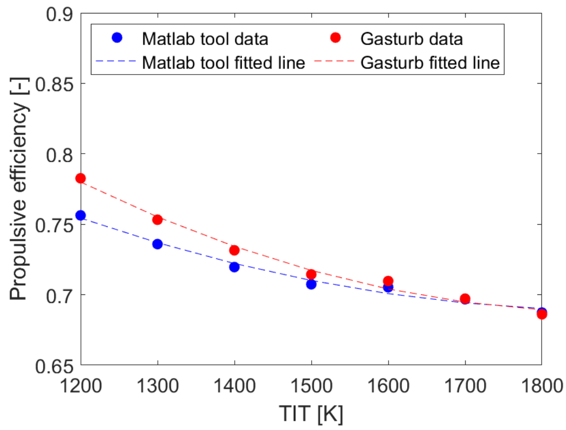

Figure 5.31: Propulsive efficiency turbine inlet temperature.

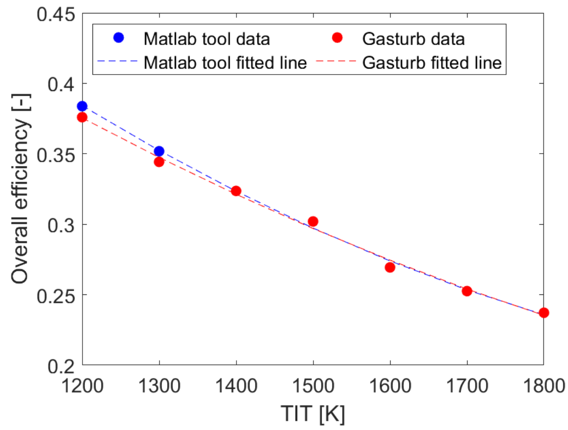

Figure 5.32: Overall efficiency versus turbine inlet temperature.

In table 5.8, the weight breakdown of the engine for various TIT values is shown. For increased TIT, all engine components decrease in weight because of the increased specific thrust. As a result, the intake mass flow is lower for the same thrust requirement. All components show a continuous decrease in mass except for the HPC. This is because an extra stage is needed from 1500 K because the radius is becoming smaller while the rotational speed remains the same.

The weight decrease for the components will be, in reality, less than shown in the table. No cooling is taken into account. As mentioned earlier, the maximum temperature for the rotor disk structural analysis is limited to 850 K. Either more cooling flow will be required to cool down the temperature to 850 K or materials with improved properties. Both possibilities will lead to an increase in engine weight.

Table 5.8: Component mass breakdown for increased TIT. [kg]

Bypass ratio [K]	1200	1300	1400	1500	1600	1700	1800
Fan [kg]	1023	848	711	739	611	668	516
IPC [kg]	150	122	130	77	85	76	70
HPC [kg]	119	133	134	141	141	130	121
CC [kg]	73	56	50	48	48	48	47
HPT [kg]	105	115	100	99	102	90	84
LPT [kg]	180	102	81	63	60	59	57
Ducts [kg]	20	17	15	12	12	11	10
Shaft [kg]	21	19	17	14	15	14	13
Frames [kg]	529	496	479	464	456	454	446
Controls [kg]	242	202	171	171	153	157	131
Total [kg]	2463	2109	1895	1829	1683	1708	1495

5.3. CFM LEAP 1A

New technology will drive the performance of aero-engines, the past has proven that every new engine has improved characteristics compared to its predecessor. The CFM LEAP 1A is the successor of the CFM56. This engine is also modeled using the conceptual turbofan engine tool to show the improvements of the LEAP with respect to the CFM56. Unfortunately, only very limited data is publicly available. Some input variables will be based on the CFM56 or literature. In table 5.9, the engine characteristics are shown for both the CFM56-7B and the LEAP 1A.

The effect of the design parameters analyzed in the previous section can be seen all together in the LEAP. This engine has an increased BPR, TIT, and OPR compared to the CFM56.

Table 5.9: CFM56-7B and CFM LEAP 1A characteristics at cruise conditions.

	CFM56-7B	CFM LEAP 1A	Unit
Intake mass flow rate	355	577	[kg/s]
Bypass ratio	5.1	11.1	[-]
Turbine inlet temperature	1300	1550	[K]
Overall pressure ratio	32.7	34.5	[-]
Cruise TSFC	16.06	15.00	[g/kN/s]
Cruise thrust	24	26	[kN]
Weight	2405	3072	[kg]
Fan diameter	1.549	1.98	[m]
HP spool rotational speed	14460	16645	[RPM]
LP speed spool rotational speed	4860	3856	[RPM]

The conceptual turbofan engine modeling results of the LEAP 1A are shown in table 5.10. The last four parameters are output results from the tool. The results are very close to the numbers from literature. The TSFC shows a 5.2% deviation, while the weight estimation only shows a 2.9% difference. Given all the assumptions and simplification made this result is very acceptable.

Table 5.10: CFM LEAP 1A data and CFM LEAP 1A modeling results for cruise conditions.

	CFM LEAP 1A	Matlab result	Unit
Mass flow rate	577	577	[kg/s]
Bypass ratio	11.1	11.1	[-]
Turbine inlet temperature	1550	1550	[K]
Overall pressure ratio	34.5	34.5	[-]
Fan diameter	1.98	2.02	[m]
Cruise TSFC	15.00	15.7832	[g/kN/s]
Cruise thrust	26.00	26.24	[kN]
Weight	3072	2982	[kg]

In figures 5.33, the Matlab 2D annulus shape estimated by the conceptual turbofan tool is shown. The tool can get very close to the number of stages of the original design. The tool has estimated four LPC stages, ten HPC stages, two HPT stages, and seven LPT stages. In the real case, the only difference with the estimate is the number of LPC stages, where it has three instead of four stages. The publicly available data of the LEAP 1A engine is limited. The exact pressure ratio of the compressors is unknown. This has an impact on the stage estimation since the work division of the compressors might be off compared to the original design. Also, due to the lack of a 2D cutaway of the LEAP 1A, the estimated annulus design can only be compared to the CFM56-7B. This is done in figure 5.34 to explain the differences between both designs.

The effect of the significant difference in BPR between the two engine designs can be seen in the fan size. Larger fan diameter is needed when the thrust produced is kept constant for increased BPR. The mass flow passing through bypass will be relatively larger compared to the core flow at higher BPR. The bypass nozzle has a lower specific thrust than the core nozzle. As a result, more intake mass flow will be needed to produce the same level of thrust for an increased BPR. In section 5.1.1, it has already been mentioned shortly, the larger fan diameter as a result of the increased BPR will lead to higher fan blade tip speed. In order to limit noise, pressure losses, and structural load, the rotational speed must be lowered to keep the tip speed within limits. Comparing the LP spool rotational speed of both the CFM56 to the LEAP, it can be observed that the LEAP has a 20% lower rotational speed while the fan diameter is around 20% higher. The fan blade tip speed, which is the rotational speed multiplied with the blade radius, will remain unchanged.

The increased OPR of the LEAP compared to the CFM56 has a negative effect on the number of compressor stages as both the LPC and the HPC show an increase in the number of stages. The increased OPR also means the gas is more compressed at the end of the HPC. The CC is smaller as the density of the gas is much lower, but the size of the CC and HPT seems partially unrealistic. Especially the HPT, where the blade chord is extremely small that it becomes challenging to find any disk shape able to withstand the stresses. The higher OPR means the turbine needs to extract more work from the working fluid. As a result, the LEAP has two stages compared to the single-stage HPT in the CFM. The LPT in the LEAP also has more stages compared to the CFM (7 vs. 4), the increased BPR and the much larger fan blades require much more work to be extracted from the working fluid.

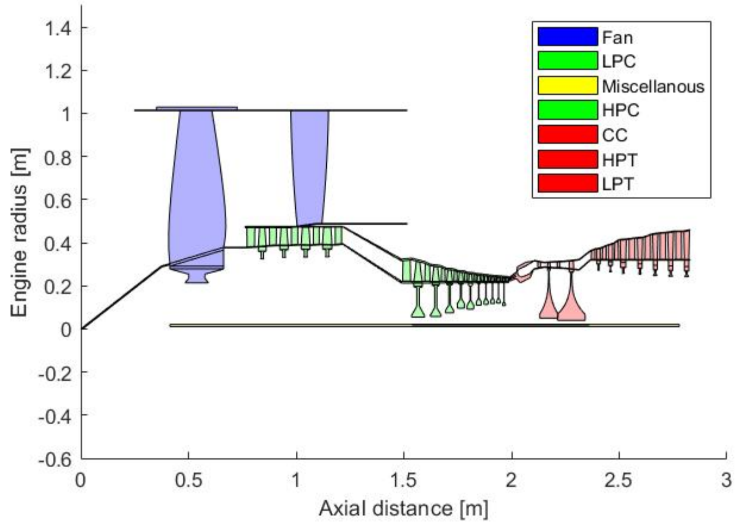

Figure 5.33: Estimated CFM LEAP 1A 2D annulus design.

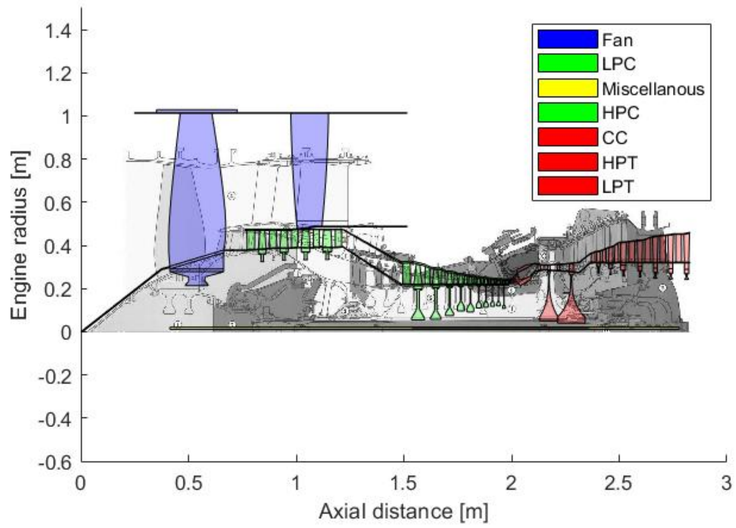

Figure 5.34: Estimated CFM LEAP 1A 2D annulus design overlaid on CFM56-7B 2D cutaway.

6

Conclusions and Recommendations

The increase of public awareness and political concern about the impact of aviation on the environment will make aero-engine design more challenging. Regulations are becoming stricter to further reduce emissions, reduce the noise emitted and improve the fuel efficiency of aero-engines. Accurate and quick analysis of engine performance and characteristics in the early engine design phase can help reduce the development time by eliminating unfeasible designs. Correcting initial estimates errors in the later design stages is more costly compared to earlier changes, therefore accuracy is of very important. This research project aims to develop a multidisciplinary turbofan engine design and sizing tool for conceptual engine design. The tool will be used in a parametric analysis to determine how the main design parameters impact engine characteristics. The results will give information on how the propulsive and thermal efficiency can be improved for the next generation aero-engines.

In this chapter, the main findings and conclusions will be presented followed by the recommendations for improvements and future work.

6.1. Conclusions

In this research project, a conceptual turbofan design and sizing tool has been developed. The main development work focused on the LPT, nozzle, and intake. Redesign of both the LPC and HPC and the design of a new HPT code were also required to develop a working engine tool. The tool is able to perform thermodynamic and structural calculations to find a design with the highest efficiency within the design constraints. The tool has been validated using two existing engines; the CFM56-7B and the PW4056. Both engines have been modeled with acceptable accuracy, the estimated weight is within 10% of the real engine weight. Given the fact the tool is designed for the conceptual design phase, meaning the use of mean line design and empirical models for the losses are the design philosophies to be used. Also, many smaller engine components have not been modeled because of their individual insignificance.

The tool has been used for the parametric analysis where the impact of several engine design variables has been analyzed. The results show how the propulsive efficiency, thermal efficiency and engine mass are affected. The design variables are increased till a range where the upper limit slightly exceeds the current level of technology to identify the future possibilities to further improve aero-engine design. The CFM56-7B has been used as the baseline for the parametric analysis. The cruise flight conditions (h = 10668 m, M = 0.82) were used and the cruise thrust requirement was set at 24 kN for all cases. The parameters analyzed are turbine inlet temperature (TIT), bypass ratio (BPR), overall pressure ratio (OPR), fan pressure ratio (FPR). The following conclusions are drawn based on the findings of the sensitivity analysis where the impact of several engine design variables was tested:

- The BPR is defined by the ratio of the bypass flow to the core flow. The bypass flow has a lower specific thrust compared to the core flow because the exit jet velocity is lower for the bypass nozzle. From the momentum and energy equation, it is clear why a lower jet velocity is more efficient because bigger mass with lower speed carries away less energy for the same momentum. When the BPR is increased from 4 to 10, the propulsive efficiency changes with 10.3% and the thermal efficiency with 3.8%, the overall efficiency improves from 31.4% to 39.0%. The TSFC is decreased by 14.8% as a result of the increased BPR. The drawback of the increased BPR is the increase in engine size and mass. The engine mass showed a strong increase of 95% in engine mass and 34% in fan diameter. The higher BPR is very beneficial in improving fuel efficiency because the bypass flow produces thrust more efficiently. However, the specific thrust of the bypass nozzle is lower compared to the core nozzle. More intake mass flow will be required, which results in an overall larger and heavier engine.

- A higher FPR means more work has been added by the fan to the working fluid. The FPR has been varied from 1.40 to 1.70, The effect of the FPR mainly affects the fan bypass flow, the bypass nozzle exit jet velocity increases for higher FPR. The trends on the impact of the FPR are difficult to show. At a certain point of increasing FPR, in this case 1.65, the flow diffusion exceeds deHaller number constraint. The BPR needs to be lowered to reduce the flow diffusion, which also impacts engine performance and engine mass. The increased FPR improves thermal efficiency but negatively impacts the propulsive efficiency. The reason for this change is the higher exit jet velocity of the bypass flow for increased FPR. The overall efficiency still shows an increase with increased FPR. As a result of the higher efficiency, the TSFC decreases. The specific thrust also increases for increased FPR because the bypass produces more thrust, therefore engine size and mass both decrease. However, in the case of too much flow diffusion, the BPR needs to be decreased. The effects of lowering the BPR will counteract the effects of the increased FPR.
- From the divergent behavior of the constant pressure lines in the T-S diagram, it is clear that a higher OPR is favorable for the fuel efficiency. The OPR has been varied from 30 to 40 in the parametric analysis. The TSFC has decreased by -6.2% while the engine mass increased by 4.8%. For the higher OPR, the compressor and turbine increase slightly in weight. The propulsive and thermal efficiency increase by 0.9% and 2.4% and the overall efficiency increased from 33.3% to 35.5%. The specific thrust decreased as a result of increased OPR, therefore the fan diameter has shown an increase of 2.9%. An increase of OPR improves fuel efficiency but the overall engine weight and size do increase to operate at higher OPR.
- The TIT has been varied from 1200 K to 1800 K and it has a major impact on the engine characteristics. The engine weight has shown a decrease of 39% because the specific thrust is higher for increased TIT. The intake mass flow can be reduced to still produce the same level of thrust, as a result, the engine fan diameter (-16.8%) and engine mass (-39.3%) decrease. The thermal efficiency and propulsive efficiency show a change of -6.9% and -15.8% in efficiency respectively. The overall efficiency drops from 37.1% to 22.8%. The higher heat losses cause the decrease is thermal efficiency while the higher exit jet velocity causes lower propulsive efficiency. More fuel will also be needed for combustion to bring the temperature to the increased TIT, in combination with the lower efficiency the fuel efficiency has drastically worsened. The TSFC has increased by 62.5% for the increased TIT.

It can be concluded that the propulsive efficiency can be improved by increasing the BPR. The larger fan produces thrust more efficiently because the exit jet speed is lower. Thermal efficiency can be improved by increasing the OPR and TIT, the divergent behavior of the constant pressure lines in the T-S diagram allows for more useful work output. Contrary to the improvements in efficiency is the increase in engine mass and size.

6.2. Recommendations

Based on the results and findings of this thesis project a list of recommendations can be given for further improvement of the current work or opportunities for future research.

- In the current tool cooling is not taken into account while in the real engines cooling flows do play an important role. Currently, the maximum material temperature for the structural analysis calculations is limited to 850 K. With cooling flows also modeled, realistic temperature can be used which will result in a more accurate structural analysis. The cooling flows will also impact the thermodynamic calculations.

- Design a new combustion chamber module because the quality and accuracy of the current module can be improved. In the new module, accurate emission estimations can also be included to further expand the capabilities of the conceptual turbofan design tool.
- The tool is now able to model and optimize a turbofan engine for a single operating condition. In reality engines need to operate in different conditions and therefore off-design conditions are also important. The engine should be optimized for the two most relevant operating conditions which are the *Hot Day Take Off at sea level* and *Max Climb at cruise altitude* while able to operate in all other operating conditions.
- In the current tool, the components are individually designed and optimized, while the components do affect each other. The designed engine is currently not the most efficient engine because the optimizer is not implemented at the engine level but instead on the component level. By changing the code structure and implementing a single optimizer instead of an optimizer for every component, the global optimum of the engine can be found.
- Unconventional turbofan design that incorporates an intercooler recuperator or an interburner combustor could also be analyzed. Especially, these unconventional engine designs are also interesting for the conceptual design phase.
- Add a gearbox to tool between the fan and LPT, currently, this is one of the limitations of current engine designs. By including a gearbox in the tool, it is possible to extend the possibilities to increase the BPR.
- A larger frontal fan area and nacelle size will lead to higher drag. In the future analysis, the drag generated by the fan and nacelle can be included in the tool to expand the capabilities of the tool.

Bibliography

[1] J. Tiemstra and A. G. Rao, *On the Conceptual Engine Design and Sizing Tool,* (2017).

[2] L. M. Nicolai and G. Carichner, *Fundamentals of aircraft and airship design, Volume 1*, Vol. 1 (2010) p. 883.

[3] J. Kurzke, *GasTurb Details GasTurb Details 5,* (2007).

[4] M. Boorsma and A. G. Rao, *Aero-Engine Gas Generator Conceptual Design,* (2015).

[5] P. Lolis, *Development of a Preliminary Weight Estimation Method for Advanced Turbofan Engines*, Ph.D. thesis (2014).

[6] H. W. Mattingly, J.D. and P. P.T., *Aircraft Engine Design*, 2nd ed., AIAA education series (American Institute of Aeronautics and Astronautics, 2002).

[7] S. Dixon, *Fluid mechanics and thermodynamics of turbomachinery* (1995) p. 537.

[8] G. Saravanamuttoo, H.I.H. Rogers and H. Cohen, *Gas turbine theory* (1996) pp. 321–334.

[9] D. G. Ainley and C. R. Mathieson, *A Method of Performance Estimation for Axial-Flow Turbines,* Aeronautical Research Council reports And Memoranda, N. 2974 **2974** (1951).

[10] D. Gutzwiller, *T-Axi Disk V2.2 User ' s Guide and Tutorial,* Ewp.Rpi.Edu , 1 (2009).

[11] M. T. Tong, I. Halliwell, and L. J. Ghosn, *A Computer Code for Gas Turbine Engine Weight and Disk Life Estimation,* Journal of Engineering for Gas Turbines and Power **126**, 265 (2004).

[12] ESDU, *Pressure recovery of axisymmetric intakes at subsonic Speeds. Item no. 80037* (Engineering Sciences Data Unit, 1980).

[13] G. Patterson, *Modern Diffuser Design,* Aircraft Engineering and Aerospace Technology **10**, 267 (1938).

[14] K. Kyprianidis, *"Multi-disciplinary conceptual design of future jet engine systems"*, Ph.D. thesis (2010).

[15] T. Bose, *Airbreathing Propulsion* (Springer Aerospace Technology, 2012).

[16] N. Birch, *2020 Vision: the Prospects for Large Civil Aircraft Propulsion,* Aeronautical Journal **104**, 347 (2000).

[17] A. Garcia and B. Bettignies-Thiébaux, *Beyond Vision 2020 (Towards 2050),* Aeronautics and Air Transport Beyond Vision **2020**, 1 (2010).

[18] L. Fishbach and R. Koenig, *GENENG — A Program For Calculating Design and Off-Design,* (1972).

[19] L. Fishbach and R. Koenig, *GENENG II — A Program for Calclating Design and Off-Design Performance of Two- and Three-Spool Turbofans With As Many As Three Nozzles,* (1972).

[20] W. L. MacMillan, *Development of a modular-type computer program for the calculation of gas turbine off-design performance,* Theses 1974 **PhD**, 228 (1974).

[21] J. Palmer and Y. Cheng-zhong, *TURBOTRANS: a Programming Language for the Performance Simulation of Arbitrary Gas Turbine Engines with Arbitrary Control Systems,* ASME 1982 International Gas Turbine Conference and Exhibit **5**, 8 (1982).

[22] W. V. Broomhead and M.J., *GSP A generic object-oriented gas turbine simulation environment*, Tech. Rep. (2000).

[23] W. Visser, *Gas turbine engine simulation at nlr,* (1995).

[24] U. Grönstedt, *Development of Methods for Analysis and Optimization of Complex Jet Engine Systems,* (2000).

[25] U. Grönstedt and P. Pilidis, *Control Optimization of the Transient Performance of the Selective Bleed Variable Cycle Engine During Mode Transition,* Journal of Engineering for Gas Turbines and Power **124**, 75 (2002).

[26] C. Drummond, G. Follen, and C. Putt, *Gas Turbine System Simulation: An Object-Oriented Approach,* (1992).

[27] R. Claus, A. Evans, J. Lylte, and L. Nichols, *Numerical Propulsion System Simulation,* Computing Systems in Engineering **2**, 357 (1991).

[28] J. Lytle, *The Numerical Propulsion System Simulation: An Overview,* CAS 2000 Workshop/The Ames Research Center (2000).

[29] A. Bala, V. Sethi, E. Gatto, V. Pachidis, and P. Pilidis, *PROOSIS – A Collaborative Venture for Gas Turbine Performance Simulation using an Object Oriented Programming Schema,* Power (2007).

[30] A. Alexiou, E. Baalbergen, O. Kogenhop, K. Mathioudakis, and P. Arendsen, *Advanced Capabilities for Gas Turbine Engine Performance Simulations,* Aerospace , p.14 (2007).

[31] L. Whitehead and J. Brown, *A mechanical design for a lightweight turbo-jet engine and the variation of engine weight with size,* National gas turbine establishment (1953).

[32] W. Pennington, *A mechanical design for a lightweight turbo-jet engine and the variation of engine weight with size,* Shell Aviation News (1959).

[33] E. Torenbeek, *Synthesis of Subsonic Airplane Design* (Delft University Press, 1976).

[34] D. Raymer, A. I. of Aeronautics, and Astronautics, *Aircraft design: a conceptual approach*, Educ Series (American Institute of Aeronautics and Astronautics, 1989).

[35] L. R. Jenkinson, J. F. Marchman, L. Jenkinson, and J. Marchman, *Aircraft Design Projects,* Aircraft Design Projects , 392 (2003).

[36] C. Svoboda, *Turbofan engine database as a preliminary design tool,* Aircraft Design **3**, 17 (2000).

[37] A. Guha, D. Boylan, and P. Gallagher, *Determination of optimum specific thrust for civil aero gas turbine engines: A multidisciplinary design synthesis and optimisation,* Proceedings of the Institution of Mechanical Engineers, Part G: Journal of Aerospace Engineering **227**, 502 (2013).

[38] D. Sagerser, S. Lieblein, R. Kkebs, N. Aeronautics, N. Aeronautics, and T. Memorandum, *Empirical expressions for estimating length and weight of axial-flow components of VTOL powerplants,* Technical Report **TM X-2406** (1971).

[39] R. Pera, E. Onat, G. W. Klees, and E. Tjonneland, *A Method to Estimate Weight and Dimensions of Aircraft Gas Turbine Engines,* Method of Analysis (1977).

[40] G. Klees and L. Fishbach, *1248. aircraft engine weight estimation method,* in *37th Annual Conference, Munich, West Germany, May 8-10*, Society of Allied Weight Engineers, Inc. (Society of Allied Weight Engineers, Inc., Munich, West Germany, 1978) p. 28.

[41] E. Onat and G. W. Klees, *A Method to Estimate Weight and Dimensions of Large and Small Gas Turbine Engines*, Tech. Rep. (1979).

[42] P. Hale, *A method to estimate weight and dimensions of small aircraft propulsion gas turbine engines.* Technical Report (1982).

[43] M. Tong and B. Naylor, *An Object-Oriented Computer Code for Aircraft Engine Weight Estimation,* Volume 1: Aircraft Engine; Ceramics; Coal, Biomass and Alternative Fuels; Manufacturing, Materials and Metallurgy; Microturbines and Small Turbomachinery , 1 (2008).

[44] J. Kurzke, *ADVANCED USER-FRIENDLY GAS TURBINE PERFORMANCE CALCULATIONS ON A PERSONAL COMPUTER,* , 8 (1995).

[45] V. Sanghi, S. K. Kumar, S. K. Sane, and V. Sundararajan, *Preliminary Estimation of Engine Gas-Flow-Path Size and Weight,* Journal of Propulsion and Power **14**, 208 (1998).

[46] S. Bretschneider, O. Arago, and S. Staudacher, *Architecture of a Techno and Environmental Risk Assessment Tool Using a Multi-Modular Build Approach.* ISABE 2007 Proceedings (2007).

[47] J. Kurzke and I. Halliwell, *Propulsion and Power: An Exploration of Gas Turbine Performance Modeling* (Springer International Publishing, 2018).

[48] M. P. Boyce, *Gas Turbine Engineering Handbook*, Vol. 23 (2011) p. 1000.

[49] D. G. Ainley and G. C. R. Mathieson, *An Examination of the Flow and Pressure Losses in Blade Rows of Axial-Flow Turbines,* **2891**, 1 (1951).

[50] M. Chase, *NIST-JANAF Thermochemical Tables, 4th Edition,* (1998), arXiv:arXiv:1011.1669v3 .

[51] S. F. Smith, *A simple correlation of turbine efficiency,* Journal of the Royal Aeronautical Society **69** (1965), 10.1017/s0001924000059108.

[52] S. Farokhi, *Aircraft Propulsion* (Wiley, 2014).

[53] J. M. Tournier and M. S. El-Genk, *Axial flow, multi-stage turbine and compressor models,* Energy Conversion and Management **51**, 16 (2010).

[54] S. Lieblein, *Loss and stall analysis of compressor cascades,* ASME Transactions, Journal of Basic Engineering. vol.81 (1959).

[55] C. C. Koch and L. H. Smith, *Loss Sources and Magnitudes in Axial-Flow Compressors,* Journal of Engineering for Power **98**, 411 (2010).

[56] R. Aungier and S. Farokhi, *Axial-Flow Compressors: A Strategy for Aerodynamic Design and Analysis,* Applied Mechanics Reviews **57**, B22 (2004).

[57] A. R. Howell, *Fluid Dynamics of Axial Compressors,* Proceedings of the Institution of Mechanical Engineers **153**, 441 (1945).

[58] M. I. Yaras and S. a. Sjolander, *Prediction of Tip-Leakage Losses in Axial Turbines,* Journal of Turbomachinery **114**, 204 (1992).

[59] R. B. I. Johnsen, *Aerodynamic Design Of Axial-Flow Compressors,* (1965).

[60] N. Falck, *Axial Flow Compressor Mean Line Design,* Lund University , 119 (2008).

[61] J. D. Denton, *Loss Mechanisms in Turbomachines,* Journal of Turbomachinery **115**, 621 (1993).

[62] P. Lampart, *Investigation of endwall flows and losses in axial turbines. Part I. Formation of endwall flows and losses,* Journal of Theoretical and Applied Mechanics **47**, 321 (2009).

[63] O. Sharma and T. Butler, *Predictions of Endwall Losses and Secondary Flows in Axial Flow Turbine Cascades,* Journal of Turbomachinery **109**, 229 (1987).

[64] S. Kacker and U. Okapuu, *A Mean Line Prediction Method for Axial Flow Turbine Efficiency,* Journal of Engineering for Power **104**, 111 (1982).

[65] M. W. Benner, S. A. Sjolander, and S. H. Moustapha, *An Empirical Prediction Method for Secondary Losses in Turbines—Part I: A New Loss Breakdown Scheme and Penetration Depth Correlation,* Journal of Turbomachinery **128**, 273 (2006).

[66] S. A. Zhu, Junqiang; Sjolander, *[asme asme turbo expo 2005: Power for land, sea, and air - reno, nevada, usa (june 6–9, 2005)] volume 6: Turbo expo 2005, parts a and b - improved profile loss and deviation correlations for axial-turbine blade rows,* (2005).

[67] J. Dunham and P. Came, *Improvements to the Ainley-Mathieson Method of Turbine Performance Prediction,* Journal of Engineering for Power **92**, 252 (1970).

[68] I. Inagaki, T. Takechi, S. Yoshihisa, and A. Nozomu, *Application and Features of Titanium for the Aerospace Industry,* Nippon Steel & Sumitomo Metal Technical Report , 22 (2014), arXiv:UDC 669.295:629.735.3 .

[69] S. C. Armand, *Structural Optimization Methodology for Rotating Disks of Aircraft Engines,* , 20 (1995).

[70] D. P. Gutzwiller and M. G. Turner, *Rapid low fidelity turbomachinery disk optimization,* Advances in Engineering Software **41**, 779 (2010).

[71] H. Loewenthal, *Design of Power- Transmitting Shafts,* (1984).

[72] E. Onat and F. F. Tolle, *An extension of engine weight estimation tech- niques to compute engine production cost. Technical Report N62269-78-C-0286*, Tech. Rep. (1979).

[73] G. Hanks and et al., *Nacelle Aerodynamic and Inertial Loads (Nail) Project Final Technical Report,* NASA contractor report **165807** (1982).

[74] A. Ibrahim, Y. Ryu, and M. Saidpour, *Stress Analysis of Thin Walled Pressure Vessels,* Modern Mechanical Engineering , 1 (2015).

[75] D. Wyatt, *Analysis of errors introduced by several methods of weighting nonuniform duct flows. NACA tech. Note 3400,* (1955).

[76] E. Fradenburgh and D. Wyatt, *Theoretical performance characteristics of sharp-lip inlets at subsonic speeds. NACA Rep. 1193,* (1954).

[77] J. Blackaby and E. Watson, *An experimental investigation at low speeds of the effects of lip shape on the drag and pressure recovery of a nose inlet in a body of revolution. NACA tech. Note 3170,* (1954).

[78] ESDU, *Friction losses for fully-developed flow in straight pipes. Item no. 66027* (Engineering Sciences Data Unit, 2008).

[79] ESDU, *Introduction to design and performance data for diffusers. Item no. 76027* (Engineering Sciences Data Unit, 2007).

[80] R. Scherrer and W. Anderson, *Preliminary investigation of a family of diffusers designed for near sonic inlet velocities. naca tech. note 3668,* (1956).

Appendices

A Pressure Recovery of Axisymmetric Intakes at Subsonic Speeds

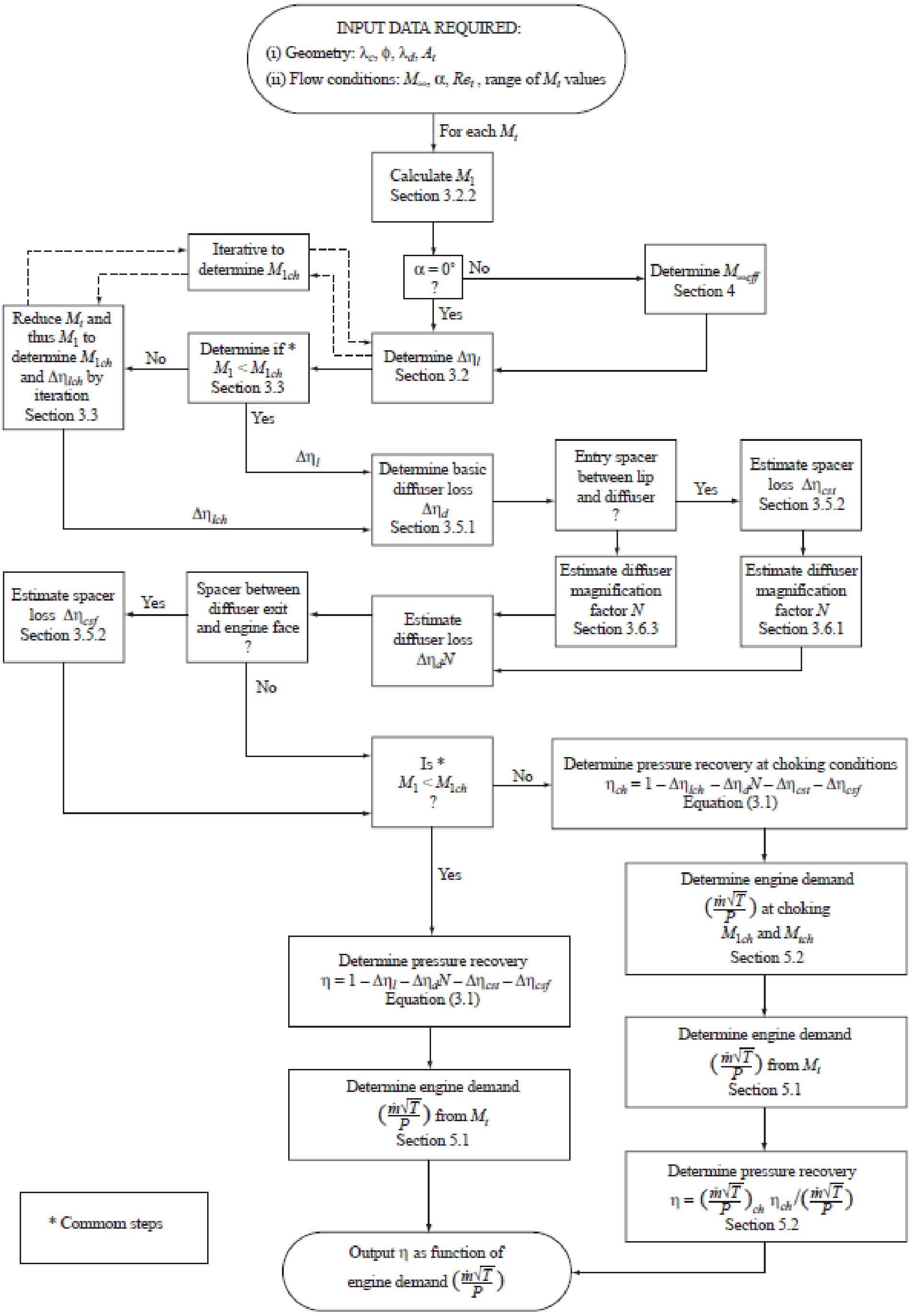

Figure A.1: Total Pressure Recovery Flowchart. Source:[12]

Intake Total Pressure Loss Estimation Method

The inlet cowl guides and decelerates the required airflow from free-stream conditions to the conditions required at the entrance of the engine fan. The engine fan works best a uniform flow of air at a Mach number of about 0.5. [6] The inlet total pressure recovery should be maximized to design an efficient engine. The total pressure recovery (η) of an engine is defined as the average total pressure at engine face P_2 divided by the total pressure available in the free-stream (P_∞). ESDU item no. 80037 [12] presents an estimation model for pressure recovery of axisymmetric intakes at subsonic speeds. The approach is limited to intake conditions below the choking of the flow.

Assumptions

In order to simplify the calculations, ESDU [12] has made several assumptions.

- Intake calculations assume uniform flow while real intake flow is often non-uniform. A method of averaging the measured flow parameters will be used to obtain an average total pressure. Wyatt [75] analyzed the error due to weighting methods for nonuniform duct flows. Two typical weighting methods are discussed; the mass-flow weighting and area weighting methods. The mass-flow-weighting method yields an average total pressure that is greater than the effective value. On the other hand, the area-weighting method provides yields total pressure values lower than the effective value. For the analysis the area weighing method will be used, this method provides a more conservative value of the pressure recovery.
- It is assumed that the external profile of the cowling has a negligible effect on the internal pressure performance. The stagnation point of the intake flow can occur on the external surface of the nacelle. These conditions in combination with sharp lips could lead to large separation losses.
- The losses in total pressure recovery due to skin friction will be based on the mean skin friction coefficient with the Reynolds number based on the throat conditions. It is assumed the skin friction coefficient remains unchanged through the intake whereas in practice this is not the case. The development of boundary layer and pressure gradient effects through the diffuser will change the local skin friction coefficient.

Pressure Loss Model Setup

ESDU [12] provides a breakdown of the loss sources, these loss sources are estimated in the model. The summation of all the losses will result in total pressure loss. The extensive flowchart of the empirical model is given in Figure A.1. The report by ESDU categorizes the intake losses in two main components:

- The loss associated with flow separations at the lip for combinations of intake mass flows and lip geometry
- The loss associated with the viscous effects of the diffuser due to boundary-layer growth and the effect of the pressure gradient imposed on it by the flow diffusion.

The model presented by ESDU is as follows:

$$\eta = 1 - \Delta\eta_l - \Delta\eta_d N - \Delta\eta_{cst} - \Delta\eta_{csf} \tag{A.1}$$

where:

$\Delta\eta_l$	is the loss in pressure recovery due to lip flow separation
$\Delta\eta_d$	is the diffuser loss excluding interaction between the entry flow and the diffuser
N	is a magnification factor for the effect of the entry flow on the diffuser loss on η_d
$\Delta\eta_{cst}$, $\Delta\eta_{csf}$	are allowances for the loss due to any lengths of constant section duct which may represent the intake upstream and downstream, respectively, of the diffuser

The intake geometry is graphically shown in figure A.2. Various positions on the intake are defined. In the pressure loss model, the intake will be split into three groups; the lip, the constant sections, and the diffuser.

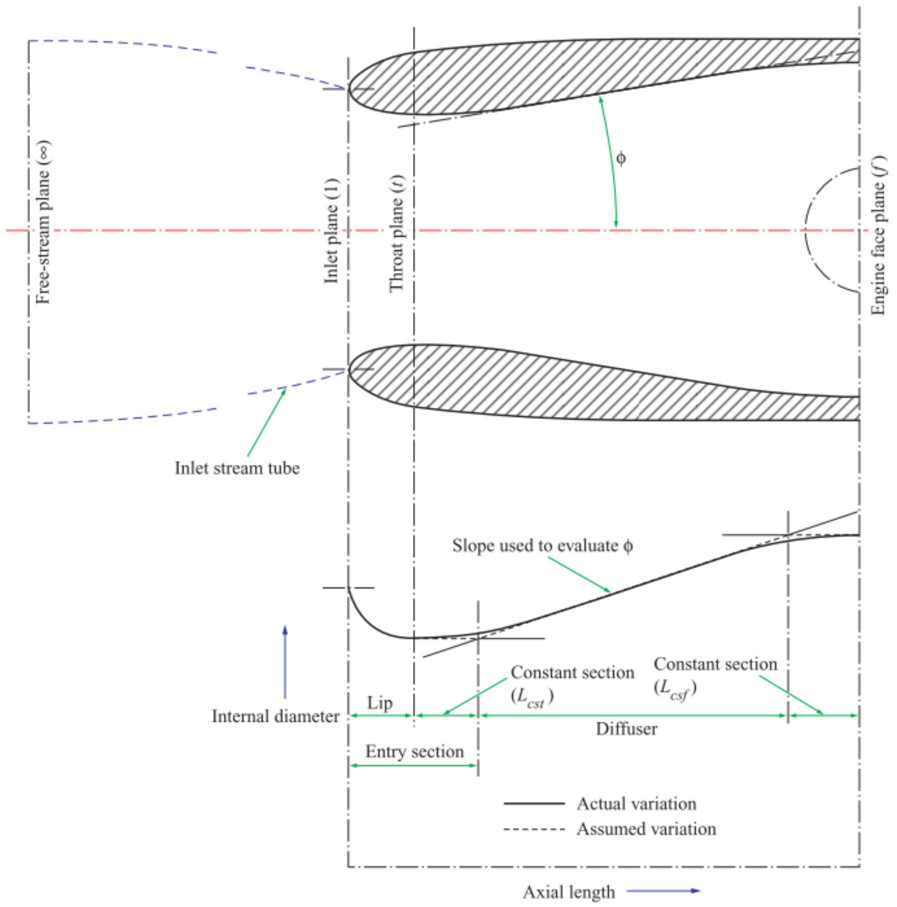

Figure A.2: Intake geometry nomenclature. Source:[12]

Loss in Pressure Recovery Due to the Lip

The pressure recovery method for intake lips will be split into two different approaches because the various lip geometries will lead to different flow paths. The lip geometries are split into sharp lips and rounded lips.

Loss for sharp lips

For velocity ratios less than unity, i.e. $A_1/A_\infty \geq 1.0$ the total pressure is equal to the free-stream value, no total pressure is lost ($\Delta\eta_l = 0$).

For velocity ratios greater than unity, i.e. $A_1/A_\infty \leq 1.0$ flow separation occurs on the inner surface of the lip. Fradenburgh and Wyatt [76] investigated these flow conditions for sharp lips and provided a method for the estimation of subsonic-flight-speed characteristics of sharp lip inlets. The analysis is based on momentum balance considerations between the free-stream and inlet planes. The pressure recovery is given in Fadenburgh and Wyatt as shown in equation A.2 and A.3.

$$\eta_l = \left[\frac{f(M_1)/f(M_\infty]^{(\gamma/\gamma-1)}}{1 + \gamma M_1^2 - \gamma M_\infty M_1 \left[\frac{f(M_1)}{f(m_\infty)} \right]^{1/2}} \right] \tag{A.2}$$

$$f(M) = \left(1 + \frac{\gamma - 1}{2} M^2 \right) \tag{A.3}$$

ESDU compared the values predicted by equation A.2 with measurement data and have found equation A.2 underestimates the loss in total pressure at high inlet Mach numbers M_1. A correction has been derived by ESDU and is shown in equation A.4, with equation A.5 being the correction factor.

$$\Delta\eta_{sl} = (1 - \eta_l)(\frac{2}{\beta_1} - 1) \tag{A.4}$$

$$\beta_1 = (1 - M_1^2)^{1/2} \tag{A.5}$$

The measurement data used by ESDU included some interaction effects between the entry flow and the diffuser. An allowance for this interaction has to be made to compensate for the interaction. The lip loss is given by equation A.6 with the interaction loss factor F. This is a empirical relation and is given in Figure A.3 as a function of $\Delta\eta_{sl}/M_t^2$.

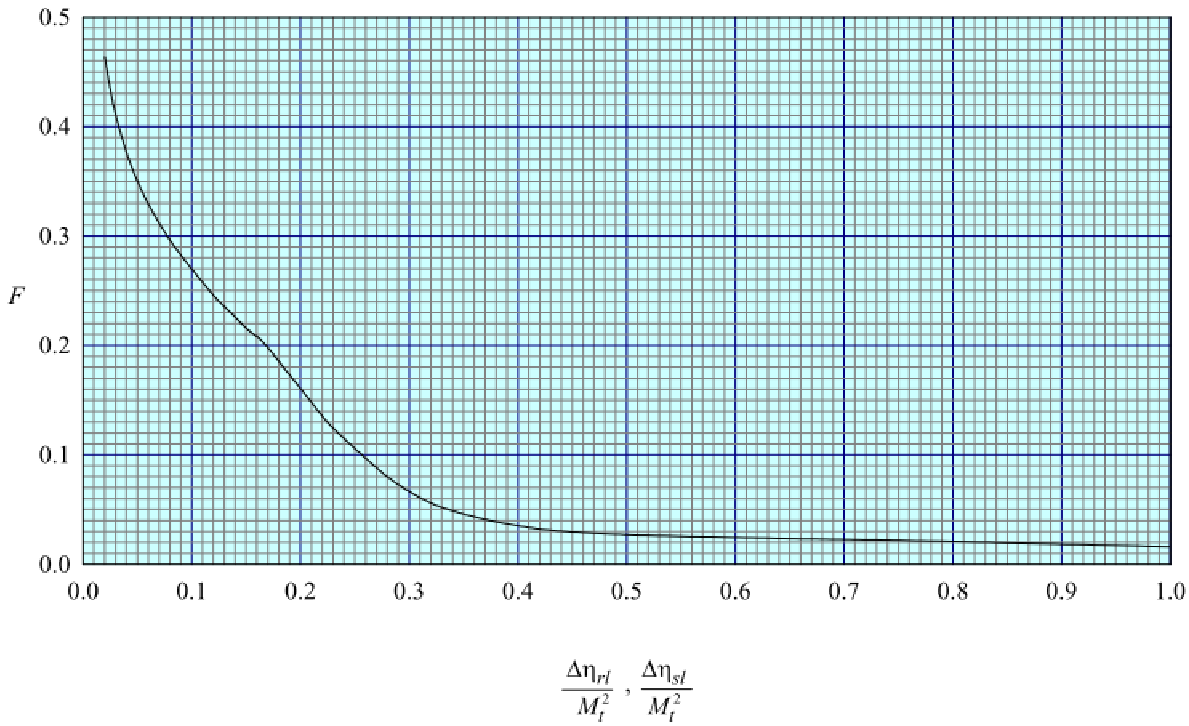

Figure A.3: Factor allowing for datum interaction effects between entry and diffuser. Source:[12]

$$\Delta\eta_l = \Delta\eta_{sl}(1 - F) \tag{A.6}$$

Loss for rounded lips

For rounded lips, two main characteristics differ with respect to sharp lips. Flow separation for some rounded lips is delayed to velocity ratios higher than unity or are completely suppressed if the entry contraction ratio is large enough. The geometry of rounded provides some "thrust recovery" in case of flow separation. At the separated location downstream of the lip a low-pressure condition will occur, the high-pressure flow at the intake lip will move towards to low-pressure region. Therefore the loss in pressure recovery is less than for a sharp lip at the same operating condition. [12]

ESDU used measurement data to find intake ratios A_1/A_∞ with zero lip loss. The results are presented in figure A.4. In the figure the λ_c value will find a corresponding $(A_1/A_\infty)_{crit}$ value, if the actual A_1/A_∞ is larger than $(A_1/A_\infty)_{crit}$ then the lip total pressure loss is zero.

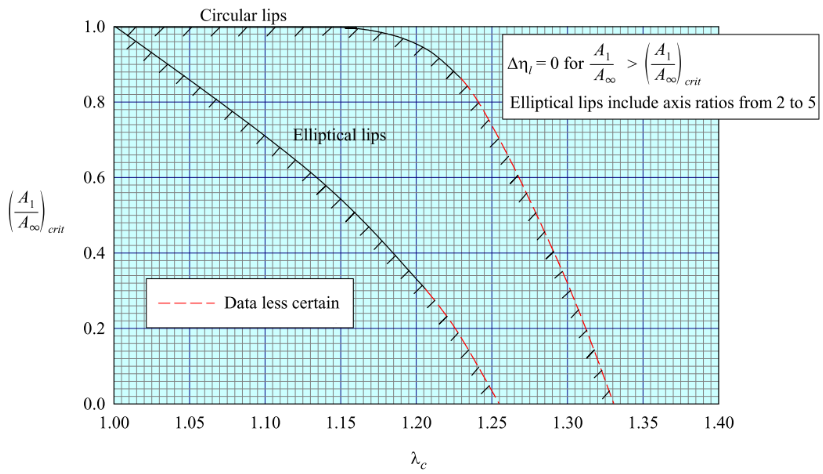

Figure A.4: Lip loss boundary at zero incidence. Source:[12]

If the A_1/A_∞ ratio is lower than the critical value then the lip total pressure loss must be evaluated. This will be done using the free stream Mach number and the inlet Mach number M_{1crit} associated with this critical value of $(A_1 A_\infty()$. Firstly the mass flow equation given in equation A.7 will be used to find the critical Mach number at location 1 $M_{1\text{crit}}$. This is done using the free stream conditions and $(A_1/A_\infty)_{\text{crit}}$ in combination with equations A.7 and A.8.

$$m_s = M\sqrt{\gamma}/\left(1+\frac{\gamma-1}{2}M^2\right)^{\frac{\gamma+1}{2(\gamma-1)}} \tag{A.7}$$

$$m_{s_{1crit}} = m_{s_\infty}/\left(\frac{A_1}{A_\infty}\right)_{crit} \tag{A.8}$$

For a given value of M_t the value of M_1 can also be found using the same approach used for $M_{1\text{crit}}$. Use equation A.7 and the mass-flow continuity equation A.9 to find S_1 and M_1.

$$m_{s_1} = \frac{m_{s_t}}{\lambda_c} \tag{A.9}$$

The lip losses for round lips can be summarized into equation A.10 and A.11.

$$\Delta\eta_{rl} = 0 \quad \text{for} \quad M_1 \le M_{1\text{crit}} \tag{A.10}$$

$$\Delta\eta_{rl} = K\Delta\eta_{\text{sl}} - \Delta\eta_{\text{slcrit}}) \quad \text{for} \quad M_1 \geq M_{1\text{crit}} \tag{A.11}$$

The factor K relates the loss for a rounded lip to that for a sharp lip and is given in Figure A.5. The parameters $\Delta\eta_{\text{sl}}$ and $\Delta\eta_{\text{slcrit}}$ can be found using equation A.4 and M_1 & $M_{1\text{crit}}$. As mentioned earlier ESDU used data that included some interaction effect interaction effects between the entry flow and the diffuser. A correction is required to take into account the interaction effects, this is done in equation A.12. The factor F is a correction factor for the interaction effect and can be determined using Figure A.3.

$$\Delta\eta_l = \Delta\eta_{rl}(1 - F) \tag{A.12}$$

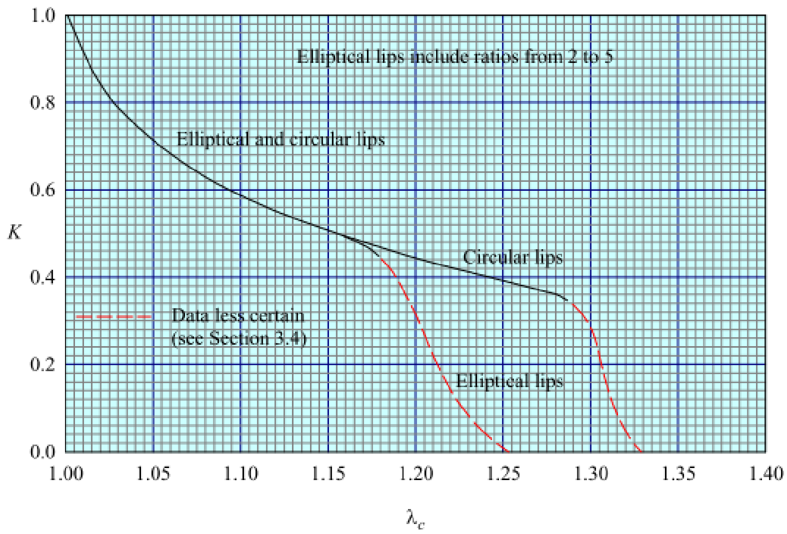

Figure A.5: Lip loss factor for rounded lips at zero incidence. source: [12]

Loss in pressure recovery due to the diffuser

The pressure recovery of the intake diffuser is primarily determined by the diffuser semi-angle ϕ, the diffuser area ratio λ_d and the Mach number at the throat of the intake M_t.

Diffuser Semi-Angle ϕ

Patterson [13] has published work on the efficient transfer of kinetic energy to pressure. In his paper he plotted the pressure recovery against the angle of divergence (2ϕ) for a conical diffuser based on data from others, figure A.6 shows the results. The results show that that the angle of maximum efficiency lies in the range 2ϕ = 5 deg. to 2ϕ = 8 deg. The efficiency drops significantly after 2ϕ = 10 deg.

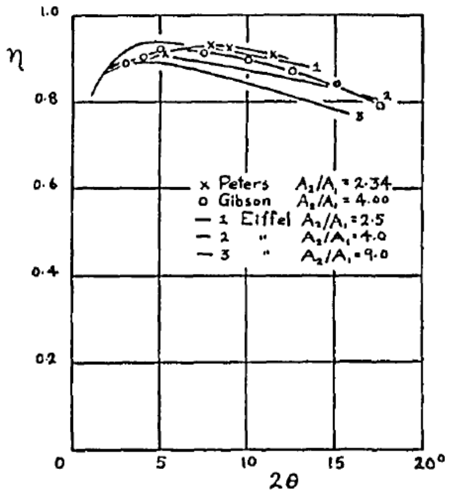

Figure A.6: Pressure recovery for conical diffusers. Source: [13]

Diffuser Total Pressure Recovery Estimation

ESDU [12] concluded the loss in total pressure in the diffuser can be assumed to be directly proportional to the entry Mach number squared. This conclusion is supported by data from Blackaby & Watson [77] who investigated the effect of lip shape on the drag and pressure recovery of nose inlets at low speed.

In the approach described by ESDU, the diffuser loss is estimated at a datum Reynolds number and subsequently corrected to the required throat Reynolds number. The diffuser loss at datum condition is given by equation A.13 where K_1 and K_2 are correction factors based on measurement data to relate the intake throat Mach number to the diffuser loss. The factors K_1 and K_2 can be determined with Figure A.7a and A.7b respectively.

$$\Delta\eta_{dd} = K_1 K_2 M_t^2 \tag{A.13}$$

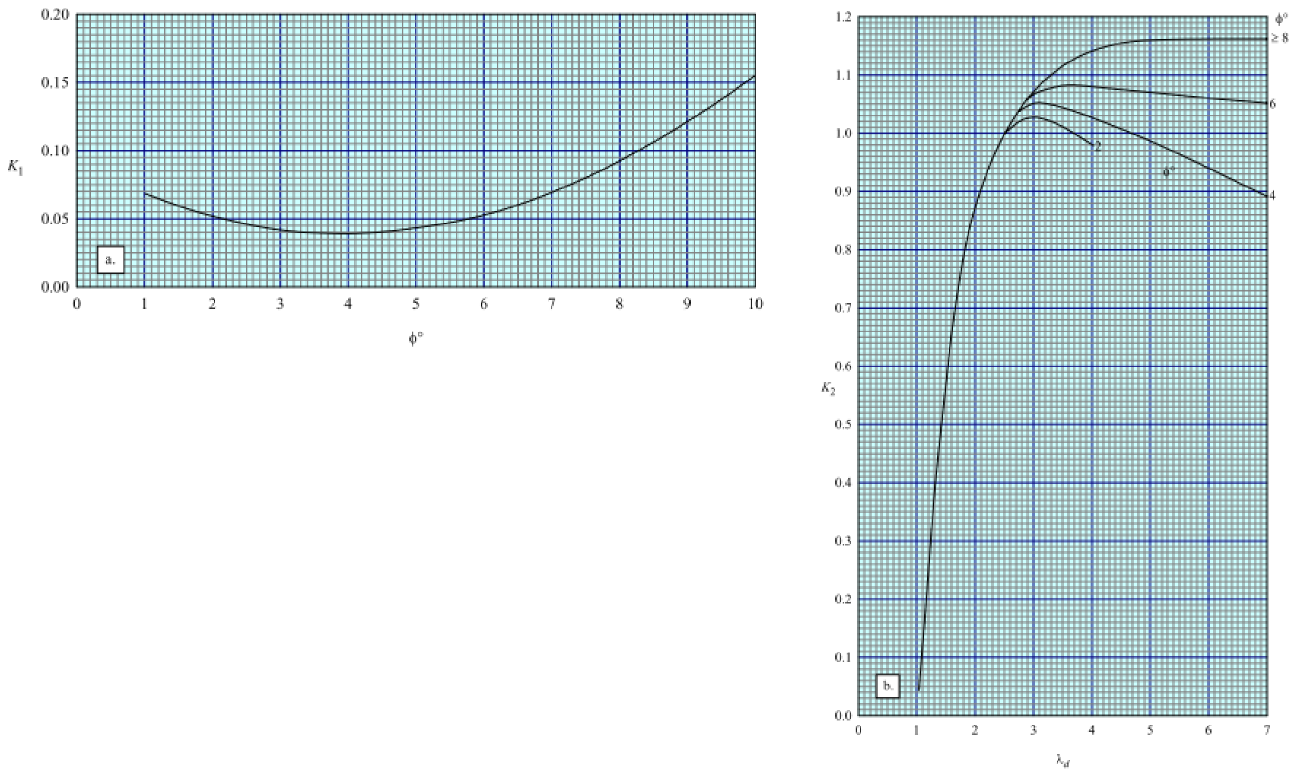

Figure A.7: Factors for diffuser losses. Source:[12]

The experimental data used to create the empirical relations were corrected to a constant Reynolds number of 7.5 × 10^5. The method used in correcting the measured data should also be used in scaling the data for Reynolds number changes. As result the values of $\Delta\eta_{dd}$ obtained from equation A.13 should be scaled as described by equation A.14. The parameter C_{f_d} is the skin friction coefficient and is given by equation A.15. Equation A.15 is based on ESDU item no. 66027 [78]. It describes friction factors for pipe flow assuming fully turbulent flow and is used to evaluate the mean skin friction coefficient for the diffuser (C_{F_d}) with Reynolds number based on throat conditions. In ESDU item no. 80037 [12] the mean skin friction coefficient (equation A.15) is used for all throat Mach numbers even though it is strictly only valid for incompressible flow.[12] The errors induced by this decision are small and therefore this assumption can be used in this project as well.

$$\Delta\eta_d = \Delta\eta_{dd}\frac{C_{F_d}}{C_{F_{dd}}} \tag{A.14}$$

$$C_F = \left[3.6log_{10}\left(\frac{Re_t}{7}\right)\right]^{-2} \tag{A.15}$$

Constant section lengths of duct

The losses of constant sections L_{cst} and L_{csf} are assumed to be given by the skin friction expression for pipe flows. The loss in energy due to the friction loss on the duct wall is equated to a loss in total pressure averaged over the duct area. [12] This is shown in equation A.16.The loss in pressure recovery due to the constant section is given by equation A.17.

$$\frac{\Delta P}{q_t} = 4\frac{L_{cs}}{D_{cs}}C_F\frac{D_t}{D_{cs}}^4 \tag{A.16}$$

$$\Delta\eta_{cs} = \left(\frac{\Delta P}{q_t}\right)\left[1-(1+0.2)M_t^2)^{\frac{-\gamma}{(\gamma-1)}}\right] \tag{A.17}$$

Interaction Loss between intake entry and diffuser

Interaction effects due to flow separation and pressure gradient effects on boundary layers are complicated. ESDU item no.76027 [79] indicates that the diffuser total pressure loss is significantly influenced by the condition of the flow at the intake. The conditions of the boundary layer also have a large impact, at the entry of the diffuser it may be attached or separated. This has been confirmed by Scherrer and Anderson [80], in their paper they concluded that the use of a constant section settling length between the lip and the diffuser entry can reduce interaction effect. The constant section length can assist the separated flow to re-attach. However, the constant section does lead to higher friction losses and an overall increase in pressure losses when the flow does not separate and remains attached trough the whole duct.[12]

The minimum settling length to allows flow reattachment will vary with intake geometry and the magnitude of the lip loss. Scherrer and Anderson [80] suggest that a settling length equal to $D_t/2$ should be acceptable for most flow conditions up to an incidence of angle ϕ of 15 degrees. Scherrer and Anderson also suggest adding an angle of (ϕ) of $1/2$ degree to compensate for the effect of boundary layer growth.

ESDU item no.80037[12] presents a method for estimating the interaction loss. The method is based on the assumption that the interaction loss can be represented by a magnification factor (N) applied to the diffuser loss from equation A.17. The interaction loss can then be described by equation A.18

$$\Delta\eta_{dn} = \Delta\eta_d N \tag{A.18}$$

The magnification factor N is based on the diffuser semi-angle (ϕ) and the loss in pressure recovery before entry to the diffuser. ESDU has two ways to calculate the magnification factor. One method is for the attached flow at the diffuser entry while the other method is for detached flow at the diffuser entry. ESD scales the interaction losses with the diffuser losses. The magnification factors used depends on whether the flow is attached or separated.

Magnification factor for attached flow at the diffuser entry For attached flow the magnification factor will be given by equation A.19. The magnification factors N_1 and N_2 are given in figure A.8a and A.8b respectively. In figure A.8a N_1 is given as function of $\frac{\Delta\eta_{de}}{M_t^2}$ which is given in equation A.20. Factor N_2 is a function of diffuser semi angle ϕ.

$$N = 1 + N_1 N_2 \tag{A.19}$$

$$\frac{\Delta\eta_{de}}{M_t^2} = \frac{\Delta\eta_l + \Delta\eta_{cst}}{M_t^2} \tag{A.20}$$

Magnification factor for separated flow at the diffuser entry The procedure for separated flow will use the same approach as the attached flow. The magnification will be given by equation A.21. The magnification factors N_3 and N_4 are given in figure A.9a and A.9b respectively.

$$N = 1 + N_3 N_4 \tag{A.21}$$

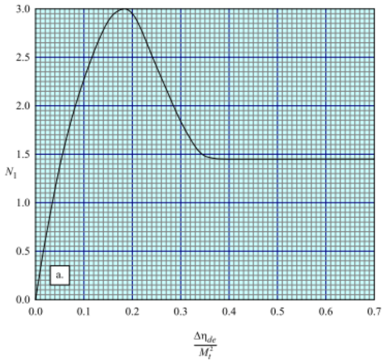

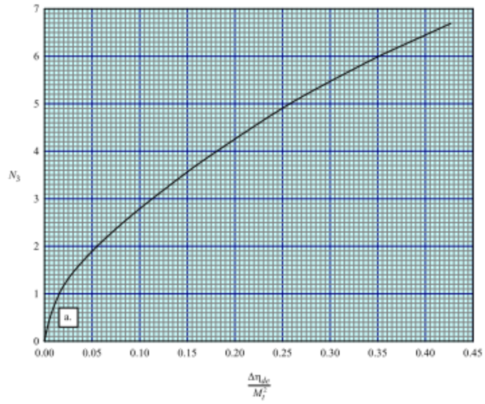

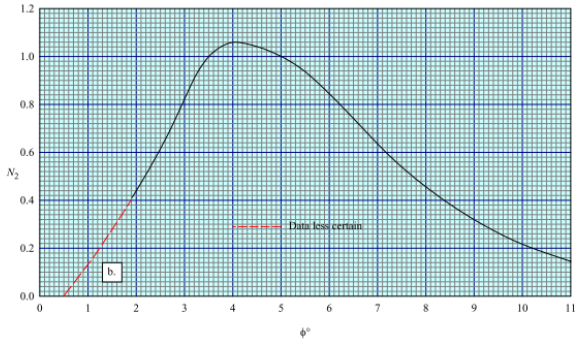

Figure A.8: Factors in equation A.19 for diffuser loss magnification factor. (Attached entry flow) source:[12]

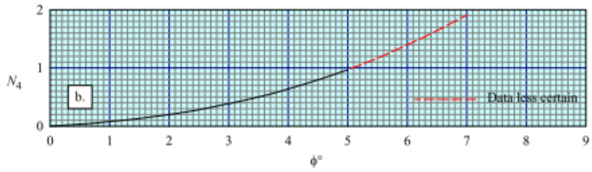

Figure A.9: Factors in equation A.21 for diffuser loss magnification factor. (Separated entry flow) source:[12]

Intakes at non-zero incidence and low speeds

The described approach is only valid for zero incidence angle intakes. To account for incidence effects ESDU[12] has provided an addition for the lip loss in the case of non-zero incidence. The effect of incidence angle on the lip loss is dependant on the flow conditions. Two cases for the effect of the incidence angle can be considered:

- If the flow has separated flow at zero incidence, the effect of incidence is to increase the magnitude of the lip separation and thus increase the loss in total pressure.
- If the lip has attached flow attached flow at zero incidence, the effect of incidence is to encourage the lip flow to separate.

It is clear that the incidence at which the flow separates is a function of the lip shape, entry contraction ratio (A_1/A_t) and the intake area ratio (A_1/A_∞). The method is for estimating the lip loss at non-zero incidence angle is exactly the same as described before in section A. The free stream Mach number M_∞ will now be replaced by an effective free stream Mach number $M_{\infty \mathrm{eff}}$. The effective free stream Mach number $M_{\infty \mathrm{eff}}$ will be described by equation A.22 and A.23 with α in degrees as the incidence angle.

$$M_{\infty \mathrm{eff}} = M_\infty \left[15\left(\alpha \frac{A_1}{A_\infty}\right)^{0.5} \right] \quad \text{for} \quad 15\left(\alpha \frac{A_1}{A_\infty}\right)^{0.5} < 90° \tag{A.22}$$

$$M_{\infty \mathrm{eff}} = 0 \quad \text{for} \quad 15\left(\alpha \frac{A_1}{A_\infty}\right)^{0.5} \leq 90° \tag{A.23}$$

$$\frac{A_1}{A_\infty} = \frac{S_\infty}{S_t}\lambda_c \tag{A.24}$$

According to ESDU [12] equations A.22 and A.23 are only valid for conditions where $A_1/A_\infty \leq 1.0$. For conditions where $A_1/A_\infty > 1.0$ a reasonable estimate is using $A_1/A_\infty = 1.0$.

Accuracy of total pressure recovery

The method of ESDU to estimate the total pressure recovery is mainly based on measurement data and used several assumptions and simplifications. It is not possible to give a single accuracy for the models, however, ESDU does provide an indication for the errors of each component of the total pressure recovery loss.

- Loss associated with the lip geometry at zero incidence, within ± 15 percent.
- Loss associated with the lip geometry at incidence, within ± 25 percent.
- Loss associated with the diffuser including the effect of entry flow, within ± 35 percent.

B Stage data storage

The stage calculation results will be stored in a matrix structure as discussed in Figure 3.12. In this appendix the second level nodes are elaborated upon. Each stage has an aero-station with the aerothermodynamic properties, geom-station for the geometrical properties and a vt-station for the velocity triangle properties. Each stage has three stations which will be the inlet of the first blade rows, the outlet of the first blade row or the inlet of the second blade row and lastly the outlet of the second blade row. The station numbering will be indicated in Figure B.1 - B.3 with i.

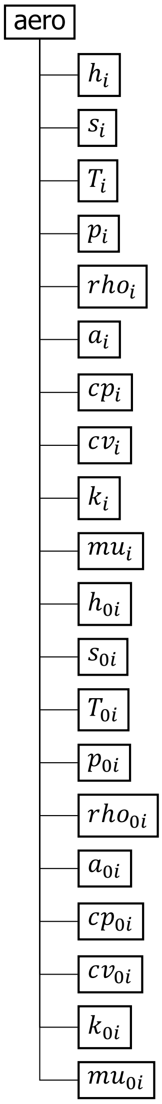

Figure B.1: Aero-station structure.

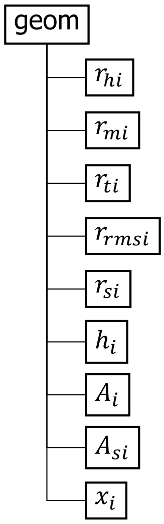

Figure B.2: Geom-station structure.

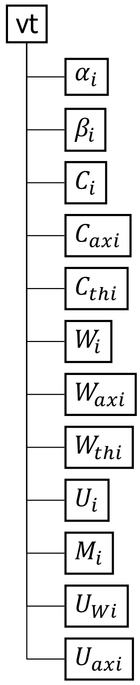

Figure B.3: Velocity triangle station structure.